MULTILAYER GRAPHENE AND CARBON NANORIBBON-BASED PHOTODETECTORS: FABRICATION AND PHOTORESPONSE MEASUREMENT

by

Rujie Sun

A thesis submitted to the faculty of
The University of Utah
in partial fulfillment of the requirements for the degree of

Doctor of Philosophy

Department of Materials Science and Engineering

The University of Utah

December 2013

Copyright © Rujie Sun 2013

All Rights Reserved

The University of Utah Graduate School

STATEMENT OF DISSERTATION APPROVAL

The dissertation of **Rujie Sun**

has been approved by the following supervisory committee members:

Name	Role	Date Approved
Feng Liu	, Chair	**10/28/2013**
Gerald Stringfellow	, Member	**10/28/2013**
Ling Zang	, Member	**11/01/2013**
Ashutosh Tiwari	, Member	**11/01/2013**
Florian Solzbacher	, Member	**10/31/2013**

and by **Feng Liu** , Chair/Dean of

the Department/College/School of **Materials Science and Engineering**

and by David B. Kieda, Dean of The Graduate School.

ABSTRACT

The focus of this dissertation is to study the multilayer graphene and carbon nanoribbon-based photodetectors through the fabrication of features like films, islands, mesas, as well as nanoribbons. The corresponding photoresponse was next explored with the realization of photodetecting devices. Graphene-based photodetectors have been fabricated and studied for a long time, and the mechanism of the photoinduced carriers in such photodetectors is still not clear. In addition, the photoresponsivity of graphene photodetectors is still improvable. Based on the research of the photoresponse experiment of multilayer graphene and carbon nanoribbon-based photodetectors, the mechanism for the photodetecting is further discussed and the photoresponsivity is highly improved by different methodologies. Specifically, this dissertation includes the following five chapters of topics: (1) introductions; (2) graphite / multilayer graphene photodetectors; (3) tunable photoresponse of epitaxial graphene on SiC; (4) photoresponse in carbon nanoribbon-based devices; and (5) conclusions. Overall, my dissertation achieves the goal of fundamental discussion of photodetecting in multilayer graphene and carbon nanoribbon-based devices and realizes the improved and tunable photoresponse in the meantime. I hope that this dissertation will help move forward graphene/carbon material-based research, which is not only limited to the device fabrication and nanopatterning technology but also to achieve a better output of photodetectors.

TABLE OF CONTENTS

ABSTRACT iii

LIST OF TABLES vi

Chapter

1. INTRODUCTION 1

1.1 Introduction to Graphene/Graphite 1
1.1.1 Graphene and the Forms of Graphene 1
1.1.2 Introduction to EG 3
1.1.3 Graphite: Graphene Stack 4
1.2 Graphene/Graphite Photodetectors 6
1.3 Photovoltaic Cell Based on CNRs 10

2. GRAPHITE/MULTILAYER GRAPHENE PHOTODETECTION 16

2.1 Raw Material Preparation 16
2.1.1 Graphite Selection 16
2.1.2 Graphite Etching Properties 17
2.1.3 Cleaving and Bonding of Graphite Film/Flakes 18
2.2 Fabrication of MLG Photodetectors 19
2.2.1 Etching Stop: Si 20
2.2.2 Photolithography-Defined HOPG Mesa 21
2.2.3 Fabrication of Graphite/MLG Photodetectors 22
2.3 Photoresponse of Graphite/MLG Photodetectors 28
2.3.1 Photodetectors with Symmetric Metal Scheme (Ti–Ti) 28
2.3.2 Photodetectors with Asymmetric Metal Scheme (Ti–Pd) 31

3. TUNABLE PHOTORESPONSE OF EPITAXIAL GRAPHENE ON SIC 51

3.1 Characterization of EG 52
3.2 Epitaxial Graphene-Based Photodetectors 53
3.2.1 EG Photodetector Fabrication and Measurement Preparation 54
3.2.2 EG Photodetector: Position Dependence 55
3.2.3 EG Photodetector: Power and Layer Thickness Dependence 56
3.2.4 EG Photodetector: Lead/EG Junction Dependence 57
3.2.5 EG Photodetector: Photoinduced Conductivity Change 58

3.2.6 EG Photodetector: Sunlight Detection 58
3.2.7 Carrier Mobility: SiC vs. EG 59

4. PHOTORESPONSE IN CNR-BASED DEVICES 69

4.1 CNR Fabrication by EBL 70
4.1.1 Approach for CNRs Fabrication 70
4.1.2 Parameters of EBL for CNR Cutting 72
4.1.3 Characterization of EBL-Defined CNRs 74
4.2 MLG/EG Nanoribbon Fabrication by FIB 77
4.2.1 Introduction to FIB 77
4.3 Photoresponse from CNR-Based Photodetectors 82
4.3.1 Introduction to GNR-Based Photodetectors 82
4.3.2 Photoresponse of EBL-Defined CNRs 83
4.3.3 Photoresponse Based on FIB-Induced CNRs 84

5. CONCLUSION 110

REFERENCES 113

LIST OF TABLES

Table Page

2.1 Parameters for O2 RIE of HOPG 36

2.2 Parameters used for SF_6 plasma etching 36

2.3 Parameters used for PR 1813 optical lithography 36

2.4 Parameters used for positive and negative lift-off process (SiO_2/Si substrate) 37

2.5 Parameters used for e-beam lift-off process 37

4.1 Parameters used for EBL based on PMMA processing 88

CHAPTER 1

INTRODUCTION

In this chapter we will provide the background information on graphene, graphene-based photodetectors, and Carbon Nanoribbon (CNR)-based photovoltaic devices and introduce the motivation of our research.

1.1 Introduction to Graphene/Graphite

In this section, the background of graphene and its different forms will be introduced, followed by a more detailed introduction to a specific form of graphene—epitaxial graphene (EG) as well as the graphene stack—graphite. Two of the applications of graphene, graphene-based photodetectors and photovoltaic cells, will be presented also.

1.1.1 Graphene and the Forms of Graphene

Graphene is a single layer of carbon atoms arranged in a honeycomb structure,[1, 2] which is the first two-dimensional (2D) atomic crystal available for use. Because of its unique and isotropic atom structure, it displays many remarkable properties, such as high electric and thermal conductivity[1–5] and high mechanical stiffness and strength,[6–8] which makes it suitable for many applications. Graphene is also considered a promising replacement for some of the currently used materials.

Different from most conventional three-dimensional (3D) materials, graphene is a truly 2D material that behaves as a semimetal.[7, 9–12] Near the 2D hexagonal Brillouin zone

boundary, i.e., six Dirac points of a single-layer graphene, carriers have a linear energy-wave factor (E-k) relation, which makes electrons behave as massless fermions or Dirac particles. The vanishing gap for the Dirac particles with zero mass ($E_0 = mc^2$) makes graphene a zero-gap semiconductor, i.e., a semimetal. This unique structure of graphene results in its extraordinary electronic properties.[7, 9, 12]

Electrically, the theoretical intrinsic electron mobility of graphene is calculated to be ~2×10^5 $cm^2 V^{-1} s^{-1}$ at room temperature,[13] while the recent experimental result is 2.5×10^5 $cm^2 V^{-1} s^{-1}$.[14] These values are two orders of magnitude higher than silicon transistors.[15]

Optically, graphene is able to absorb 2.3% of incident light from ultraviolet, visible to IR spectral range by just one single layer of carbon atoms. A high coefficient of light absorption is a consequence of the linear and gapless band dispersion of Dirac fermions.[16–18] The effective mass of carriers in graphene is zero (massless), which leads to a significant wavelength-independent absorption ($\pi\alpha$ = 2.3%) for normal incident light below about 1 eV.[17]

Graphene was first discovered as a form of cleaved layer from graphitic material.[1] It was then extensively studied and many other forms of graphene were then achieved with different methodologies. Besides the mechanically exfoliated graphene, CVD-grown graphene,[19] graphene reduced from graphene oxide,[20] and epitaxial graphene (EG) on SiC substrates[21, 22] were realized during the past few years.

Exfoliated graphene has been shown to have a large crystallite size and the highest carrier mobility. The mechanical exfoliation process is simple and effective to obtain graphene sheets in micron size. If we assume the mobility of electrons in exfoliated

graphene μ_e is equal to 2 x 10^5 cm^2 V^{-1} s^{-1}, and the electron concentration n in graphene is 4 x 10^9 cm^{-2}, we can get the conductivity of exfoliated graphene described as follows:

$$\delta_{graphene} = n*e*\mu_e, \tag{1.1}$$

where the electron charge e is ~1.6 x 10^{-19} Coulomb. Thus, the calculated electron conductivity of exfoliated graphene is ~0.13 mS, which is very close to the tested results in a suspended graphene device.[23] However, cleaving graphite to produce graphene may only fit the need for research, but it is not suitable for industry due to its extremely small yield and small sample size.

CVD graphene demonstrates large-area size and good continuity,[24] which is good for volume manufacturing in industry, but disorder and scattering processes lead to much lower carrier mobility than an exfoliated graphene sheet. In addition, CVD graphene needs to be transferred from Cu or Ni metal films to an insulating substrate for building electric devices. This transfer process may create additional chemical contaminations as well as structural defects. The reduction from graphene oxide shows a simple and inexpensive method to derive graphene chemically.[20] However, the solution-based process introduces contaminations and surface defects as well, resulting in the lowest mobility among all the forms of graphene.

1.1.2 Introduction to EG

Another form of graphene is EG, which has been heavily used in our experiments. EG is achieved by removing the Si atoms in SiC substrate, where it is processed at high temperatures (>1300 °C) and ultra-high vacuum (UHV).[21] Thus, the size and quality of EG is mainly limited by the original SiC substrate. Either Si-face or C-face SiC can be used for the growth of EG while the growth on C-face SiC is capable to generate more

layers of graphene with a faster growth rate, and the number of layers for graphene C-face SiC is well controlled.[25] 4-H and 6-H SiC substrates, which have bandgaps of 3.23 eV and 3.05 eV, respectively, are usually used for the evaporation of Si to form EG.

EG can be fabricated with a carrier density as high as ~3 x 10^{12} cm^{-2} and the electron mobility in the range of 10^3 cm^2 V^{-1} s^{-1}.[26] The EG-based field effect transistor (FET) can exhibit a transition frequency of 100 GHz under a certain bias,[26] higher than the frequency of a silicon-based FET (30 GHz for 200 nm channel length). EG films grown on 4-H SiC show a room-temperature conductivity of ~5 x 10^6 S/m,[27] which is comparable to the conductivity of exfoliated graphene.

Notably, EG on SiC can be fabricated as large-size, multilayered devices, suitable for volume manufacturing due to its good continuity, stability, and reproducibility.[21, 28, 29] The bottom SiC film can be conveniently used as a semi-insulating layer to support the EG device on the top.[30] In addition, the SiC substrate has much better thermal conductivity than SiO_2, which promotes the heat transfer from EG on SiC to the outside environment in some experiments, e.g., laser experiments on EG-based devices. Thus, the accumulative heat on EG will not greatly change the carrier temperature, affecting the electronic performance further.

Here in our research, EG samples were made on carbon face 4-H SiC with different layers of thickness, which were fabricated and provided by our collaborators at Institute of Physics (IOP), Chinese Academy of Science.

1.1.3 Graphite: Graphene Stack

Graphene is also a basic component for building many other graphitic materials, i.e., 0D buckyballs, 1D carbon nanotubes, or 3D graphite. Fig. 1.1 shows the schematic

drawing of the unzipping of a carbon nanotube (top-down process) or the wrap-up of a graphene film (bottom-up process).

Graphite is actually a stack of graphene films. The interlayer Van der Waals interaction in graphite plays as the cohesive force, and the space between two adjacent layers is ~0.34 nm. Graphite can be effectively treated as a multilayer system with almost decoupled 2D graphene sheets.[31] The resistivity of commercially available graphite (ZYA grade from *SPI Supplies Inc.*) is ~ 4 x 10^{-5} ohm-cm in the direction parallel to the layer plane, while the resistivity is as high as 0.15 ohm-cm in the direction normal to the layer plane. Thus, the electric properties of graphene are largely preserved in graphite, and graphene planes in a graphitic system of multilayer graphene (MLG) may perform independently, which make graphite a promising material for electronic applications.

The light absorption rate of a single-layer graphene is ~2.3%, while the multilayers in MLG will lead to a low light transmission. Especially in the visible region of spectrum, the relationship between light transmissivity *T(w)* and photoconductivity of graphene or graphite *σ(w)* can be expressed as follows,

$$\begin{aligned} T(\omega) &= \sqrt{\frac{\varepsilon_2}{\varepsilon_1}} \frac{4(\varepsilon_1\varepsilon_0)^2}{[(\sqrt{\varepsilon_1\varepsilon_2}+\varepsilon_1)\varepsilon_0+\sqrt{\varepsilon_1}\sigma(\omega)/c]^2}, \\ &\approx [1+\frac{\sigma(\omega)}{2\varepsilon_0 c}]^{-2} \end{aligned} \quad (1.2)$$

where the ε_0 is vacuum permittivity (8.85 x 10^{-12} F·m^{-1}) and c is the velocity of light (3 x 10^8 m/s). The photoconductivity of single-layer graphene σ_0 is equal to $e^2/4\hbar$. Considering the number of graphene layers $n(\omega)$ is related with the overall thickness ω of MLG by a factor of interlayer thickness, we can get the relationship as follows:

$$n(\omega) = \omega\ (nm) / 0.34\ (nm). \quad (1.3)$$

Also, we assume the photoconductivity of MLG or graphite is a multiple of σ_0 by the factor of $n(w)$. Then Equation (1.2) could be transformed into the following formula:

$$T(\omega)=[1+\frac{\sigma_0}{2\varepsilon_0 c}\frac{\omega}{0.34}]^{-2}. \quad (1.4)$$

The light transmissivity can then be plotted as a function of the thickness of MLG (see Fig. 1.2). From Fig. 1.2, over 90% of optical absorption can be achieved by up to 300 graphene layers in graphite. Therefore, graphite is able to work as a light absorber with very limited carbon materials. This unique property of notable optical absorption of MLG or graphite is utilized for our device application.

1.2 Graphene/Graphite Photodetectors

Graphene has attracted much recent attention because of its extraordinary electrical and optical properties that promise a wide range of device applications.[1, 10, 32–34] For example, graphene photodetectors have been fabricated for high-speed optical communication,[35, 36] wide band optical detection,[36–38] terahertz detection,[5, 39] and other applications.[28, 40, 41] Graphene-based photodetectors have been made using mechanically exfoliated graphene flakes,[1] CVD grown graphene,[19] and epitaxial graphene (EG) on SiC substrates.[21, 22]

Limited by the bandgap size, semiconductor photodetectors usually have limited detecting spectral width. However, there is no gap for graphene because of its conduction and valence band touching each other at the Dirac point.[11, 32] Thus, graphene-based photodetectors can be used for a wide spectral range, from ultraviolet to infrared. The high mobility of carriers in graphene supports the high-speed photodetecting, and the

high operating bandwidth promotes the high-speed data communications by graphene-based photodetectors.[35, 38]

The mechanism for the photocurrent generation in graphene-based optoelectronic devices is still not fully understood. There exist three main explanations: the built-in electric profile at the graphene-metal contacts, photothermoelectric (PTE) effects from hot carriers, and bolometric effects. Similar to the photovoltaic effect in semiconductor devices, researchers have found that the photogenerated current in graphene-based photodetectors usually occurs at the graphene-metal contacts, where an internal electric field accelerates the charge carriers to flow to contacts.[5, 35, 38] Metal electrodes (e.g., Ti, Cr, Al, and Pd, etc.) have been deposited on the two sides of graphene film/flake to form built-in electric fields at the metal/graphene interfaces. The electric profile is created by the work function difference between a metal electrode and graphene: the Fermi level of two materials line up at the thermal equilibrium and then the electric field shaped up as a slope (see Fig. 1.3). Electron carriers in graphene, in response to incident photons, are generated and directed from the interface to the metal leads. This internal electric field will drive electrons from one material of high work function to another with low work function.

Symmetric graphene photodetectors[38, 42, 43] are realized by using only one metal material to build the two electrodes on graphene. The mirror contacts (see Fig. 1.3a) lead to an opposite direction of electron flow. In contrast, an asymmetric metal scheme can be applied by using two metals,[35] one having a higher work function than graphene ($\phi \sim 4.6$ eV) and the other lower, to direct electron flow in the same direction to enhance the

signal under global illumination. The choice of metals, to achieve different slopes of band bending, will affect the optical-electric response in graphene photodetectors.

On the other hand, PTE effects are believed to be induced by the entropy difference at interfaces (like monolayer and bilayer graphene interfaces),[44] which is proportional to the difference of density of states (*D(E)*). Thus, hot carriers tend to diffuse to the material with higher *D(E)* to enable the maximized entropy, which leads to electron (or hole) doped materials (doped p-n). Such hot carrier transport may also apply for the photocurrent generation at graphene-metal interfaces: the temperature gradients (or say thermal voltage) drives electrons or holes from metal contacts to graphene to achieve the n-type or p-type doping.[45] However, the electric conductivity of graphene was reported to decrease under the increased local temperature.[46–49] The optical-enhanced phonon temperature will lead to strong electron-phonon scattering, hence reducing the conduction of electron carriers in graphene. Therefore, hot electrons (or hot phonons) will enhance (or reduce) the photoresponse of graphene.

Moreover, bolometric mechanisms can also explain the generation of electrons under optical illuminations.[50, 51] The resistance of the graphene can be changed by the enhanced local temperature, owing to the incident electromagnetic radiation. The small specific heat makes the electrons be quickly heated up, and the weak electron-phonon coupling allows the thermally decoupled electrons from the lattice.[52, 53] Based on light illumination, resistance change by photon absorption can be detected in electrical signals, and photocurrent is then generated in the biased graphene.

Although experimental results concluded that both photovoltaic and bolometric effects are relevant to the photocurrent generation,[51] the exact contribution from these

three effects for the generation of photocurrent at graphene-based photodetectors is still under debate. Our experimental results mainly support the band-bending theory at graphene-metal contacts, but we believe the PTE effects also contribute to the net photocurrent.

The photoresponsivity of several mA/W is observed in graphene photodetectors with or without source-drain bias. Plasmonic structures[54, 55] were reported to improve the optical response from graphene and hence to improve the device photoresponsivity. However, there are not many experiments confirming the enhanced photoresponse by the utilization of the different forms of graphene, i.e., graphite and its nanoribbons.

Graphene-based photodetectors are widely studied presently and reported in many publications, although graphite-based photonic devices were seldom researched historically. We believe the outstanding absorption rate of optical spectrum by multilayer graphene (MLG) will greatly improve the photodetecting performance, in contrast to graphene photodetectors. In addition, graphite/graphene nanoribbons (or carbon nanoribbons, CNRs) can also be applied in the photonic devices. Although fabrication of CNRs may introduce edge states that might affect the lifetime of carriers and hence weaken the photon induced signal response, recent experiments have shown that CNRs can in fact enhance light absorption due to the intrinsic plasmon enhancement in graphene that leads to improved photoresponse.[56]

Furthermore, graphene photodetectors were reported to generate electrons under optical illumination mostly within a 200–300 nm region next to the metal/graphene boundary (on one side of the boundary, there is pure graphene; on the other side, there is graphene covered by metal lead),[43, 57, 58] where a lateral electrical field zone exists across

the boundary without any gate bias. Also, a vertical field exists across the planar metal/graphene interface. Although the metal leads on top of graphene film may reflect a good portion of incident light, the photocurrent signal generated in the vertical electric field can still supplement the signal generated at the metal/graphene boundary region, especially if a large-area graphene metal contact is employed. For these reasons, we have built photodetectors both on a planar surface of EG with large-area metal leads and on CNRs.

1.3 Photovoltaic Cell Based on CNRs

Solar energy has been identified as the leading renewable energy source to meet the challenge of increasing demand for energy with limited fossil fuel resources on this planet. During the last decade, the photovoltaic (PV) industry is the fastest growing power-generation technology in the world, with the annual production capability increasing more than 60 times. A 2010 PV market analysis issued by the European Photonics Industry Consortium (EPIC) shows that production of PV modules will reach a record high again in 2011, primarily due to the growth in crystalline silicon (Si) cells and thin-film cadmium telluride (CdTe) cells. However, due to the rapid growth in the PV industry globally, the raw material cost has been increasing rapidly, especially for crystalline Si. On the other hand, Te is an extremely rare element (one part per billion in the Earth's crust),[59] making the use of CdTe in sufficiently large quantities a serious potential problem. This calls for the development of new, efficient PV cells using cheap and abundant raw material.

Fig. 1.4 shows the reserve amount of graphite in comparison with other in-use PV materials. According to the 2011 US Geological Survey report,[60] the world’s inferred

recoverable graphite resources exceed 800 million tons. The reserve base of graphite in the United States exceeds one million tons, while neighboring countries such as Mexico, Brazil, and Canada are all major graphite exporters. Therefore, graphite provides an abundant, sustainable, and cost-effective raw material resource for harvesting solar energy, provided an efficient PV technology can be developed. In addition, graphite has recently been selected to undergo outer space harsh environment tests for electronic and PV applications because of its extreme stability and durability.

Recently, Lagally and Liu proposed a novel design of efficient multigap solar cells based on the radical concept of employing a new class of graphite-based material, lithographically-defined carbon nanoribbons. A patent entitled "Graphite-Based Photovoltaic Cells" (US patent publication no. 2010/0132773), filed on this invention jointly by the University of Utah and the University of Wisconsin-Madison, has been allowed by the US patent office in December 2010. The conceptual basis of the proposed solar cell originates from our recognition that the energy gap of CNRs exhibits a dependence on their dimensions, similar to graphene nanoribbons as shown experimentally (see Fig. 1.1).[61, 62] With the proper selection of metal contacts of different work functions (ϕ),[63] a Schottky barrier PV cell can be constructed, whose energy diagram is shown in Fig. 1.5 using Ti (ϕ =4.3 eV) and Au (ϕ =5.1 eV) as electrodes.

Upon photoexcitation, electrons and holes will be generated within the CNRs and be separated by the building-in potential (V_{bi}), which equals the work function difference between the two metal leads, to generate electricity. The CNR-based cells can be designed with continuously varying band gaps (or an optimized combination of multiple gaps) to absorb the full (or selected) spectrum of solar radiation by employing CNRs of

different widths and thicknesses, achieving the highest possible intrinsic cell efficiency. In addition, first-principles calculations show that the work function of CNRs remains constant (ϕ = 4.6 eV) independent of CNR size.[64] This unique property eases the way to fabricate multigap solar cells using the same metal contacts. Calculations by Wang and Liu[65] show that an optimized 3-gap graphite solar cell has a theoretical intrinsic efficiency of ~50%, which will deliver a power conversion efficiency of >20%, even considering a high extrinsic loss of more than 50%. Fabrication of CNRs can be made economical via massively parallel processing based on lithographic patterning of graphite sheets or blocks, a technology compatible with the current Si electronics industry. Therefore, an ambitious long-term goal set out by Professor Liu's group is to develop CNR-based PV cells, while my Ph.D. thesis research has focused on developing protocols for nanopatterning of CNRs and fabricating multilayer graphene- and CNR-based photodetectors, which are prerequisite steps critical to the future development of CNR-based PV cells.

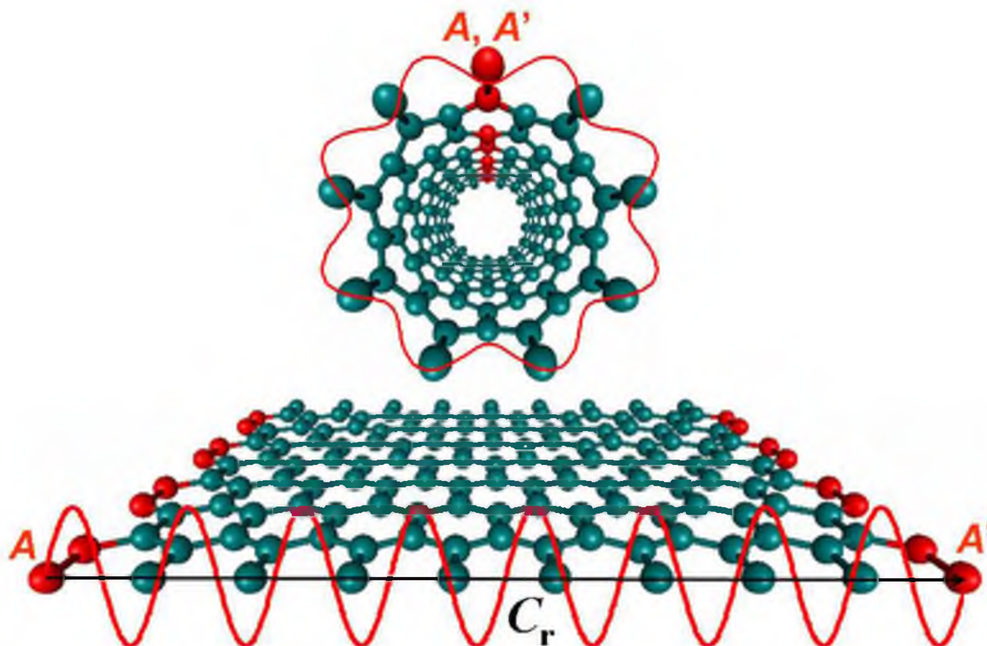

Figure 1.1 Schematic diagram of a carbon nanotube, regarded as a wrapped graphene film in a certain form.

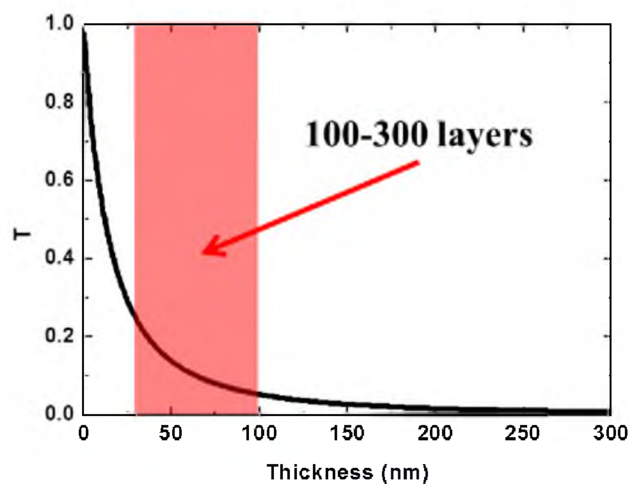

Figure 1.2 Light transmissivity of MLG or graphite in response to the thickness.

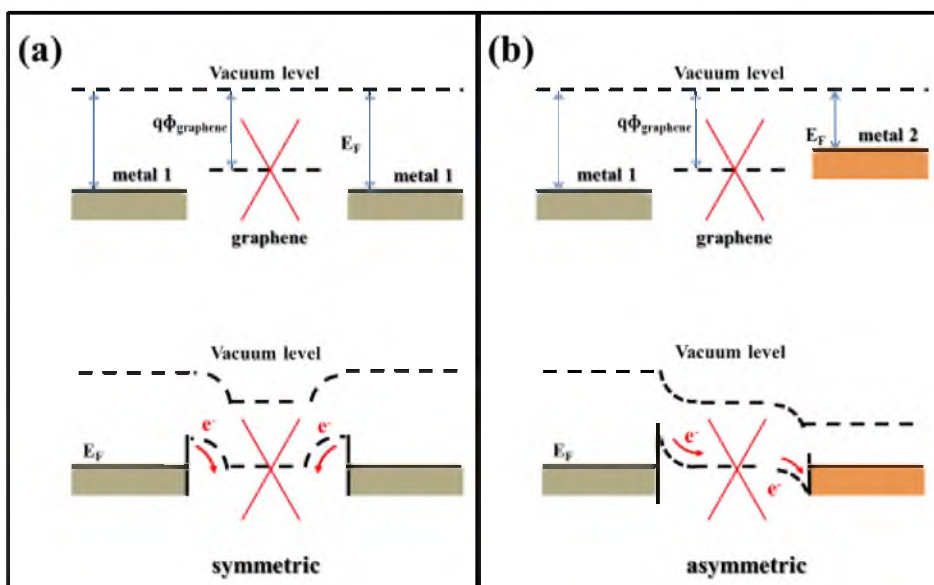

Figure 1.3 Energy band diagram showing the internal electrical field for (a) a symmetric metal scheme and (b) an asymmetric metal scheme. Upper panel: Bands of isolated metal leads and graphene. Lower panel: Bands of contacted metal leads and graphene in thermal equilibrium.

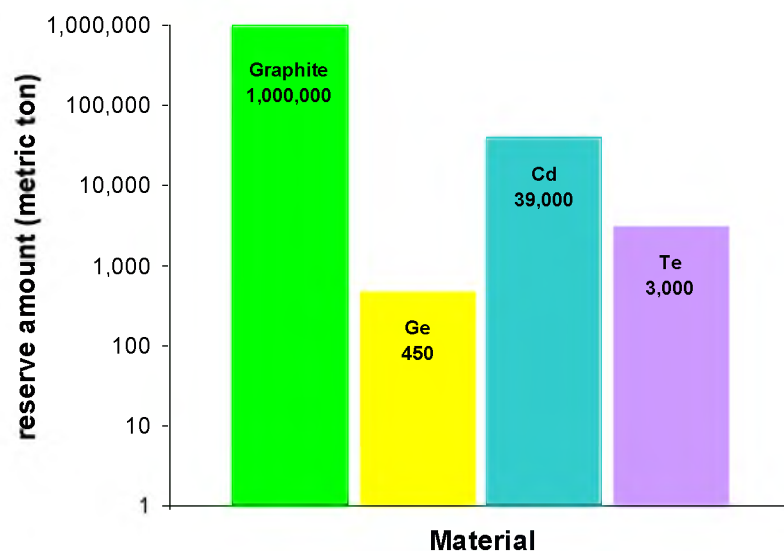

Figure 1.4 US mineral reserve amount of Graphite, Ge, Cd, and Te plotted in a log scale.

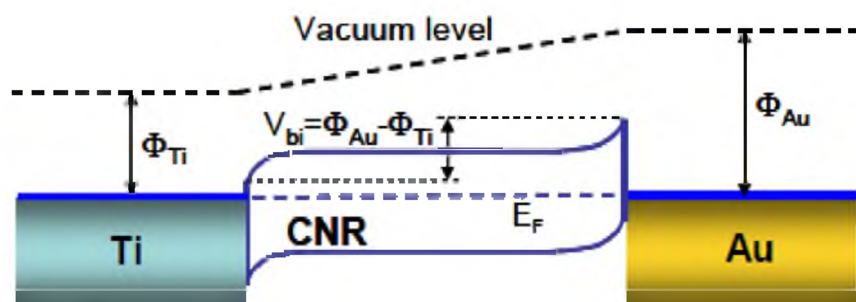

Figure 1.5 Energy band diagram of CNR-Schottky barrier PV cell using Ti and Au as electrodes.

CHAPTER 2

GRAPHITE/MULTILAYER GRAPHENE PHOTODETECTON

Graphite / multilayer graphene photodetectonIn this chapter, we introduce the experimental techniques used and present the related test results regarding the graphite/multilayer graphene (MLG) photodetectors, which are key steps before making CNRs photovoltaic cells in the future.

2.1 Raw Material Preparation

In this section, we will introduce the preparation of raw materials related to the fabrication of graphite/MLG photodetectors. Graphite selection from different vendors, graphite removal under reactive ion etching (RIE), and bonding of graphite film/flakes onto two different substrates will be discussed.

2.1.1 Graphite Selection

Since Novoselov and Geim found a method to separate one atomic graphene layer from graphite film[1] by mechanical exfoliation, graphite has become a popular choice of raw material to produce graphene with excellent properties. In our work, commercially available highly ordered pyrolytic graphite (HOPG) was used as the starting material from which MLG has been exfoliated and photodetectors have been fabricated.

Industry grade graphite (~1 x 1 cm^2 in surface area, 2 mm thick) were purchased from GE and PSI Supplies Inc., both of which claimed their HOPG has a Mosaic angle <0.5° as well as good surface quality. After surface characterization of both samples, however, we found that the GE sample has a smoother surface with smaller surface roughness, as seen in Fig. 2.1. From the optical image of both HOPG samples' surface, it is obvious that the quality of GE HOPG is much better than that of SPI HOPG. The atomic force microscope (AFM) image in Fig. 2.1c clearly shows the atomic-level smoothness of the surface of GE HOPG.

2.1.2 Graphite Etching Properties

In order to fabricate graphite/MLG nanoribbons, the process of carbon removal is necessary. Considering graphite/graphene to be highly anisotropic and chemically stable in nonoxidizing environments, a solution-based removal process is not suitable for the carbon etching. Therefore, we adopt here a dry etching approach, which effectively removes carbon material by oxidation of carbon and is capable of keeping HOPG with good surface smoothness,[66] as shown in Fig. 2.2. The high energy O_2 plasma hits the surface of the carbon layer and breaks the C–C bonds by O_2 of the high reactive energy. The product of the reaction is CO_2, which is vented away from the chamber.

Inductively coupled plasma (ICP) and capacitively coupled plasma (CCP) are usually used for the RIE process. CCP is preferred here because the anisotropic etching can be achieved through the directional electric field. O_2 ions will be driven and accelerated toward the surface of the HOPG sample (see Fig. 2.2).

Oxford Plasmalab 80 was used for the etching of HOPG. A radio frequency (RF) electromagnetic field of 13.56 MHz was preset with tunable power. We used high

vacuum conditions with a base chamber pressure of 9 x 10^{-5} mBar, while the process pressure was set to be 5 mTorr. A 90 sccm O_2 was purged into the chamber for 3 minutes to fill the chamber with oxygen before the plasma was initiated. Two etching powers of 75W and 50W were tested with the DC bias range of 63~68 Volts, leading to the etching results shown in Fig. 2.3.

It is worth noting that the O_2 plasma will not work effectively in a long-time etching process (for example, 4 hours etching) because of the raised temperature inside the etching chamber. We therefore added a cooling step (leaving the RIE machine idle for 5 minutes) after each 20 minutes of O_2 plasma etching. The tested etching rates for SPI HOPG in Fig. 2.3 are 12.7 nm/min (75W) and 6.9 nm/min (50W), respectively. The power of 75W was selected for all the carbon material etching in our research, and with this power the etch rate for GE HOPG was tested under the same condition, giving a similar rate of 14.76 nm/min. All the etching parameters are summarized in Table 2.1.

2.1.3 Cleaving and Bonding of Graphite Film/Flakes

Graphite has much stronger forces in the lateral plane than between planes so that the planar layer of carbon can be easily removed. This makes mechanical exfoliation an effective way to separate graphene/MLG from bulk HOPG. Thermal tapes from Nitto Denko Corporation were tested for successfully cleaving the HOPG surface as well as transferring the HOPG/MLG layer to a substrate. Thermal tape is preferred because it loses adhesion force at a relatively high temperature. We have been able to use thermal tape to exfoliate 20–50 μm thick HOPG films (~1 cm x 1 cm). The thin HOPG film was then transferred to a substrate (SiO_2/Si or glass wafer), which was subsequently placed on a 120 °C hot plate. We applied pressure on the tape while it was attached to the hot

substrate for ~30 seconds. Then, the thermal tape was removed, leaving behind the HOPG film bonded to the substrate. As dielectric substrates, 300-nm thick thermal SiO_2 on Si and a Corning 1737 glass wafer were tested and used for further device fabrication (Fig. 2.4). Van der Waals interaction is believed to play a role in the HOPG film bonding to substrate surface. It is found that a plasma-treated wafer has better bonding effects due to the possible removal of surface contaminations and the increase of dangling bonds on the wafer surface.

To insure the graphite surface is clean after the use of thermal tape, two main types of thermal tape, 3195 MS and 319Y-4LS, were tested based on surface contamination evaluation as well as etching resistance to O_2 plasma. Fig. 2.5 shows that the 3195MS model of thermal tape can provide a relatively cleaner surface after the release of HOPG to a substrate. In addition, the remaining tape residuals can be easily cleaned by O_2 plasma treatment.

The O_2 Plasma etching process is also used for the thinning of HOPG. However, a long-time etching will result in a rough surface, compared with the freshly cleaved HOPG. A simple thinning process of HOPG films (it is typically 20–50 μm thick after the first-time exfoliation by a thermal tape) is to repeat the cleaving process by thermal tapes so that thin and smooth HOPG films/MLG flakes can be made. By applying this method, graphene flakes of ~0.3nm thick have been achieved with a micron size.

2.2 Fabrication of MLG Photodetectors

After the HOPG films and MLG flakes were prepared, a lithographical patterning process was utilized to prepare graphite/MLG mesas in micron scale. These MLG mesas can be used to pattern CNRs (see Chapter 4 below) or to fabricate graphite/MLG flake

based photodetectors by directly depositing metal leads on them. In this section, we will first discuss the patterning process for making graphite/MLG mesas and then the fabrication process for making graphite/MLG flake-based photodetectors.

2.2.1 Etching Stop: Si

A clear-field glass mask was designed to transfer structure to a photoresist (PR) layer through optical lithography. Then, the photoresist acted as an etching mask to transfer patterns to the substrate underneath by using an etching process. Considering photoresists are mainly carbon-based materials, O_2 plasma etching would remove both graphite and photoresists. Thus, photoresists are not suitable candidates for direct transferring of patterns to graphite. To overcome this problem, an etching stop layer needed to be added between the photoresist layer and the graphite layer for both patterning of mesas and further patterning of MLG nanoribbons. Aluminum was tested first but turned out not to be a good protective (O_2 plasma etching-stop) layer for two reasons: 1) wet solution-based etching was necessary to remove unwanted aluminum after photoresist development. However, undercutting became an issue during the wet etching process, which led to the pattern transferring with a different dimension. 2) Aluminum was not bonded well with the graphite surface and usually floated off the original position after a wet process.

Because of the drawback of solution treatment, silicon was next chosen because it can be etched away by SF_6 plasma.[67] SF_6 reagents react only with Si and have no impact on graphite. During the dry RIE process, the etching of Si occurs through a reaction with F atoms, and the overall stoichiometry of the reaction of Si with atomic F is:

$$Si + 4F \rightarrow SiF_4\uparrow. \qquad (2.1)$$

The common recipe for the Si etching offers an etching rate of ~300 nm/min with Recipe 1 shown in Table 2.2. However, to eliminate the effect of O_2 and to achieve uniform Si removal, the settings for Si dry etching were improved by using pure SF_6 instead of a mixture and a lower process pressure. A lower etch rate of 25–30 nm/min was realized, but the effect of etching is greatly improved. The parameters finally used in the Si RIE process are listed in Table 2.2 as Recipe 2.

2.2.2 Photolithography Defined HOPG Mesa

With Si performing as an etching mask, the HOPG mesa arrays have been fabricated with good repeatability. The patterning process is shown in Fig. 2.6. A positive photoresist s1813 was used, in which polymer chains can be broken by UV exposure (350W Hg Lamp) and dissolved in special solvent developer like AZ MIF 300. The specific parameters used in the PR optical lithography are shown in Table 2.3.

To transfer the patterns from photoresist to the Si layer (step 4 in Fig. 2.6), the PMMA should be thick enough to survive in the SF_6 plasma for Si etching. In our test, the SF_6 RIE etching rate of s1813 was ~25nm/min, which was near the same rate of Si etch. However, PR s1813 film is normally 2.2 μm thick after spin coating (see Table 2.3), and the sputtered Si film was only ~50–100 nm, which could be totally removed in SF_6 Plasma within 5 minutes.

As mentioned in Chapter 1, a 10 nm thick graphene stack should be able to absorb a large amount of the incident light spectrum (see Fig. 1.2). Therefore, the protective Si layer may not be necessary for the thin HOPG mesa production. To verify this, the etch rate of PR s1813 in response to the O_2 plasma etching (75W) was tested and the result is shown in Fig. 2.7. The linear fit of the data in Fig. 2.7 indicates an etch rate of ~50

nm/min, which is much slower than HOPG etch rate. Thus, the PR s1813 layer can perform as a protective layer to etch through thin HOPG film, considering the coated PR s1813 thickness of ~2 μm. Using the protection from Si layer, thick (~μm thickness, see Fig. 2.8) HOPG/MLG mesas were achieved.

As shown in Fig. 2.8, a mesa array was successfully patterned by the long-time O_2 Plasma etching. Fig. 2.8c indicates a straight side wall of a 2.5-μm thick HOPG Mesa. It is worth mentioning that better edge quality was achieved when the PR layer was removed before the HOPG removal by O_2 plasma. Thin MLG mesas were also produced by positive optical lithography (see Fig. 2.9) and the quality of the mesa corner is not as good as the Si protected mesa. Cold piranha solution (3:1 mixture of sulfuric acid and 30% hydrogen peroxide) was used to remove the residual PR s1813 after the patterning of mesas. Overall, the anisotropic dry etching led to the clean edge (Fig. 2.8) and the undercut was minimized.[66]

2.2.3 Fabrication of Graphite/MLG Photodetectors

After fabricating graphite/MLG flakes/mesas, we selected two metal leads for the device source/drain contacts on the two sides. As shown in Fig. 1.5, a Schottky junction was built with two metals (such as Au and Ti), which have higher and lower work functions, respectively, compared to graphene. We have used Ti for both sides of contacts to build a symmetrically configured device (Fig. 1.3a) and Ti on one side and Pd on the other side to build an asymmetrically configured device (Fig. 1.3b) for better efficiency.

An optical lift-off process was employed in our contact deposition and the process flow is shown in Fig. 2.10. Both positive and negative lift-off methods were used, and the

negative lift-off process was found to give better lead edge quality. The parameters used for the two kinds of lift-off processes are summarized in Table 2.4.

Limited by the UV wavelength, the lift-off feature, which is confined by exposure, lies mainly in the micron scale. To better control the feature size with the clean edge of patterned metal leads, we also added an electron beam lift-off process, which has a similar procedure as shown in Fig. 2.10. In the e-beam lithography, a designed pattern from a CAD file is transferred onto an e-beam resist layer by exposing parts of the resist to the electron beam. Since the minimum feature size (or critical dimension) is proportional to the exposure light wavelength, the electron beam having a much lower wavelength provides a competitive source for patterning the metal leads.

Polymethyl methacrylate (PMMA), which is a transparent polymer produced from the polymerization of methyl methacrylate, was applied here as the e-beam resist. Two different solvents, Anisole and Methyl isobutyl ketone (MIBK), were mixed with 350K (molecular weight) PMMA and 996K PMMA, respectively, to form a two-layer structure. Both the 350K PMMA and 996K PMMA could be broken in bond by high-energy electrons, while the 350K PMMA was found to be more sensitive. Thus, the substrate surface was coated with the 350K PMMA first, and followed by a coating of the 996K PMMA. Due to the different solvents used in dissolving PMMA, the two layers of PMMA were isolated. When an electron beam is illuminated on the two-layer PMMA, the bottom 350K PMMA has more bonds collapsed. Thus, a limited undercut effect occurs after development, which helps to break the continuity of deposited metal film and promote the removal of unwanted metal on PMMA in the final lift-off process (see Fig. 2.11b).

The processing parameters for e-beam lift-off are shown in Table 2.5. Successful e-beam lithography involves tuning many control parameters, which we will later discuss in detail in Chapter 4 for the MLG ribbons fabrications.

As shown in Fig. 2.10, a metal layer needs to be deposited on the substrate after the patterning of photoresist by either optical or e-beam lithography. Both the Denton Discovery 18 sputtering system and Denton SJ20C e-beam evaporation system in the Nanofab cleanroom at the University of Utah are capable of depositing a uniform metal film. Among the two deposition methods, e-beam evaporation offers better film quality and edge smoothness with lower depositing rate.

Denton sputtering is able to coat metal as well as other materials like Si, so it is also used for the deposition of a protective layer of Si. In the sputtering system, argon ions are accelerated with high kinetic energy and bombard the atoms in a solid target material (i.e., Ti or Si), leading to the ejection of atoms from the target material. The ejected atoms move toward the bottom substrate and grow layer by layer. For the metal lead deposition implemented in the typical lift-off process, DC input is used with a low power of ~30W to minimize the substrate heating caused by plasma. This is because high temperature will always make the resist for lift-off sticky and hard to remove. The tested deposition rates for Au, Ti, and Pd in this particular Denton system are 7 nm/min, 4 nm/min, and 12 nm/min, respectively.

The electron beam source was embodied in the Denton SJ20C e-beam evaporation system and heated the raw metal materials in a crucible. The evaporated metal atoms moved upwards and arrived on the cold substrate hanging on the top of the chamber (see Fig 2.11a). The settled metal atoms formed a layer, which became thicker with more

atoms attaching. Notably, the focused e-beam directed the lifted vapor phase metal more directionally to reach our sample substrates, which is favorable to break the continuity of the deposited metal film (see Fig 2.11b).

Titanium was first tested to deposit on the substrate and to form a contact with a MLG flake. However, we found that Ti is easily oxidized in ambient conditions, which is not allowed in our application. To prevent the Ti oxidation, a gold (Au) film was deposited right after the Ti in a high vacuum for insulating Ti film from air. For an asymmetric contact configuration, Au was first applied in this device for the other lead because of its high work function compared to graphene (ϕ_{Au}~5.1eV). However, Au film cannot be attached well to the SiO_2 substrate, so Pd (ϕ_{Pd}~5.4eV) was later chosen to replace Au. In addition to this reason listed above, Pd was also chosen because of its good chemical bonding with graphene indicated by theoretical study.[68]

Since only one layer of sacrificial polymer resist (AZ nLOF 2020, see Table 2.4) was used, the “undercut effect” did not exist after developing. Additionally, the ejected metal atoms moved more randomly than the e-beam lifted metal vapor. Therefore, the sputtered metal film usually had very high coverage over the steps of the resist features and was hard to remove by dissolving the resist in the solvent. Ultrasonication can assist the lift-off process but will remove MLG flakes by overcoming the Van der Waals force between MLG and SiO_2 substrate. Fig. 2.12 shows the surface characterization of 3 initial photodetectors made by depositing ~15nm thick Ti leads on both sides of the device, which were covered by ~15nm Au film. Both metals were deposited in high vacuum conditions via sputtering and positive lift-off. The rough edge in Fig. 2.12 provides evidence that incomplete lift-off is brought about by the step covering of Ti/Au film.

After the lift-off process, devices were put in a high vacuum chamber (10^{-5} Pa) for overnight annealing at 130 ºC to reinforce the metal lead bonding to MLG mesas as well as the substrate. We noticed that the MLG flakes and micron-scale ribbons easily broke along their grain boundaries after annealing or laser illuminations, owing to the stress relaxation from Ti/Au metal leads (see Fig. 2.12d and Fig. 2.12e).

We offer three contributing factors to the phenomenon: 1) Ion-induced plastic strain in metal leads as well as atomic displacement[69]: Ar ions or possible Ti/Au ions flowing into the layered film caused strain. During the sputtering process, atoms moved to grain boundaries and led to the build-up of compressive strain. 2) Grain coalescence or heat absorption occurred during the annealing process.[70-72] 3) The similar thickness in nanometer scale: both Ti and Au films are ~15nm thick so that the strain was easily built up.[73] The metal layer easily rolled up with very large curvature (see Fig. 2.12c and Fig. 2.12f). In addition to these factors, the wrapping edge as a result of incomplete lift-off also promotes the initiation of film deformation.

This lead-deposition-induced strain effect provides evidence that strain can be built up on graphene flake, which offers a simple and effective method for making a strained graphene device. By constructing a bilayer metal lead on the two sides of a graphene flake, a “spring exerciser” forms and the compressive strain will lead to a tensile strain in the attached graphene (see Fig. 2.13).

For the suspending or strained graphene, a lot of interesting properties can be studied.[39, 70, 74, 75] Inspired by our experimental discovery, we propose a new methodology to achieve suspended and/or strained graphenes, similar to the nanomechanical architecture of bilayer semiconductor nanomembrane devices fabricated before.[76] The

strain is caused by the stress relaxation of the bilayer of metals (or other possible materials, like silicon), which is tunable through the thickness engineering of the two metal films, lead deposition methods, thermal treatment, or even laser curing.[77] Critical point drying should be involved to get rid of the surface tension effect during the sacrificial layer (i.e., PMMA or s1813) releasing. The electric performance of the suspending and/or strained graphene device can be directly researched over the source/drain contact scheme.

In the end, to eliminate the edge folding defects, we used e-beam evaporation for anisotropic growth of metal film and e-beam (or optical negative) lift-off processes instead of positive lift-off. Furthermore, a thickness mismatch was predetermined with no equal or similar thicknesses for the two metal layers. Fig. 2.14 shows devices fabricated with asymmetric metal contacts by optical negative and e-beam lift-off. Thin MLG mesas were directly fabricated by employing O_2 RIE with the protection of PR s1813 layer (see Fig. 2.9 and Fig. 2.15a).

Color contrast on proper dielectric (i.e., SiO_2/Si) substrate under an optical microscope is a convenient way to estimate the thickness of graphene.[78, 79] As an almost transparent layer with high optical transmission,[17, 33, 37] graphene is more visible in reflection than in transmission. The visibility in reflection is greatly enhanced by a certain thickness of SiO_2.[37] Thus, the optical difference under visible light source guides our experiment for thickness estimation. Fig. 2.14a shows different graphite/MLG islands produced from the exfoliation of HOPG, and some 1-micron wide MLG ribbons were made as well. Color difference in Fig. 2.14a indicates the different layer of graphite.

Using the graphite/MLG flakes on SiO_2/Si substrate, metal contacts were deposited to form symmetric and asymmetric device configurations. The Ti (ϕ~4.3eV) layer on both sides of graphite flakes (ϕ~4.6eV) forms an internal electric field with the opposite direction of electron flow (See Fig. 1.3a). The same direction of electron flow can be achieved by using Pd to replace one side of Ti contact (see Fig. 1.3b).

Fig. 2.14b–e show different photodetectors fabricated based on graphite/MLG flakes, and Fig. 2.14e indicates the different edge quality of metal leads by two different lift-off processes (Ti leads by positive lift-off and a Pd lead by negative one). To precisely control the gap distance between the two metal leads and investigate the influence of lead/MLG coverage, the metal leads produced by e-beam lift-off were used with smaller and more controllable sizes (see Fig. 2.15).

2.3 Photoresponse of Graphite/MLG Photodetectors

Several Ti/HOPG/Ti photodetectors were verified under the laser illumination experiment for the photocurrent detection. Even with this symmetric contact scheme, large photoresponse was observed. Photodetectors based on asymmetric contact schemes of Ti and Pd were also verified. It is shown that the electron carriers flow from the high work function material (Pd) to the low work function material (Ti), which is consistent with the photocurrent generation by the internal electrical field mechanism. This confirmation can be useful for future PV device fabrication too.

2.3.1 Photodetectors with Symmetric Metal Scheme (Ti–Ti)

The graphite/MLG flake (without patterning into rectangular mesas)-based devices were first tested for the photoresponse. A continuous-wave (CW) laser of two

wavelengths (350 nm and 488 nm) was used together with a lock-in amplifier (Standford SR830) to capture the photoinduced current signal (see Fig. 2.16). The power distribution in a CW laser spot, typically 500 nm in diameter, basically follows the Gaussian distribution law. We used a simple 1D Gaussian distribution in a laser beam to determine the actual laser power absorbed in the active area of our devices. For a certain laser power, a 488 nm (2.54 eV) laser contains more incident photons than a 350 nm (3.54 eV) laser. In the photocurrent detection system, a pre-amplifier is also used to enlarge the photoinduced current signal. The chopper was set at ~300 Hz in our experiment and the laser spot of ~500 μm in diameter to cover the whole detection area of our device.

The graphene-based photodetectors have been reported recently.[35, 38, 40, 43, 52, 57, 58, 80] Both symmetric and asymmetric metal schemes were tested in the previous research. Our results confirmed that the HOPG/MLG-based photodetectors could achieve great photoresponse. Fig. 2.17 shows a Ti/HOPG(~50 nm thick)/Ti device with an asymmetric contact area, in which the thickness of Ti/Au contacts is 30–40 nm in total (this typical thickness of leads applies to all our devices discussed later). A chopped UV laser of 350 nm illuminated the whole detection area of the device. Because the contact metal layer is very thin, the laser beam is able to partially penetrate and reach the vertical metal/HOPG internal electric field, where this portion of light is absorbed to generate electron flow. In addition, the work function difference at the metal/HOPG boundary forms a field in lateral direction,[38, 57] which leads to the generation and drift of free electrons upon photoexcitation. Photocurrent generated at the two internal fields will contribute to the overall current signal. In the symmetric lead configuration, the electric field drives the electrons from the high work function material (HOPG) to the low work function

material (Ti). For this reason, photocurrent flow from both Ti leads to the mid HOPG flake, and the overall current generated by the internal electric field was the difference of the electron flows from opposite direction.

We believe the PTE effects also played a role in the overall net photocurrent.[45, 52] HOPG/MLG flakes are usually composed of terrains with different thicknesses/heights (see Fig. 2.14a). Based on the PTE theory,[44] hot carriers tend to diffuse from a low graphite terrain to a high terrain. Thus, the structural composition of a HOPG flake/mesa is important to the influence of PTE effects. Researchers believe that photocurrent has a nonlinear dependence of $T^{1-\beta}$ ($\beta > 1$), while the laser power (P) dependence is described as $I \propto P^{2/(\beta+1)}$, if the heat flow is regarded as a radial wave.[44] This nonlinear dependence might be one of the reasons for the saturation of current in Fig. 2.17c.

In Fig. 2.17b, it is observed that the photocurrent was dramatically changed based on the on/off switching of the laser. With the increasing input laser power, the output photocurrent signal increased gradually. The background noise is relatively high because a laser chopping frequency of 300 was used, which is a multiple of household AC (60 Hz). Thus, in the following tests, a frequency of 280 Hz was used to minimize the household AC signal interference.

Fig. 2.17c shows the photocurrent signal from this device as a function of laser power. At the high power range, the rise of photocurrent amplitude becomes smaller in response to growing photon intensity. A saturation of photocurrent is displayed at high laser power, which agrees with previous work[35, 44] and may contribute to the limited thermal gradient at a high power range. Furthermore, the high-temperature-induced resistivity change of graphene/graphite, as reported before,[46-49] may lead to the reduction of conductivity of

the device and thus to limit the increase of photocurrent signal in response to the raising laser power.

The effective laser power in the active area of our device from our estimation and calculation is ~0.18 mW when laser power was set to 1.0 mW. The active area of this device can possibly consist of three parts: (a) the 300 nm photovoltaic-like junction region around the metal/graphite boundary, (b) the metal lead covered graphite interface (leading to the possible photons loss by the reflection of light), and (c) the exposed graphite flake in between Ti contacts, which can contribute to the net current by the drifting of hot electrons. The final estimate of the photoresponse for the Ti/HOPG/Ti device at 1.0 mW is ~ 0.3 mA/W (1.67 mA/W with laser power of 0.1 mW), which is much higher than some other reported graphene-based photodetectors at zero gate bias.[38, 51]

2.3.2 Photodetectors with Asymmetric Metal Scheme (Ti–Pd)

Asymmetric metal contact configurations on exfoliated HOPG flakes, which create an asymmetric internal electric field between the source and drain contacts, can help to direct the photocurrent and has been used for efficient and ultrafast photodetection.[35] Thus, a simple Ti/HOPG/Pd device was built to achieve a better photocurrent signal in response to the photosource (see Fig. 2.18). Compared with the Ti–Ti device shown in Fig. 2.17, a higher photocurrent signal was achieved with less detection area. The asymmetric internal electric field is believed to lead to the enhancement of the photocurrent signal, due to the coherent electron flow direction. Moreover, a 488 nm wavelength laser, instead of 350 nm in the Ti/HOPG/Ti device testing, was used with

more photons by the same laser power output, which also leads to the improved photocurrent response.

During this test, the blue laser with chopping frequency of 280 Hz was used to minimize the effect of the background signal from the household AC. 488 nm laser powers of 13 μW to 1 mW were applied. In contrast to the Ti/HOPG/Ti photodetector shown in Fig. 2.17, the estimated effective power is 0.072 mW with the overall laser power of 1.0 mW, which is much lower than the effective power in the Ti/HOP/Ti device due to a smaller active area. However, the photocurrent signal is much higher at the same laser power (i.e., 1.0 mW). Under the 1.0 mW laser, a 5 times higher photoresponsivity of 1.8 mA/W was achieved with smaller HOPG thickness, compared with the symmetric-lead device. If we take into account the photons per power density, the 488 nm laser used in this experiment contains ~40% more photons than the 350 nm laser. Then, we still get a much higher photoresponsivity in this asymmetric-lead device. We can attribute this remarkable photoresponse to the efficient asymmetric lead scheme and the short channel length. Based on the test shown in Fig. 2.18b, the photocurrent vs. laser power curve is displayed in Fig. 2.19, which also shows a near-saturation trend.

Both symmetric and asymmetric photosensors were fabricated with great photoresponse. Next, we built a three-terminal device with one Pd contact and two Ti contacts, using a HOPG flake ~50nm thick, to investigate the contribution of Ti/HOPG and Pd/HOPG junction to the photocurrent. This three-terminal device is shown in Fig. 2.20a. The Pd lead was sputter-deposited by a negative lift-off process (marked as L1 in Fig. 2.20a), while the two Ti leads were prepared through a positive lift-off process with a clean edge (marked as L2 for the wide Ti channel and L3 for the narrow Ti channel in

Fig. 2.20a). By choosing two contacts from L1, L2, and L3 as the source/drain channels, we obtained the photocurrent signal under a 488nm blue laser of 0.23 mW working power as shown in Fig. 2.20b–d.

From Fig. 2.20b–d, high photocurrent was achieved at a relatively low laser power (photoresponsivity as high as ~9.9 mA/W). Fig. 2.20c and Fig. 2.20d indicate that there is no obvious difference based on if the channel width is changed on the Ti side electrode in the asymmetric Ti–Pd scheme. So we conclude that the photocurrent signal is mainly caused by the Pd/HOPG rather than from the Ti/HOPG junction. The ON/OFF ratio of this device is around 300.

The Ti/HOPG/Ti configuration achieves a photocurrent of 204 nA, which is lower than the Ti/HOPG/Pd asymmetric device. However, considering the smaller band bending of HOPG at the Ti/HOPG junction as well as the symmetric internal electrical field, the photocurrent signal is still high. The short distance of ~200 nm between the two Ti leads may account for this phenomenon. Because of this small gap, some of the photogenerated free carriers can arrive at the leads without scattering with local defects.

To study the effects of lead/graphite contact geometry, we also prepared a device based on a MLG mesa by patterning a MLG flake. A 13 x 24 μm MLG mesa with ~20 graphene layers is shown in Fig. 2.21. The optical image in Fig. 2.21a shows different layer thickness contained in the HOPG mesa block on SiO_2/Si substrate by the color difference. AFM characterization in Fig. 2.21b and Fig. 2.21c confirms the MLG structure and size and indicates the average thickness of 8–10 nm.

Both titanium (T) and palladium (P1, P2, P3) lead were deposited through a metal evaporation method and modified by e-beam lithography, which helps achieve the clean

edge. The thickness of all four leads is ~30nm. As shown in Fig. 2.22a, the 3 right Pd leads are 1.3, 5, and 10 microns wide from top to bottom, respectively, and the contact width of the Ti lead and bottom MLG mesa is 22 μm. The gap between Ti and Pd leads is 3 μm, while the gap between adjacent Pd leads is 2 μm. The photocurrent measurement was conducted under a 450nm blue laser with 100 μm spot size at the fiber outlet, and the laser fiber was placed ~1 mm above the sample surface to direct the laser beam onto the sample. This laser through the modulated fiber has a uniform distribution within the spot. A 450 nm wavelength laser was used in this experiment with a chop frequency of 77 Hz, which was used for later photocurrent tests by the preamplifier.

For the asymmetric connections, the 3 channels with different Pd lead widths were placed separately into the circuit for photocurrent testing. The results in Fig. 2.22b indicate that the photocurrents generated in the 3-leads scheme are all the same (11.7 μA), and the photoresponsivity of 65 mA/W was achieved with only ~10 nm thick graphite, which is much higher than any of the previous photodetectors. We attribute this to the overheating of the device (laser power as high as 114 mW) so that the photothermo effect dominates. The high thermal gradient causes the drifting of hot electrons, and the same amount of photocurrent signal was generated through all the 3 channels.

To summarize, in this chapter, we realized the thinning of commercially available graphite and its bonding to two different glass substrates. Graphite films and graphite/MLG islands were successfully prepared. With the protection from Si Layer on top, optical lithography together with dry RIE was utilized for the fabrication of graphite/MLG mesas. Graphite/MLG-based photodetectors were fabricated and tested, based on graphite/MLG islands with irregular shapes and MLG mesas with a

photolithographically defined rectangular shape. We applied a photocurrent detection system using laser as a light source and the resulting photoresponse from our devices showed noticeable enhancement compared with conventional graphene photodetectors. Graphite/MLG photodetectors based on symmetric and asymmetric metal schemes were studied and Pd–Ti showed better photoresponsivity because of the existence of an internal field at both lead/graphite boundaries and interfaces. We also found that short channel length and the limited thermal gradient at high temperatures may be responsible for the saturation of photocurrent at high power.

Table 2.1 Parameters for O2 RIE of HOPG

Parameter	Setpoint
Pumping to Base Pressure	9 x 10^{-5} mBar
Oxygen Purge	90 sccm @ 3 min
Process Pressure	5 mTorr
Plasma Initiation	75W or 50W

Table 2.2 Parameters used for SF_6 plasma etching

Parameter	Recipe 1	Recipe 2
Pumping to Base Pressure	9 x 10-5 mBar	9 x 10^-5 mBar
Gas Purge	SF6/26sccm & O2/3.5sccm @ 3min	SF6/10 sccm @ 3 min
Process Pressure	75 mTorr	15 mTorr
Plasma Initiation	50W	50W
DC Bias	NA	35 V
Etch Rate	300 nm/min	25–30 nm/min

Table 2.3 Parameters used for PR 1813 optical lithography

Parameter	Setpoint
Spin Speed	2000 rpm
Spin Time	45 sec
Prebake Temperature	110 °C
Prebake Time	60 sec (silicon wafer), 90 sec (glass substrate)
Exposure Dose	75 mJ/cm^2
PR Film Thickness	2.2 µm

Table 2.4 Parameters used for positive and negative lift-off process (SiO_2/Si substrate)

Positive		**Negative**	
Parameter	**Setpoint**	**Parameter**	**Setpoint**
Pre-bake	150°C @ 5min	Pre-bake	150°C @ 5min
PR LOR-10B spin coating	2000rpm @ 45sec	PR AZ nLOF 2020 spin coating	3000rpm @ 40sec
LOR-10B thickness	~1 µm	AZ nLOF 2020 thickness	~2 µm
Bake	150°C @ 5min	Bake	110°C @ 1min
PR s1813	2000rpm @ 45sec	UV Exposure	11 sec @ 75 mJ/cm^2
Bake	110°C @ 1min	Developer	AZ 300 MIF @ 45-60 sec
UV Exposure	12-15 sec @ 7 mW/cm^2	Lift-off (AZ Kwik striper)	90°C @ >40min
Developer	AZ 300 MIF @ 20-30 sec	Lift-off (acetone)	90°C @ >40min
Lift-off (acetone)	remove PR s1813		
Lift-off (AZ 300 MIF)	remove LOR-10B		

Table 2.5 Parameters used for e-beam lift-off process

E-beam Lift-off	
Parameter	**Setpoint**
350K PMMA solution	in anisole (0.995 g/ml)
Spin coating	500rpm @ 5sec + 3000 rpm @ 40 sec
Bake	130–140°C @10min
996K PMMA solution	in MIBK (0.801 g/ml)
Spin coating	500rpm @ 5sec + 3000 rpm @ 40 sec
Bake	130–140°C @10min
E-beam exposure	400–500 µC/cm^2 in area dose
Developer	1:3 MIBK:IPA @ 70 sec
Rinse	IPA @ 20 sec
Lift-off (Acetone)	90–100°C @ 40min

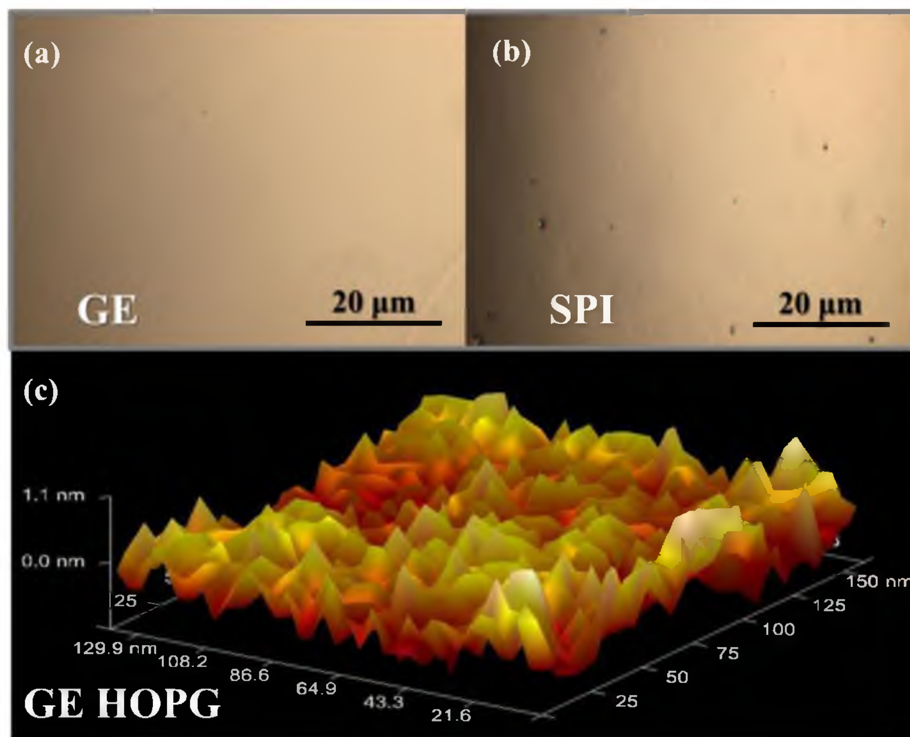

Figure 2.1 Surface characterizations of two HOPG samples. (a) and (b) Optical image of GE and SPI HOPG sample surfaces, respectively. (c) 3D AFM scan of GE HOPG. The local RMS surface roughness is only several angstroms.

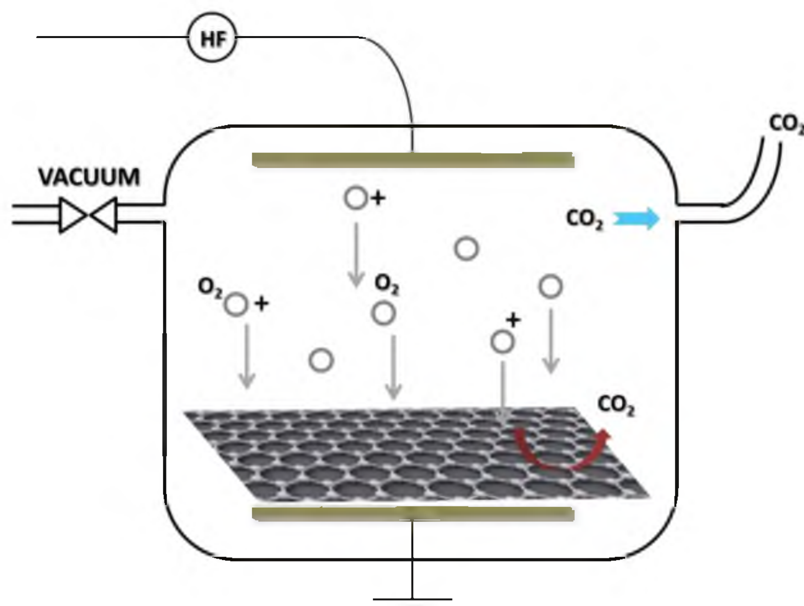

Figure 2.2 Schematic drawing of the O2 plasma etching process in a capacitive reactive ion etching (RIE) chamber.

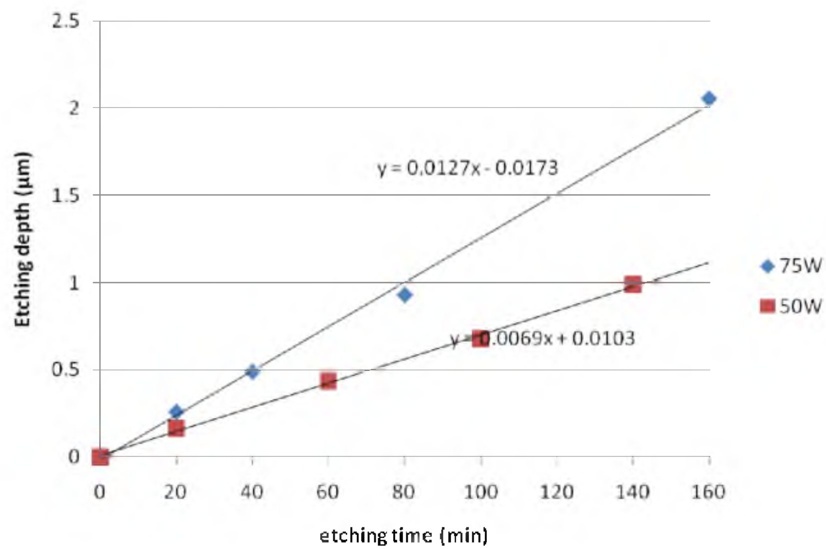

Figure 2.3 O2 Plasma etching of SPI HOPG at two different powers, all other parameters held constant.

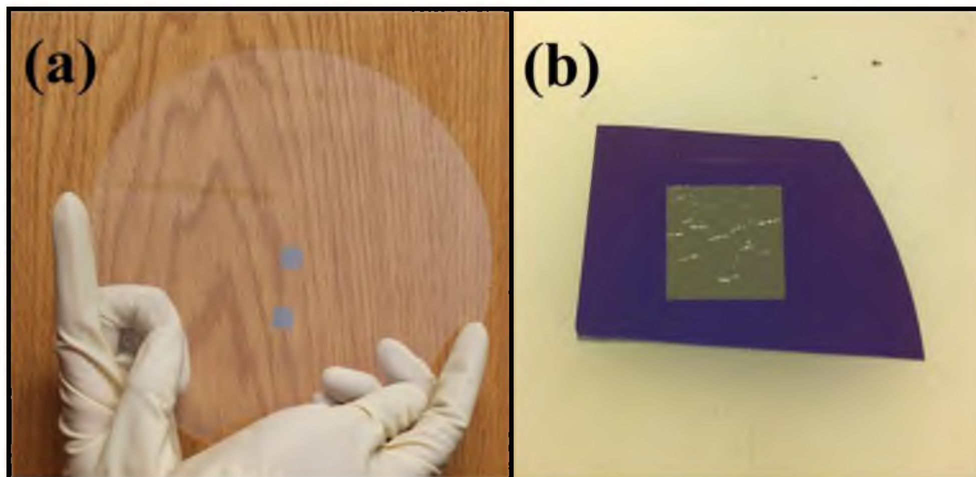

Figure 2.4 Optical images of HOPG films bonded on (a) glass wafer and (b) SiO2/Si.

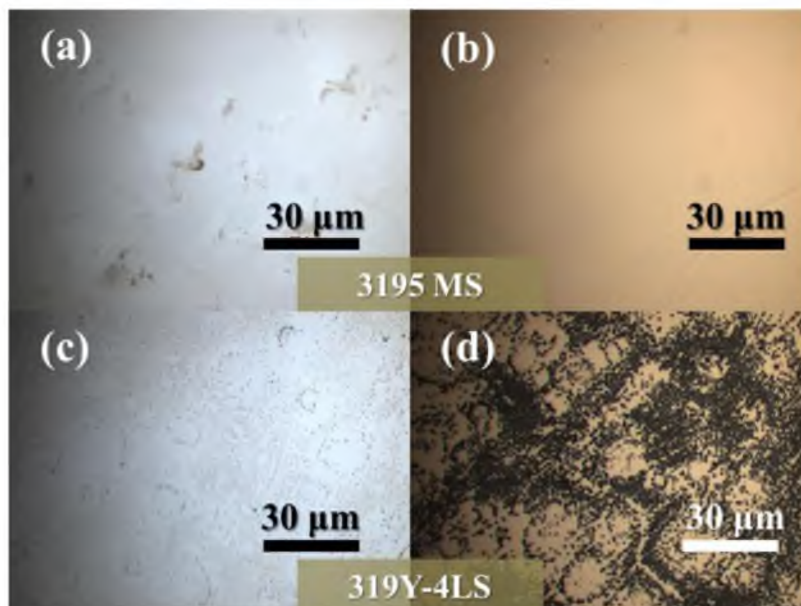

Figure 2.5 Optical images of HOPG surface after being released from thermal tape (a) 3195MS and (b) 319Y-4LS, respectively. (b) and (d) resulting surface with 20 minutes O_2 plasma etching of (a) and (c), respectively.

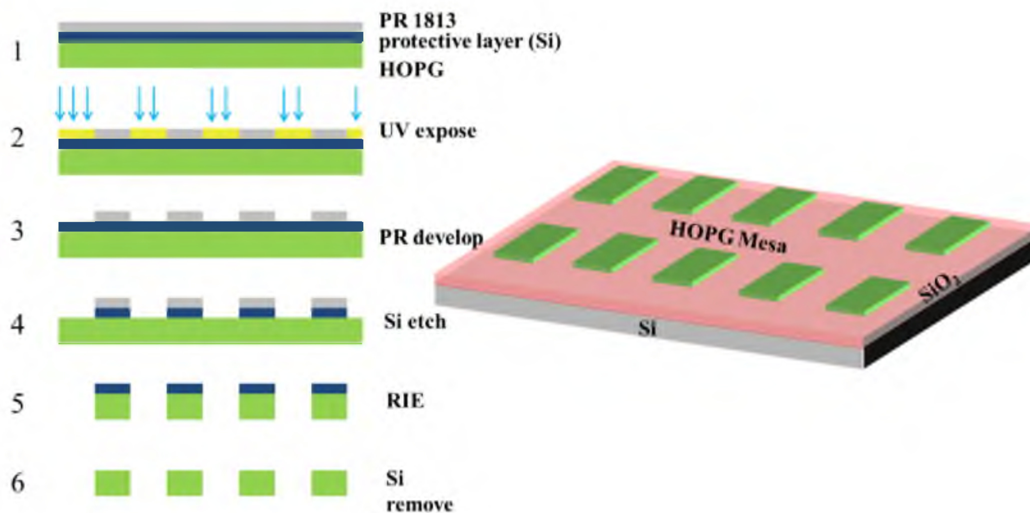

Figure 2.6 HOPG patterning flow. Left: schematic process flow of HOPG patterning. Right: schematic 3D view of a patterned HOPG mesas array on SiO2/Si substrate.

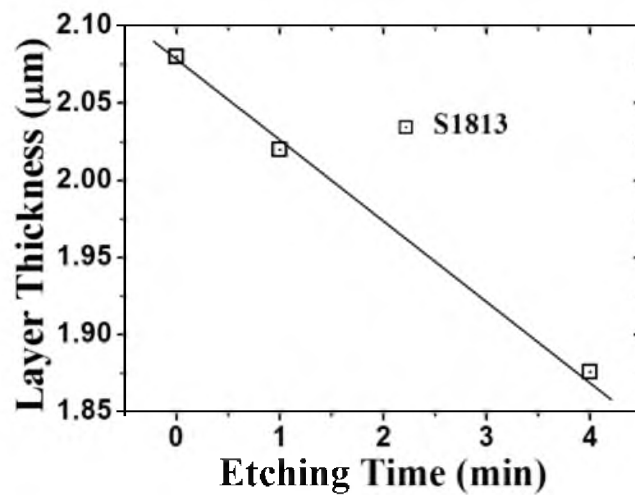

Figure 2.7 Etching test of PR s1813 under O2 RIE at 75W.

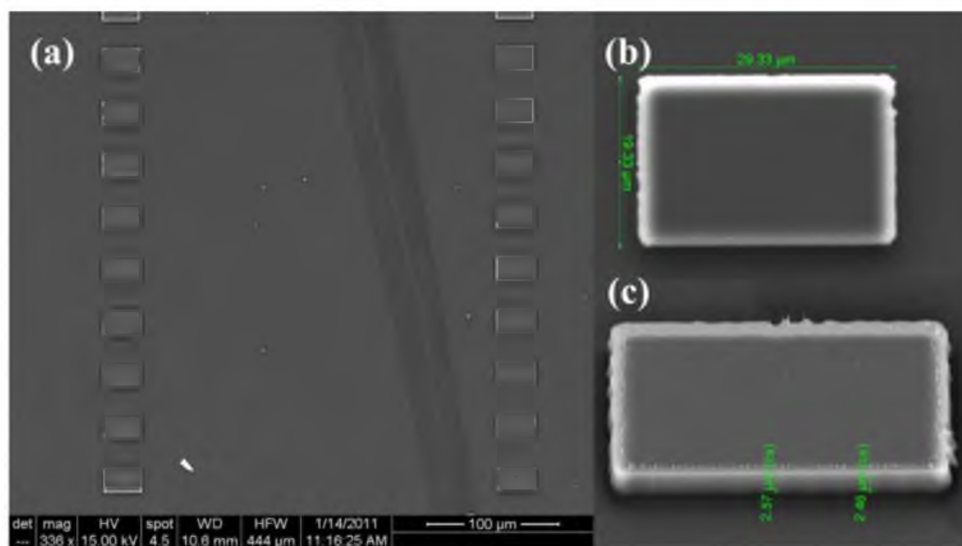

Figure 2.8 Scanning electron microscopy (SEM) images of patterned HOPG mesas. (a) 20 x 30 μm mesa array, (b) close-up image of a HOPG block with clean edge, and (c) tilt of 30° to estimate the thickness of HOPG mesa.

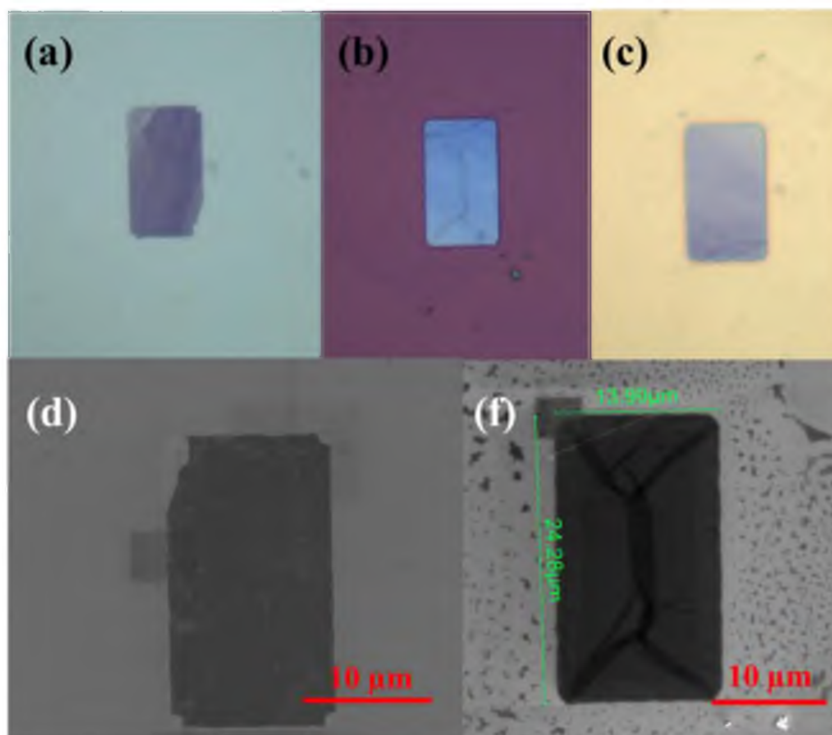

Figure 2.9 Optical and SEM images of patterned MLG mesas (~ 15 μm x 25 μm). (a)–(c) Optical images of mesas with thickness in a range of 5–30 nm; (d) and (f) SEM images of mesas shown in (a) and (b), respectively. Residual of masking PR s1813 was left after the O_2 RIE process to pattern MLG mesas.

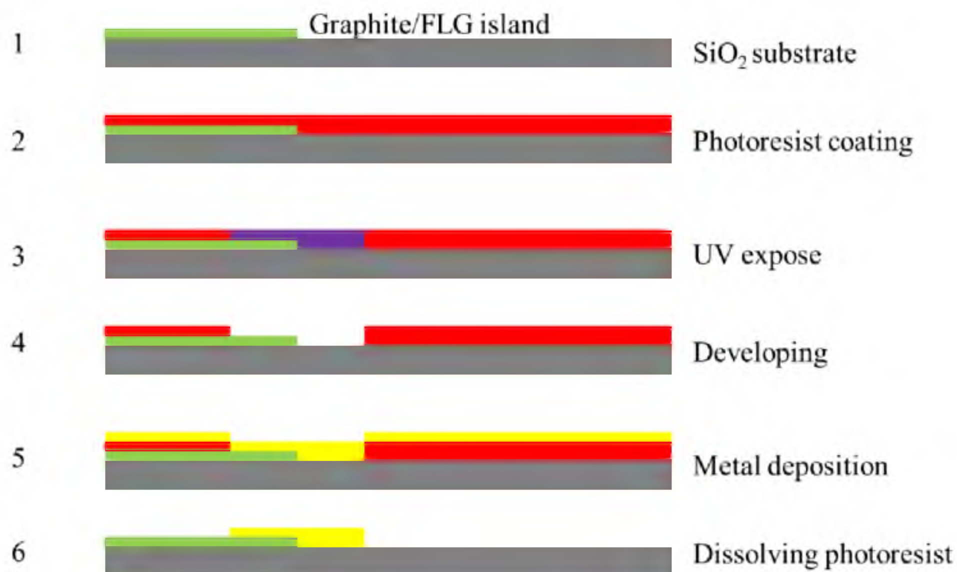

Figure 2.10 Schematic process flow of a positive lift-off of a metal lead.

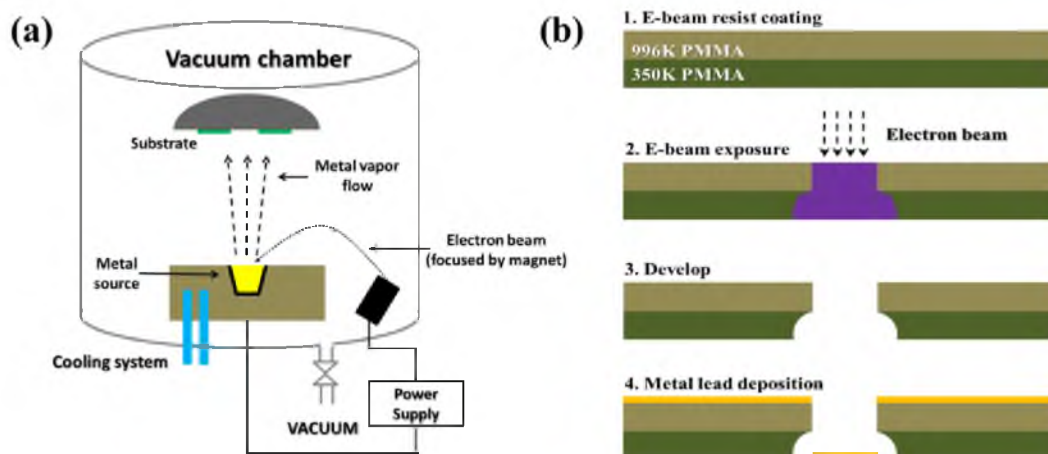

Figure 2.11 Schematic drawing of the e-beam evaporation system as well as the e-beam lift-off process. (a) Metal evaporation system view. A high power of 6.5 kV is used to elevate electrons for metal source heating. (b) A typical flow chart for the e-beam lift-off process. The final lift-off step is neglected here. The benefit of the two-layer structure is shown in step 4, which indicates the break in continuity of the metal film.

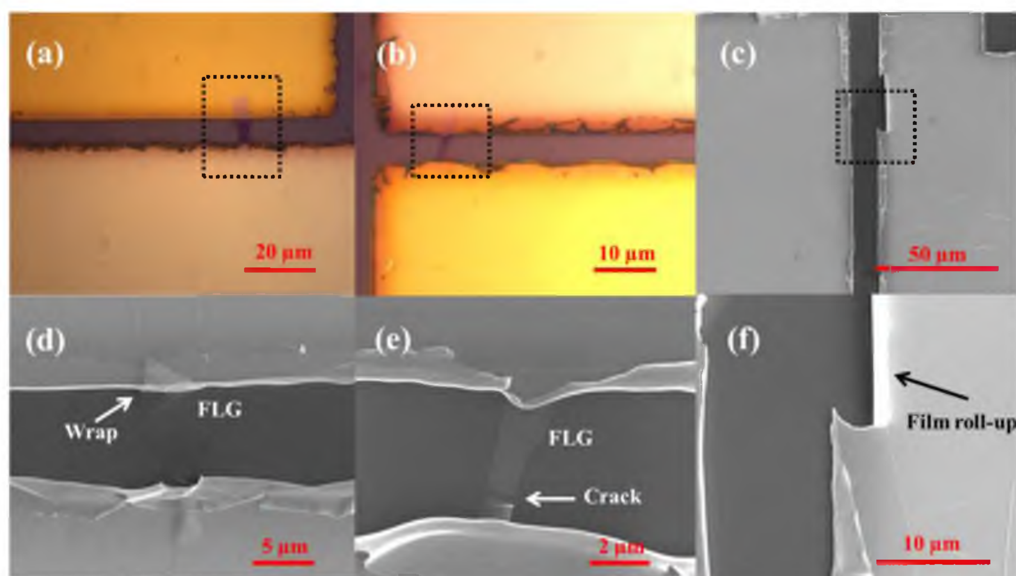

Figure 2.12 Optical and SEM characterization of graphite/MLG island photodetectors. 15nm/15nm Ti/Au metal leads were deposited on the two sides of MLG island. The thicknesses of MLG islands are typically among 5nm–10nm. (a) and (d), (b) and (e) optical and SEM images for the two devices. The dark dot boxes in (a) and (b) confine the areas of images shown in (d) and (e), respectively. Crack and wrap occurred after overnight anneal. (c) and (f) SEM images of another strained graphene device, which contains rolled-up Ti/Au film.

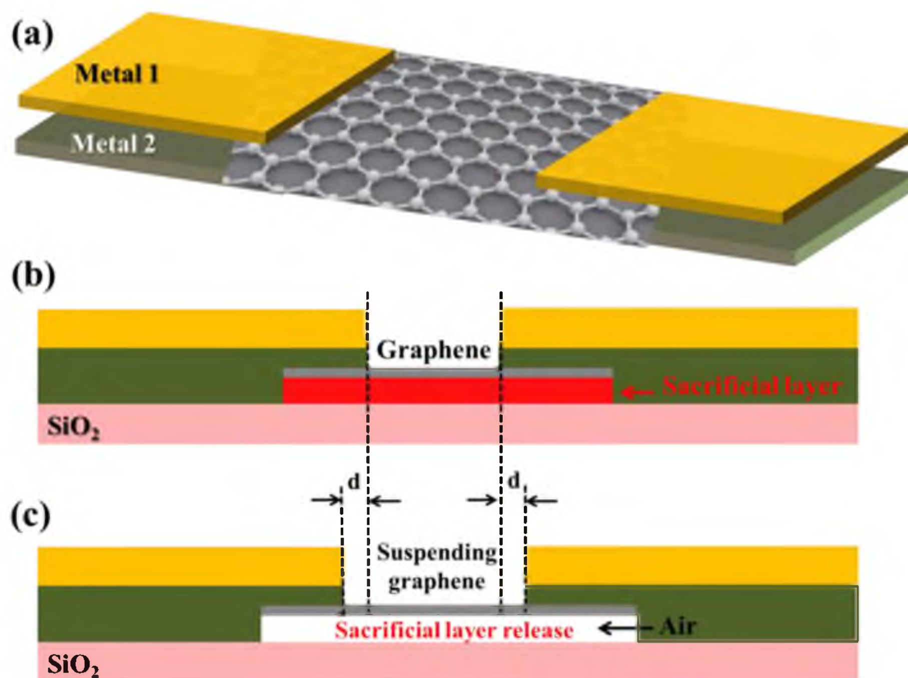

Figure 2.13 Schematic exhibition of a strained graphene device. (a) 3D drawing of a metal/graphene/metal sandwich structure. (b) and (c) Schematic cross-section view of a proposed suspending and strained graphene fabrication process. d shows the x-direction displacement of graphene flake. The bilayer of metals can be used to sandwich the graphene in (a) or load on graphene all together in (b) and (c).

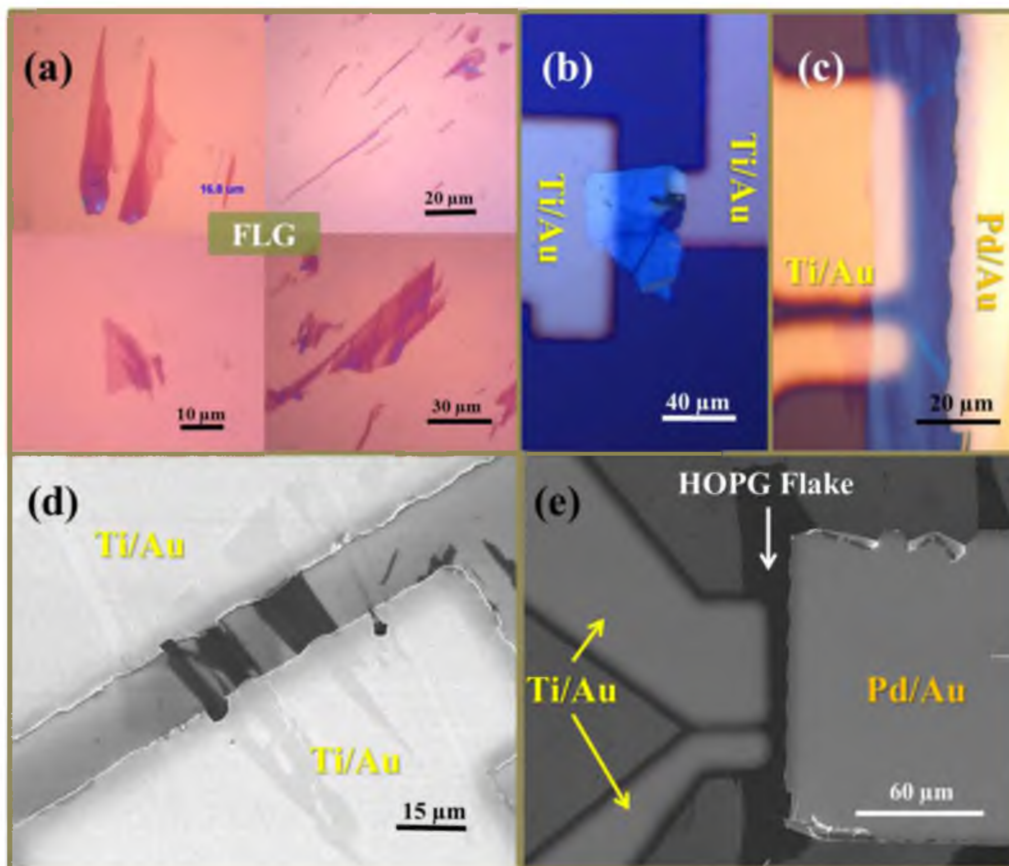

Figure 2.14 Surface characterization images of graphite/MLG flakes together with some typical photodetectors. (a) Optical images of MLG flakes and ribbons on SiO2/Si substrate after mechanical exfoliation from HOPG. (b) and (c) Optical images of symmetric (Ti-graphite-Ti) and asymmetric (Ti-graphite-Pd) photodetectors. (d) and (e) SEM images of photodetectors with two different metal schemes. (c) and (e) show the 3-terminal connection for the same device. All the leads are covered with a protective Au layer.

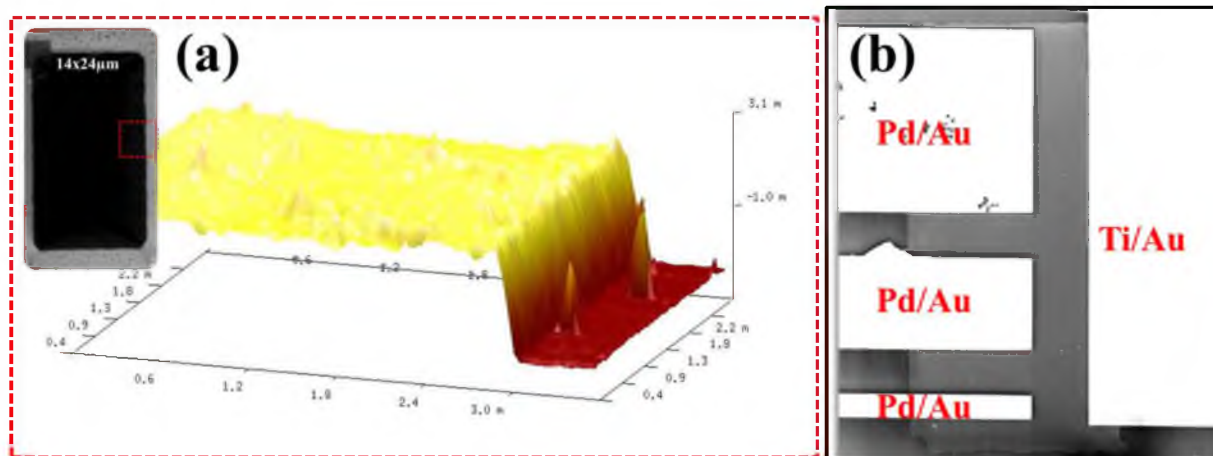

Figure 2.15 A RIE defined HOPG rectangular block together and e-beam lead deposition by lift-off. (a) The surface characterization of the RIE tailored HOPG mesa by AFM, and the thickness shows 30nm indicating ~100 graphene layers stacking. Inset shows a SEM Image of the HOPG mesa. (b) SEM image of a Ti/HOPG/Pd device with the lead deposition by e-beam lift-off. The widths of Ti leads on the left are 10μm, 5μm, and 1.3μm (from top to bottom), respectively.

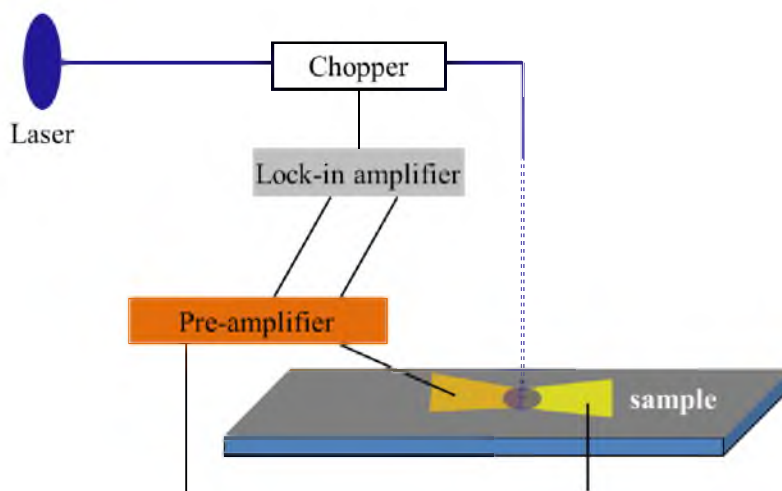

Figure 2.16 Schematic illustration of a photocurrent detection system.

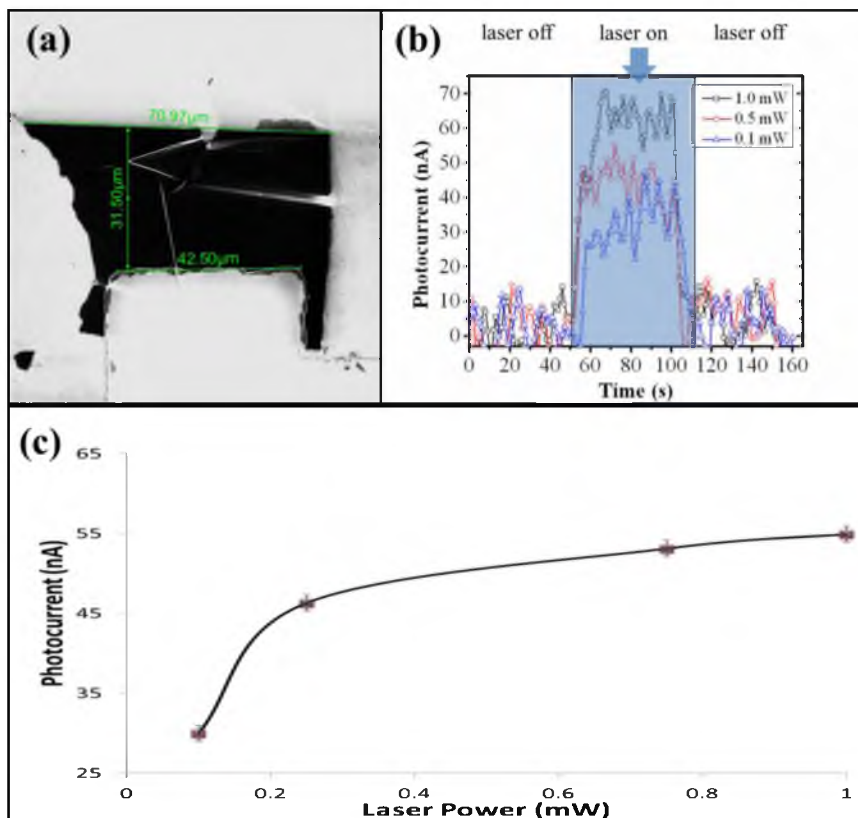

Figure 2.17 Surface characterization and photoresponse test of a Ti/HOPG/Ti device. (a) SEM image of the Ti/HOPG/Ti device. (b) Photocurrent as a function of time. (c) Photocurrent signal with error bar in response to the laser power.

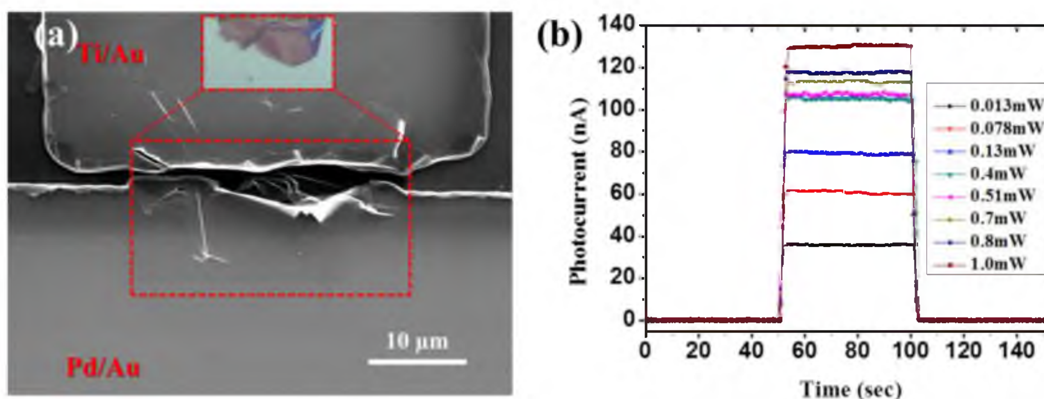

Figure 2.18 An asymmetric Ti/HOPG/Pd photodetector. (a) Device SEM image. The Ti/Au and Pd/Au leads gap is ~300nm wide at the closest. Inset shows the optical image of the HOPG flake (~35nm thick in average) before the lead deposition. (b) Photocurrent in response of testing time duration.

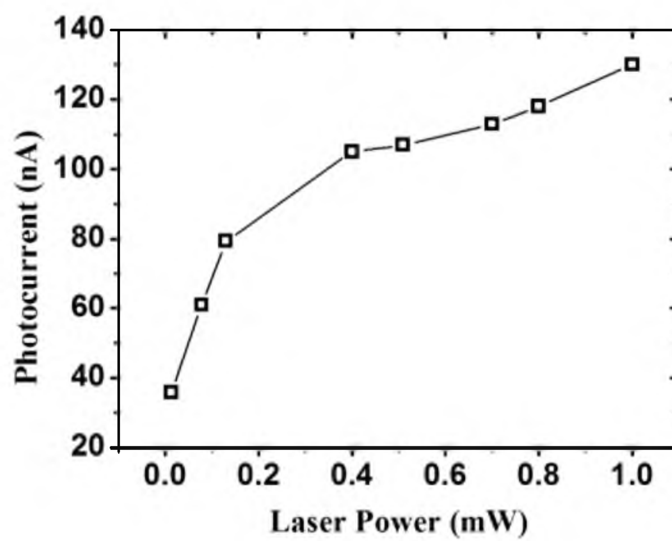

Figure 2.19 Photocurrent as a function of laser power input.

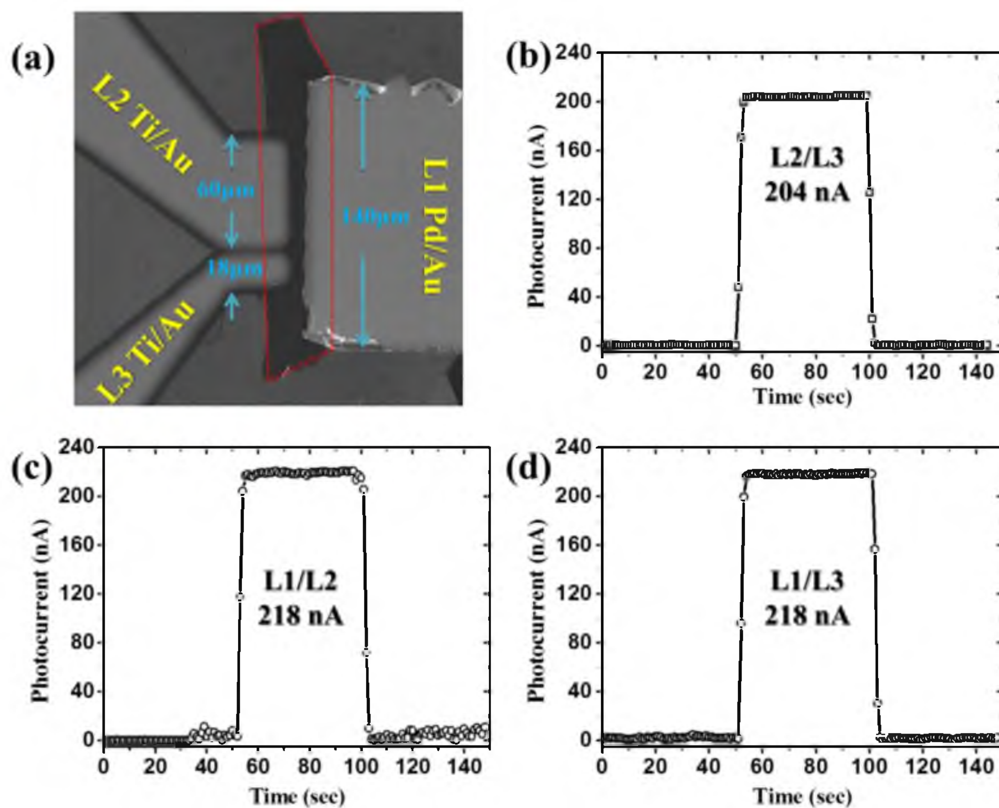

Figure 2.20 Three-terminal device and photocurrent test. (a) SEM image of the three-terminal device, which is composed of 2 Ti- and 1 Pd- leads (30nm thick in overall with covered Au). The gaps between Ti and Pd leads are 10 μm between L1 and L2 and 7 μm between L1 and L3. The red dotted frame confines the HOPG flake on top of the SiO2/Si substrate. (b), (c), and (d) Photocurrent vs. time for L2/L3, L1/L2, and L1/L3, respectively.

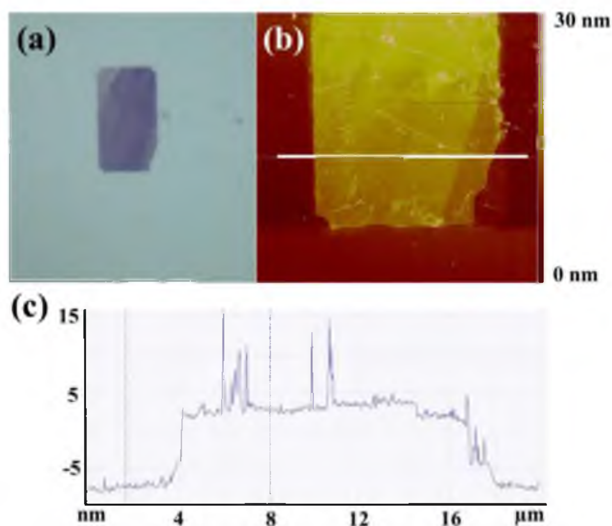

Figure 2.21 Surface characterization of a 13x24 µm HOPG block. (a) Optical image of the HOPG block. (b) AFM scan of the part of the HOPG block. (c) Depth profile along the sectional white line shown in (b).

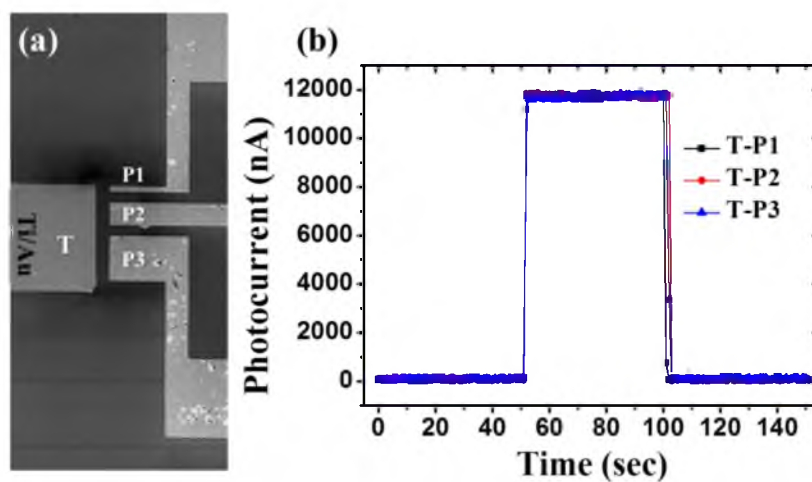

Figure 2.22 A four-terminal device with photocurrent measurement. (a) SEM image of the photodetector with 1 Ti lead and 3 Pd leads. (b) Photocurrent vs. time curve under 450nm laser at 114 mW.

CHAPTER 3

TUNABLE PHOTORESPONSE OF EPITAXIAL GRAPHENE ON SIC

Despite our initial success of acquiring a strong photocurrent signal from graphite/MLG devices as discussed in Chapter 2, the use of exfoliated HOPG samples has several limitations. First, the graphite/MLG flakes and mesas usually contain carbon layers of different thicknesses, and the influence of the thickness (number of layers) of graphene to the photoinduced current remains unclear. Second, the PTE effects are related to interface junctions between two adjacent graphene terrains[44] and the complex graphene topography contained in a graphite/MLG flake or mesa will lead to intricate effects that affect the device photoresponse. Third, the spot size of the laser is too big, covering the whole device area so that we cannot separate signal contribution from different lead/graphene junctions or device regions. Therefore, large-area EG based devices with uniform graphene layers are chosen for further study. The semi-insulating and thermal conducting SiC substrate will help conduct excessive heat from EG to minimize the photocurrent contribution from hot carriers by the thermal gradient.

In this chapter, we report photoresponse measurements from two comparable epitaxial graphene (EG) devices of different thicknesses (2-layer vs. ~10-layer EG) made on SiC substrates.[81] An asymmetric metal contact scheme was used in a planar

configuration to form a Ti/EG/Pd junction. By moving the laser illumination across the junction, we observed an increased photocurrent signal resulting from local enhancement of the electric field near the metal/EG contact. A maximum photoresponsivity of 1.11 mA/W without bias was achieved at the Pd/EG contact in the 10-layer EG device. Photocurrent was also observed under AM 1.5 illumination. Our experiments demonstrate the high tunability of this EG photodetector by varying EG thickness, metal leads, channel length, and/or illumination area. The fast extraction of photogenerated carriers was also verified through the chopped laser experiment on both EG and SiC devices.

3.1 Characterization of EG

As mentioned in Chapter 1, we obtained EG samples made on carbon face 4-H SiC with different layers of thickness, which were fabricated by our collaborators at the Institute of Physics (IOP), Chinese Academy of Science. Before employing the IOP EG samples, we also bought two EG samples from Graphene Works Inc. (Here we call them GW samples) to see which one has the best quality of EG for our device build-up. The GW EG samples were grown on the carbon face on the 4-H SiC substrate as well. The surface characterization of two kinds of EG samples provided the evidence that the EG samples from IOP give better surface quality in smoothness.

Two types of GW EG samples were purchased based on the different thickness of EG (2-layer and 30-layer), which was confirmed by the ellipsometry measuremnt. From Fig. 3.1, we can clearly see that the surface of 30-layer EG contains many hole defects, of which the depth is ~15nm. The 2-layer EG sample was also studied by SEM as well as

AFM (see Fig. 3.2). The surface quality is better than the 30-layer EG, and the layered structure was revealed by the color contract in Fig. 3.2a.

By using the same method for surface study, two IOP EG samples of 2-layer and ~10-layer were also investigated using SEM and AFM. As shown in Fig. 3.3a, 4 EG on SiC samples with the area of 2 mm x 10 mm were placed on a glass wafer. Fig. 3.3c shows the smooth surface under SEM. A typical AFM scan of a 10-layer EG film is also shown (Fig. 3.3b), which has a local roughness of ~0.3 nm within a 500nm domain (Fig. 3.3d). The two film thicknesses were verified by Raman spectra as shown in Fig. 3.4.

Compared with the GW samples, IOP samples have better surface quality as well as a relatively larger average domain size. Thus, the density of EG boundaries in IOP samples is smaller than that of the GW samples. The existence of grain boundaries in EG is known to affect the carrier mobility,[82] yielding lower device quantum efficiency. Thus, we pick IOP samples for the fabrication of our photodetectors. We note that in spite of the effect of grain boundaries, the overall photocurrent in our device was dominated by its large active area.

3.2 Epitaxial Graphene-Based Photodetectors

We used the IOP EG samples of 2-layer and 10-layer graphene to fabricate the large-scale photodetection devices by deposition of Ti and Pd metal contacts. This asymmetric metal scheme was applied to research the influence from different metals to the photoresponse. In addition, the thickness dependence and the laser position dependence were studied as well. The efficiency of carrier extraction from EG was compared with the related performance from the semiconductor SiC without EG through a chopped laser system.

3.2.1 EG Photodetector Fabrication and Measurement Preparation

Large-scale photodetectors were fabricated without involving any microscale fabrication technology. Fig. 3.5 shows the optical images and the schematic drawing of the device configuration. Two metal electrodes (2 x 3.8 mm) were directly deposited onto a continuous EG film with a 2.4 mm wide separation. A metal shadow mask was used to directly pattern electrodes in a Denton SJ20C electron beam evaporation system. 5 nm thick Ti and Pd were deposited on two ends and subsequently covered by a protective 20 nm thick Au layer to prevent oxidation.

Photocurrent for both 2- and 10-layer EG devices was measured at ambient conditions. A 450-nm continuous wave laser system with adjustable power output and a visible light source from an AM 1.5 solar simulator were used as illumination sources. The energy of the laser (2.75 eV, blue) was chosen to be below the band gap of the 4H SiC substrate (3.23 eV) to minimize the substrate contribution. The laser beam was directed onto the sample surface with a 100 μm diameter optical fiber while photocurrent measurement was performed by a Keithley 2420 I-V unit. As a control experiment, we also made a benchmark device by depositing metal contacts directly onto SiC substrate without EG; no significant photoresponse signal is detected from such device (see Fig. 3.6). It is shown in Fig. 3.6b that the blue laser illumination on the SiC detector induces many fewer electrons than on the EG device. Thus, the contribution of photocurrent from the bottom SiC substrate can be neglected for this laser system.

Because the contact metal layer is very thin, the laser beam is able to penetrate and reach the EG film, which adsorbs the most lights. The work function difference at the

metal/EG interface forms an internal electric field, which leads to the generation and drift of free electrons upon photoexcitation. The electric field drives the electrons from the high work function material to the low work function material. It is observed that when the laser or light is illuminated on either the Ti or Pd side, photoelectrons always flow from the metal lead to the EG. This indicates that EG has a work function lower than both Ti (Φ~4.3eV) and Pd (Φ~5.4eV) in the range of ~4.0 eV (see Fig. 3.7).

3.2.2 EG Photodetector: Position Dependence

To investigate the location dependence of photocurrent generation, a laser was scanned from the Ti side to the Pd side along the 2- and 10-layer EG devices. As shown in Fig. 3.8, the photocurrent signal is very strong when the laser illuminates directly on the metal contact. When the laser illuminates on the pure EG surface in between the two contacts, there is no electric field driving the photocurrent flow, and the signal is negligible. It is interesting to see that when the laser illuminates at or near both the Ti/EG and Pd/EG contact boundaries, there is a local signal enhancement (a peak in the photocurrent curve). This can be explained by the local electrical field enhancement at the metal/EG boundary: in addition to the vertical field across the planar metal/EG interface, there exists also a lateral field across the line boundary.[43] Overall, the thicker EG generates more photocurrent because of its higher light absorption compared to the thin EG.

3.2.3 EG Photodetector: Power and Layer Thickness Dependence

To investigate the relationship between the photogenerated current and light intensity, the I-V curves under different laser power illuminations were measured. A bias voltage in the range of +/- 1 mV was applied between the source and drain contacts. Fig. 3.9 shows the typical I-V curves of the thin 2-layer EG device illuminated by five different laser powers (0, 89, 201, 293, and 374 mW) on the side of Pd electrode. The linear I-V curve shifts upward with the increasing incident light intensity. The interceptions on the y-axis, i.e., the zero-bias photocurrents, illustrate that the amount of charge carrier generated by the laser illumination increases monotonically with the increasing laser power.

To quantify the relationship between the photogenerated current and light intensity, in Fig. 3.10 we plot the photocurrent, as extracted from Fig. 3.9, as a function of laser power. We see that the photocurrent generated at the Pd/EG junction with light illumination at both thin and thick EG samples (see Fig. 3.10) increases linearly with the laser power up to the highest laser power used. A linear fitting to the photocurrent data in Fig. 3.10 gives a constant photoresponsivity of EG on SiC over a wide range of laser power. The maximum photoresponsivities without bias measured on the side of the the Pd/EG junction for the thick and thin EG devices are 1.11 and 0.88 mA/W, respectively.

The linear photoresponse to the laser power observed in our EG devices is quite different from the behavior of photoresponse measured from the devices made from the micron-size graphene flakes, whose photocurrent displays a saturation when the incident laser power is too high[35] (see Fig. 2.15). We attribute this distinct advantage of our EG devices having a wide range of liner photoresponse without saturation to their long

channel length. The eliminated thermal effects, which are led by the thermally conducting substrate and possible long device channel, might have also helped to achieve the linear I-P behavior. Furthermore, our thick 10-layer device generates higher photocurrent than the thin 2-layer device, affording the opportunity to tune the device performance by varying the EG layer thickness in addition to varying device size (channel length and illumination area).

3.2.4 EG Photodetector: Lead/EG Junction Dependence

To reveal the effect of the different lead/EG junctions (Ti/EG and Pd/EG), photocurrent collected on the thin EG device at both the Ti and Pd leads is displaced in Fig. 3.11, as a function of laser power. The linear relationship of photocurrent vs. power curve is found at both the Ti and Pd lead junction. Also, a larger photocurrent is generated at the side of the Pd/EG junction than at the side of the Ti/EG junction, as shown in Fig. 3.11. We think this is caused by the larger work function difference between Pd and EG than that between the Ti and EG difference, which leads to a larger internal field at the Pd/EG junction (or larger band bending of EG as shown in Fig. 3.7).

The photoresponsivity at 0V bias measured on the thin EG device for the Ti/EG junctions is 0.12 mA/W, much lower than the photoresponsivity from the Pd/EG junction (0.88 mA/W). Furthermore, the linear I-P relationship was also observed, which means that the internal electric field at metal/EG junctions is dominating the generation and drift of electrons while the PTE effects were limited.

3.2.5 EG Photodetector: Photoinduced Conductivity Change

Illuminating on the Pd/EG junction, we also performed experiments using a much larger range of bias voltage up to 100 mV to measure the photoconductivity of the EG devices. Fig. 3.12a shows the results obtained from the thin EG sample. With or without light illumination, the device I-V curves shows different characteristics, indicating a slight change of the photoinduced conductivity from 0.187 to 0.192 Ω^{-1}. Fig. 3.12b shows the I-V curve with the laser on and off from the thick EG sample, which indicates the photoinduced conductivity change from 0.160 to 0.150 Ω^{-1}.

Fig. 3.13 shows the photoresponsivity as a function of bias voltage. The photoresponsivity increases initially linearly with the bias and then saturates, in agreement with the previous measurement. A maximum photoresponsivity of ~4.5 mA/W was achieved at ~0.7 V bias.

3.2.6 EG Photodetector: Sunlight Detection

The large photoresponsivity of our large-area EG devices of ~1mA/W indicates that a detectable signal should be obtained from the ambient light illumination without using a laser source. To confirm this, we used a solar simulator with AM 1.5 visible light and a power density of ~100 mW/cm^2, which was much smaller than the laser source (190,000 mW/cm^2 for 0.5mm spot size at maximum laser power). Fig. 3.14a shows the test result, which confirms the observable photoresponse to the AM 1.5 light. The zero-bias photoresponsivity is 4.08 mA/W at the active absorption area (2 x 3.8 mm) of the Pd/EG junction, which is significantly higher compared with our laser test at zero bias. We believe this is mainly because photons of a wide range of wavelengths, instead of a single wavelength, are adsorbed. Also, a larger photocurrent signal is observed on the Pd/EG

junction than the Ti/EG junction, in agreement with the laser testing results. Furthermore, to see whether the SiC substrate affects our AM 1.5 measurement on the EG device, we put our Ti/SiC/Pd device under AM 1.5 solar simulator as well for testing. The result shown in Fig. 3.14b indicates a very small photocurrent of ~65nA, which is several orders of magnitude smaller than the signal obtained in EG device (see Fig. 3.14a). The observable photocurrent in the SiC device is possibly due to the alloying between the metal (Pd) and the SiC at their interface to increase light absorption. Also, there can be some limited light adsorption above this SiC band gap (3.23 eV).

3.2.7 Carrier Mobility: SiC vs. EG

SiC and EG devices were built together with the same lead geometry and thickness (see Fig. 3.6a), so their photonic performances could be compared as seen in Fig. 3.6b. Here we report the photoinduced carriers shifting on the Ti/SiC/Pd device, captured by a source measurement unit with a chopped laser of tunable frequency. We can clearly see from Fig. 3.15 that more photocurrent was generated at the Pd/SiC junction rather than the Ti/SiC junction, which agrees with the result shown in Fig. 3.14a. In addition, the I-V curve fluctuates at a large range when the frequency of the chopped laser is low. That means the photogenerated carriers do not respond quickly enough in accordance with the low on/off ratio observed. Because the carriers arrive at the lead for extraction mix with background noise, the Keithley meter cannot collect the right current signal, separating the photocurrent from noise. When the frequency of chopping is higher (e.g., 187 Hz, in Fig. 3.15), the I-V curve looks more linear with less fluctuation.

For comparison, the Ti/EG/Pd device was also employed for testing under a laser frequency of 77Hz with a laser power of 201 mW. Fig. 3.16 indicates that the chopped

laser signal has no impact on the data collection by the Keithley meter, which proves that EG has high carrier mobility. Thus, the extraction of photogenerated carriers is fast enough to be recorded.

In conclusion, we report on a very simple and direct methodology to fabricate EG photodetectors in an asymmetric metal contact configuration. Photocurrent was first observed by using a continuous-wave blue laser. The dependence of photocurrent on the laser-spot position was measured, with the increased photocurrent signal observed near the metal/EG contact resulting from local enhancement of the electric field. A maximum photoresponsivity of 1.11 mA/W without bias was achieved at the Pd/EG contact in the 10-layer EG device. Photocurrent was also observed under an AM 1.5 illumination using a solar simulator, indicating potential practical application of the EG for photodetecting devices. In the end, faster extraction of photoinduced carriers was demonstrated in EG devices compared to a SiC detector.

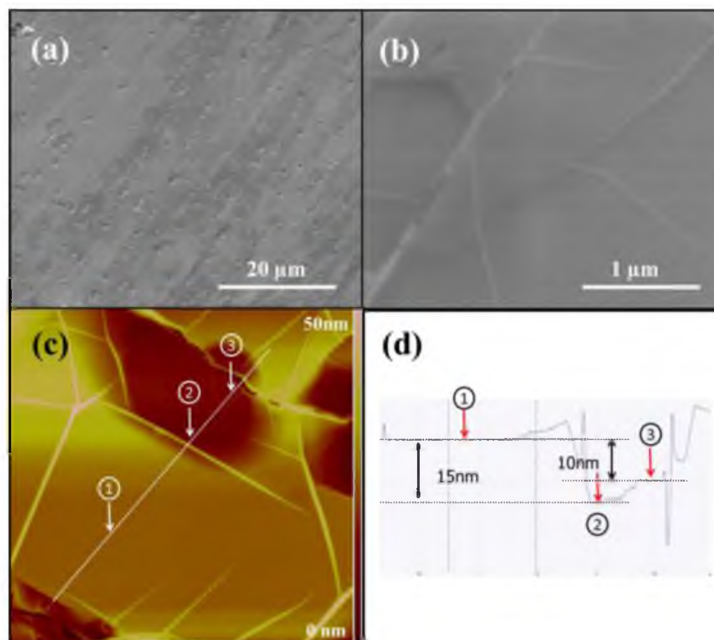

Figure 3.1 Surface characterization of 30-layer GW EG sample. (a) and (b) SEM image of EG surface with detects. (c) AFM scan of a 3µm x 3µm domain on EG surface. (d) Depth profile along the dotted line shown in (c).

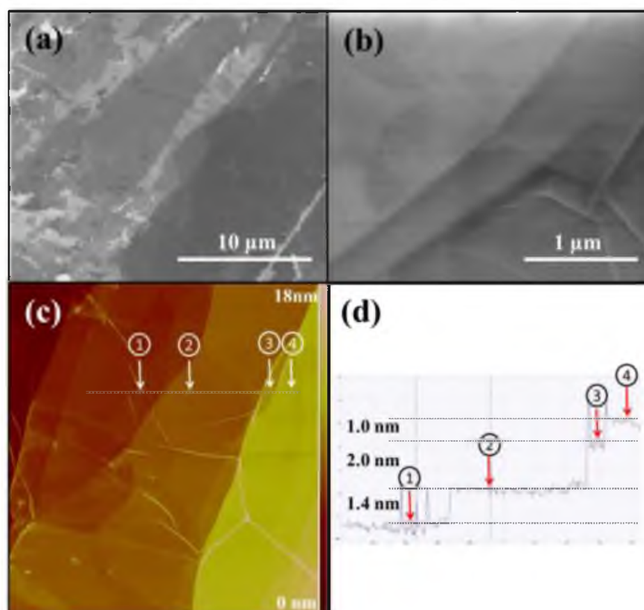

Figure 3.2 Surface characterization of 2-layer GW EG sample. (a) and (b) SEM image of EG surface with detects. (c) AFM scan of a 3µm x 3µm domain on EG surface. (d) Depth profile along the dotted line shown in (c).

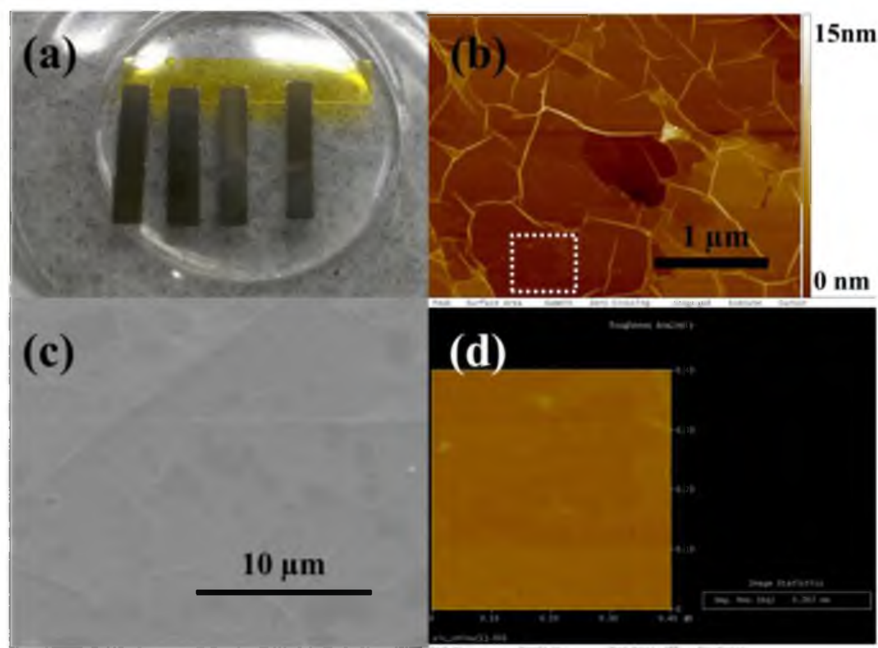

Figure 3.3 Quality analysis of EG samples from IOP. (a) Image of 4 EG samples. (b) AFM scan of 10-layer (thick) EG surface with a ~3x3µm domain. (c) SEM image of thick EG surface. (d) Roughness analysis of the dotted box confined surface area in (b), which gives a statistic roughness of ~0.26nm.

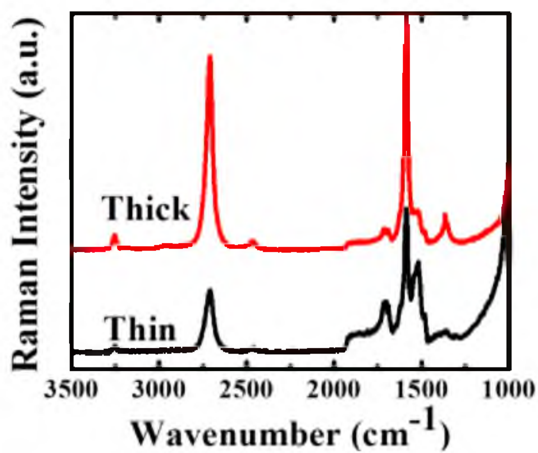

Figure 3.4 Raman spectra of thin (~2-layer) and thick (~10-layer) EG films to analyze the number of layers on C-face SiC

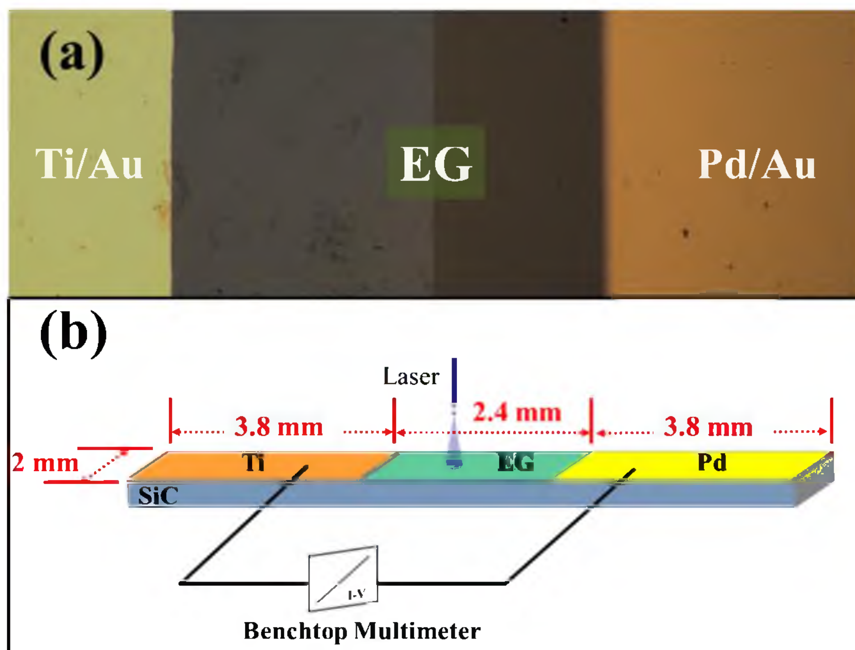

Figure 3.5 (a) Optical image of the EG based device with Ti and Pd contacts, covered with Au. (b) Schematics of the device with asymmetric Ti and Pd lead contacts. A Keithley meter was used for I-V characterization.

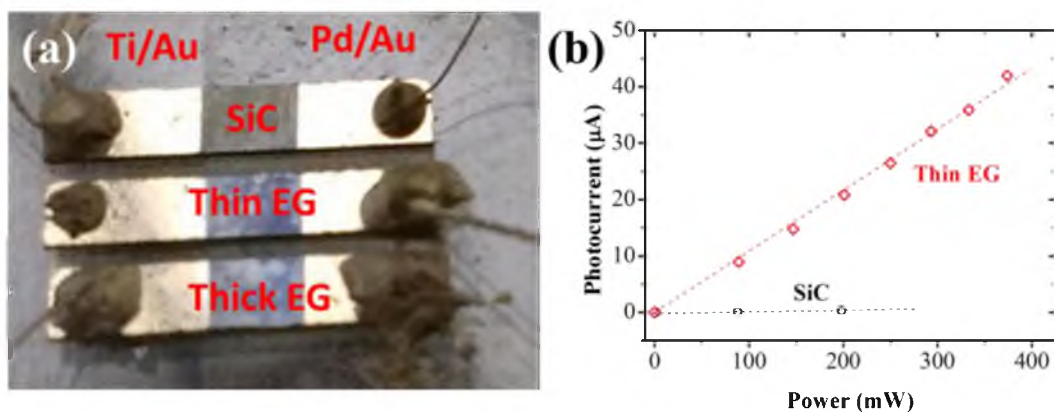

Figure 3.6(a) Thick, thin and SiC device fabricated with same dimensions and placed parallel on glass substrate for test. Silver paste was used for the connection between copper wires and electrodes; (b) Photocurrent of SiC and thin EG device from the Ti/EG junction as a function of laser power.

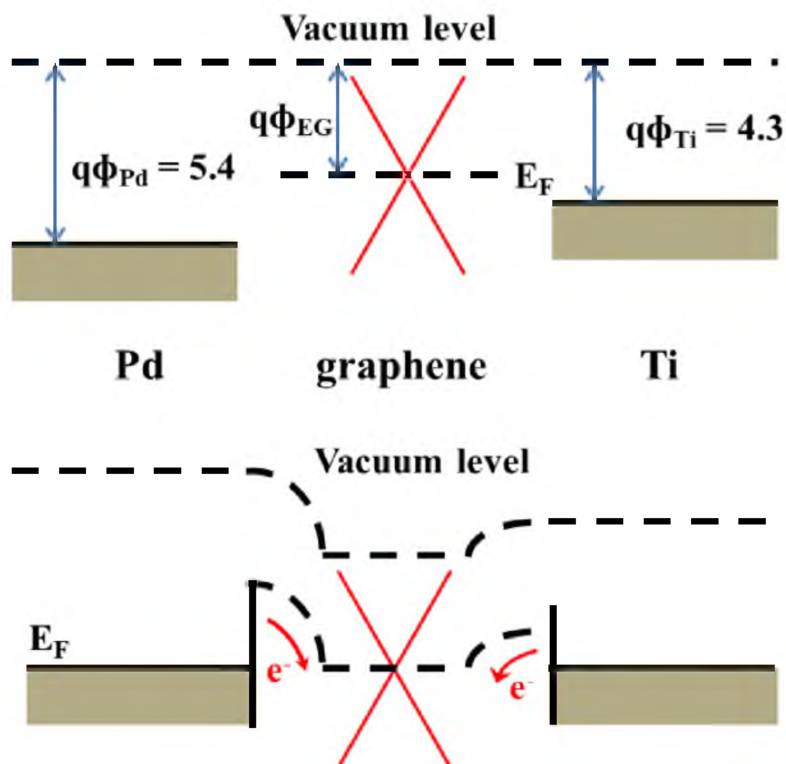

Figure 3.7 Energy band diagram showing the internal electrical field at the metal/EG contacts. Upper panel: Bands of isolated metal leads and EG. Lower panel: Bands of contacted metal leads and EG in thermal equilibrium.

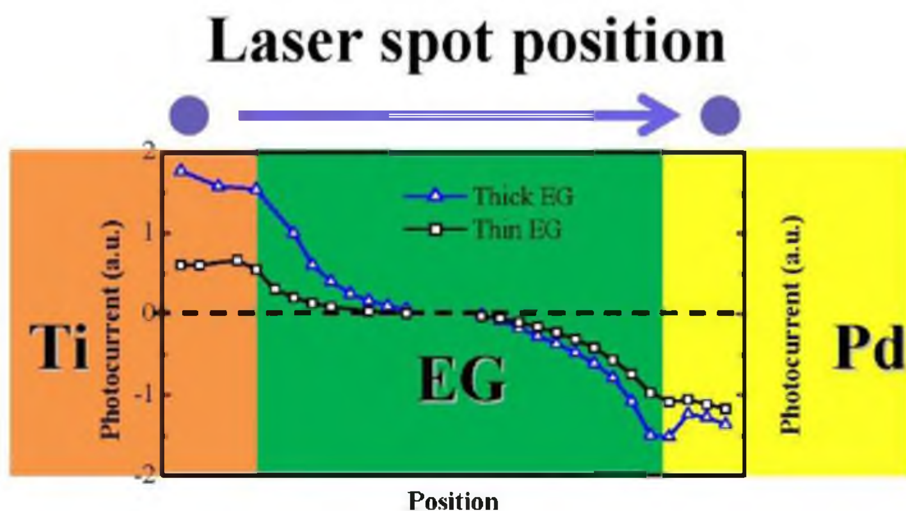

Figure 3.8 Photocurrent (arbitrary unit) of the thin and thick Ti/EG/Pd devices in response to laser illumination at different locations.

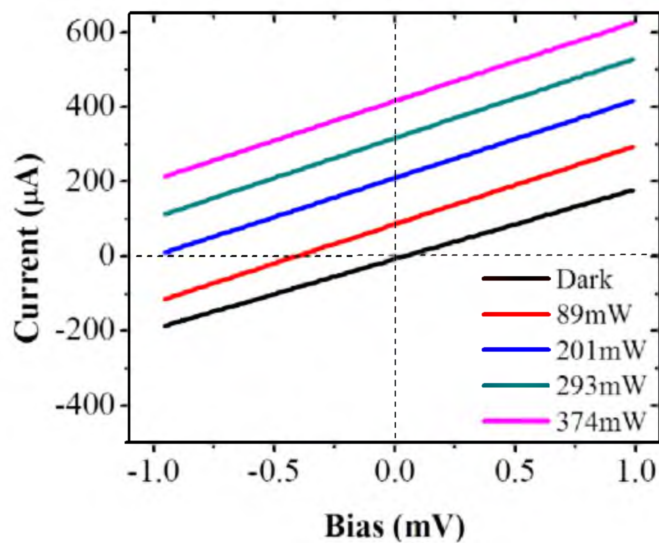

Figure 3.9 I-V curves of thick EG device under different laser illumination power. Laser spot was located on the Pd/EG junction.

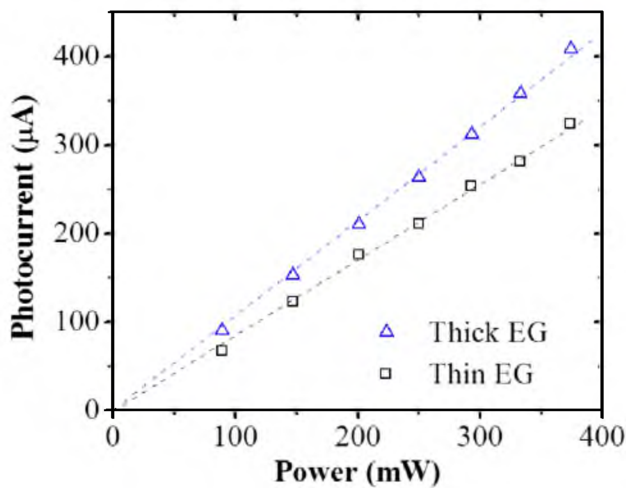

Figure 3.10 Photocurrent measured as a function of laser power at the Pd/EG junction from both the thin and thick EG devices.

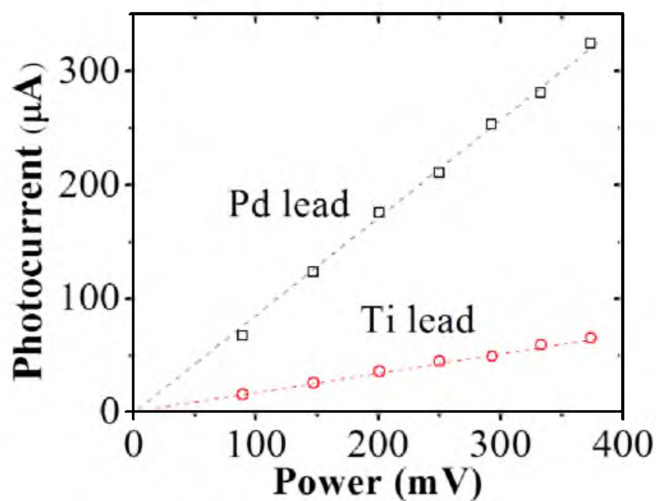

Figure 3.11 Photocurrent measured from the thin EG device at the Pd/EG vs. Ti/EG junction.

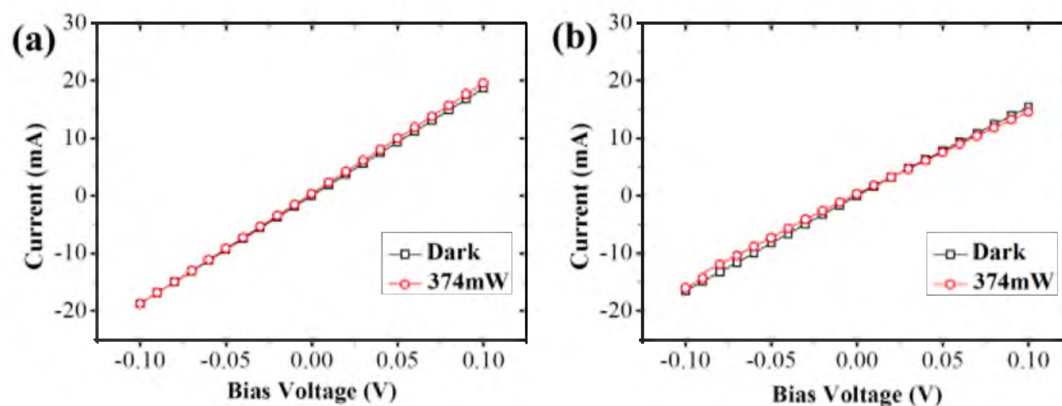

Figure 3.12 Current (I) as a function of source–drain bias (V) with and without light illumination at 450nm wavelength at Pd/EG junction, (a) for thin EG device and (b) for thick EG device.

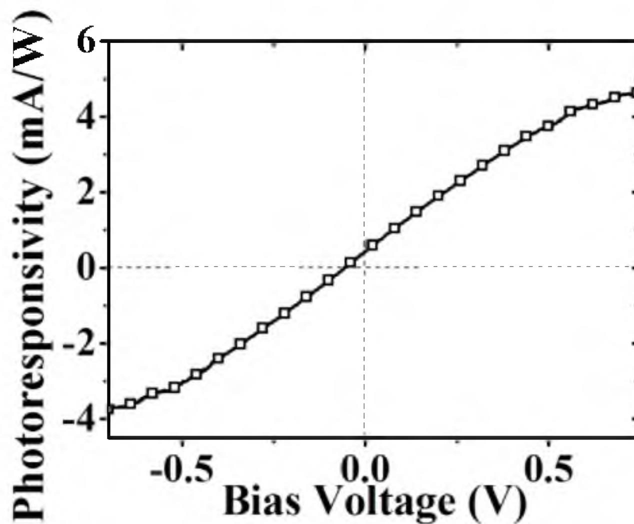

Figure 3.13 Measured external photoresponsivity (PR) as a function of the bias voltage.

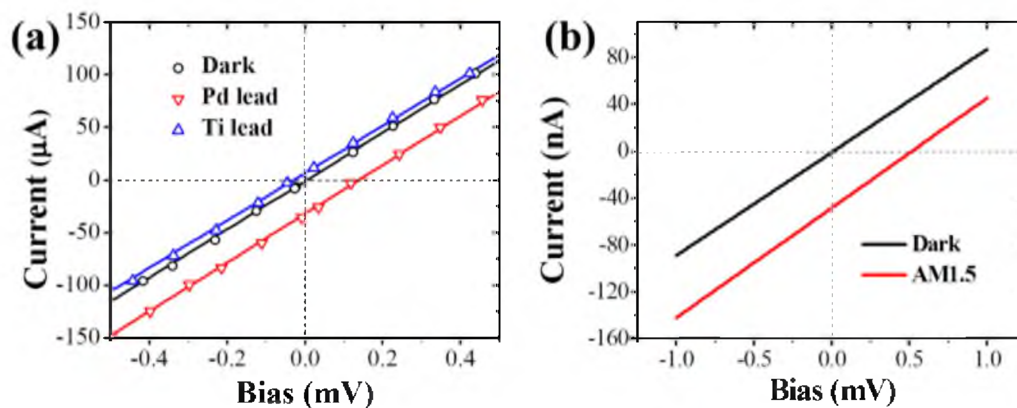

Figure 3.14 AM 1.5 characterizations. (a) I-V curves of thick EG device under AM 1.5 illumination. The down triangle and up triangle represent the light irradiated on the Pd lead and Ti lead, respectively, while the circle data show the I-V characteristics in the Dark environment; (b) SiC device test under +/- 1mV bias with or without light illumination.

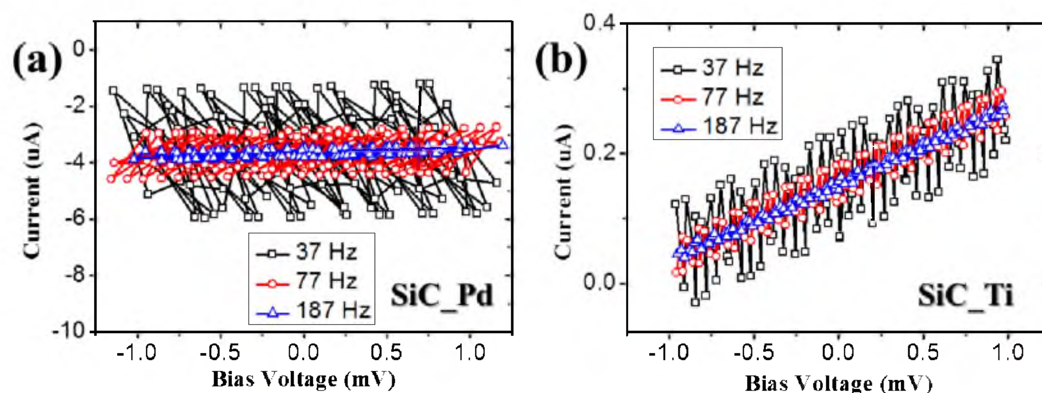

Figure 3.15 I-V characteristics of Ti/SiC/Pd device under chopped laser illumination with 37 Hz, 77 Hz, and 187 Hz, (a) near Pd lead; (b) near Ti lead.

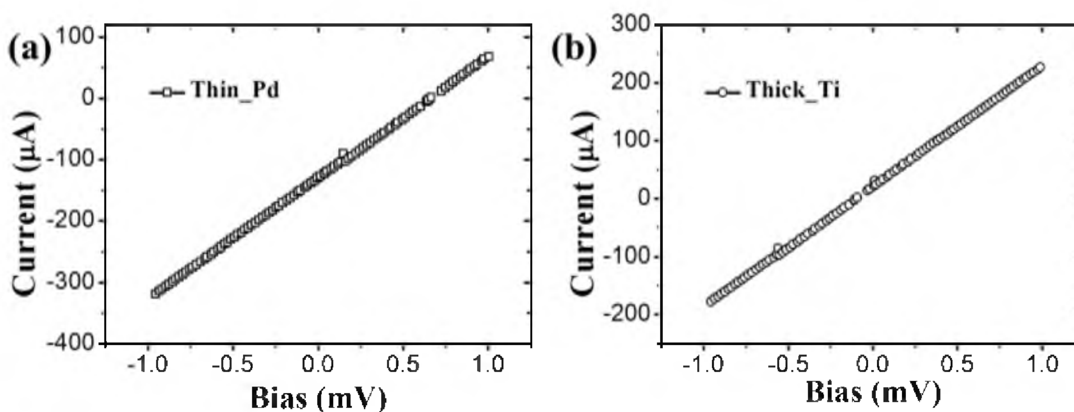

Figure 3.16 Photoresponse of the Ti/EG/Pd device under the blue laser of 450nm with a chopped frequency of 77Hz. (a) I-V curve at Pd/EG junction for the thin EG device. (b) I-V curve at Ti/EG junction for the thick EG device.

CHAPTER 4

PHOTORESPONSE IN CNR-BASED DEVICES

When the 2D graphene is cut into 1D gaphene nanoribbons (GNRs), which form confined quantum states, a gap is opened with the size inversely proportional to the width of the GNR.[61, 62, 83] GNRs have been successfully synthesized by chemical derivation,[62] unzipping of carbon nanotubes,[84] scanning tunneling microscope (STM) lithography,[85] nanoimprinting lithography,[86] and controlled growth on SiC.[87] These methods have the drawbacks of rough edges, slow processing, or a limited patterning area. Thus, there is increasingly a need to utilize some existing techniques for fabricating large-scale and small-width GNRs or more generally CNRs consisting of multiple layers of GNRs.

In this chapter, we present the experimental details to achieve fabricating CNRs as well as the results of photoresponse measurement of CNR-based photodetectors. This is one of the milestones that has to be achieved before realizing our future CNR photovoltaic cells. Two state-of-the-art techniques, e-beam lithography (EBL) and focused ion beam (FIB), were utilized for the fabrication of CNRs. The CNR-based devices, consisting of multilayer graphene ribbons in the width range of ~300nm down to 20nm, were tested for photoinduced current. Compared with graphite/MLG-based photodetectors, these CNRs based devices are seen to produce larger photocurrent due to the improved photoresponsivity.

4.1 CNR Fabrication by EBL

In this section, we describe the fabrication of EBL-defined CNRs, which begins with the graphite films as well as the optical lithographically defined graphite mesa on SiO_2/Si substrate. The tuning of e-beam parameters can lead to different results in ribbon cutting. By optimizing the parameters, we have succeeded to make CNRs down to ~35 nm.

4.1.1 Approach for CNRs Fabrication

Taking advantage of the capability of the e-beam lithography equipment at the University of Utah, we have two different approaches to pattern the GNRs: positive lithography and negative lithography. Correspondingly, two positive and negative photoresists or e-beam resists need to be used for the two different methods. Typically, PMMA, ZEP520 (1:1 co-polymer α-chloromethacrylate, α-methylstyrene) or SML can be used for the positive process with high resolution, while the NEB-31A is usually used for the negative process. The working principles of the EBL photoresist process are introduced in Chapter 2, Section 2.2.3. It is interesting to mention that the exposed area of negative resist film by the e-beam will become insoluble to the developer (see Fig. 4.1, step 3 for the positive development for contrast), while the unexposed part will be dissolved in certain solvents. This is directly contrary to the positive EBL process using PMMA.

Fig. 4.1 shows a typical positive EBL process flow for our CNR fabrication. A negative EBL process would differ from step 3 to step 6 in Fig 4.1. Using positive or negative EBL, CNRs are formed beneath the undissolved photoresist after developing and anisotropic plasma etching. In the negative EBL process, one can directly control the ribbon width by controlling the e-beam spot size (or beam current) while in positive EBL,

CNRs are generated by the squeezing of two parallel e-beam scans (see Fig. 4.2 below). Comparing the two methods, positive EBL can always give a narrower ribbon because the ribbon size is controlled by the distance of two parallel e-beam scanning patterns (see Fig. 4.2). Thus, we chose positive EBL for the patterning of CNRs.

Fig. 4.2 describes the two different modes (positive and negative) to generate CNRs. The EBL functions can be realized in the e-beam machine, which is built directly inside the SEM machine. The resolution of an e-beam machine is mainly defined by the e-beam size, which is controlled by the beam current and acceleration voltage. A state-of-the-art e-beam lithography system such as the JEOL JBX-6300FS in the Center for Integrated Nanotechnologies in the Sandia National Lab, whose max acceleration is 100kV, can process a minimum beam spot of ~3 nm. With a normal e-beam lithography SEM, such as the FEI NovaNano in the University of Utah Dixon Laser Institute, which is the only accessible EBL machine on the campus, its maximum acceleration voltage for electrons is 30kV. Thus, a minimum spot of ~30 nm can be achieved while PMMA was used for the positive EBL processing of CNRs to obtain <50-nm ribbons.

The production of CNRs began with a graphitic mesa covered with a Si layer and the HOPG ribbons were finally achieved by O_2 RIE (see step 5 in Fig. 2.6). Like Photoresist s1813 for the optical lithography, e-beam resists are also reactive under O_2 plasma. Thus, a protective Si layer is also needed in e-beam lithography to prevent affecting the graphite structure underneath.

Based on our test, the etching rate of 950K PMMA (from Micro Chem Inc.) under SF_6 RIE is ~22 nm/min, which is close to the etch rate of PR s1813 and Si. As the silicon layer is much thinner than the spin coated PMMA film, PMMA serves as a masking layer

for Si. The patterned PMMA nanofeatures can then be transferred to the bottom Si film, and subsequently transferred to the HOPG/MLG film by anisotropic O_2 plasma etching. The etch rate of PMMA under O_2 plasma was studied, as shown in Fig. 4.3.

4.1.2 Parameters of EBL for CNR Cutting

The use of PMMA is one of the key steps in EBL and the parameters are listed below in Table 4.1. After the spin coating of PMMA, our sample was attached to a metal holder by a carbon tape to build a good electric connection with the ground. The purpose of this is to export redundant electrons remaining on the sample surface. These unwanted electrons may cause unsteadiness in the image and negatively affect the stability of our e-beam spot that hits the PMMA surface. Samples were placed horizontally, normal to the beam direction, and lifted to a certain distance from the electron gun. For the SEM in the Dixon Laser Institute, we put the sample at the optimal distance of 5 mm from e-gun. The SEM chamber was then pumped down to achieve high vacuum.

Prior to activating the e-beam, the SEM machine was set to 30 kV and a spot size of 1.0 (machine parameter with no units) in the lowest beam current range. The machine's highest possible acceleration voltage (30 kV) and lowest possible beam current provided the best beam resolution. We tested the beam under different acceleration voltages and discovered that the bond of PMMA does not break at or below 15 kV. A 20 kV beam is capable of exposing PMMA, but higher voltage always gives a smaller beam size. The actual beam current was measured by a Faraday Cup placed in the chamber. For FEI NovaNano SEM, the e-beam current was typically ~19 pA for a spot size of 1.

To get the smallest ribbon size, it was necessary to tune and optimize the e-beam to have the smallest spot size. This was mainly affected by two parameters in SEM: focus

and stigmation. Focusing on the sample surface can lead to a clear image based on electron scanning, and good focusing means the focal point of electron flow is located right on the surface of the detection area of samples. Generally, we obtain a good focus by tuning the electron beam on a testing area of the sample surface. By doing so, we avoid exposing the PMMA on the nearby patterning area. After obtaining a good e-beam focus on the testing area, we can easily maintain the same focus when the beam spot moves to the patterning area.

Stigmation controls the shape of the electron beam. The x and y axis of stigmation modulation changes the shape of the e-beam spot in the relevant direction. The ideal shape for an e-beam spot is round. This optimal shape confines electrons to the smallest area and offers the lowest spot width in both the x and y directions. In this experiment, the adjustment of stigmation was performed by tuning the image of the gold nanoparticles (see Fig. 4.4a) and subsequently tuning the beam to obtain the smallest spot on PMMA (see Fig. 4.4b).

In Fig. 4.4b, round spots in white are PMMA with bonds broken by e-beam exposure. Gray areas represent the unexposed PMMA. The Ti/Au lead below the PMMA layer acts as a high-contrast substrate so that the e-beam spot can be more clearly observed. The optimal e-beam spot of ~35nm is very close to the limit of the SEM machine. Moreover, the tuning of the e-beam spot mark on PMMA can be used as another way to obtain a good focus on the testing area.

The EBL pattern is predesigned using AutoCAD software (DesignExpress) to form a vector file in which a dashed and closed structure means filling inside with e-beam spots. A solid line represents the trace for e-beam writing (see Fig. 4.5). We applied the

methodology shown in Fig. 4.5a and used two parallel dashed rectangles to confine a ribbon in between. Fig. 4.5 is a schematic demonstrating how CNRs are produced using PMMA (positive EBL).

After tuning the e-beam, we ran a program called NPGS (Nanometer Pattern Generation System), which allows the e-beam machine to read the designed EBL pattern. In the NPGS software, several key parameters for EBL writing, including dose, beam center-to-center distance, beam line spacing, and pattern coordinates, were set before patterning/writing. Dose is the most important parameter. We tested 2 line doses: 0.05 nC/cm and 0.08 nC/cm, of which 0.05 nc/cm is slightly better based on our testing (see Fig. 4.6).

Center-to-center distance is usually set to be around half of the spot size, while line spacing should be slightly less than the e-beam spot size. These two parameters changed in every experiment according to the real spot size we tuned (see Fig. 4.4b) before EBL patterning. To precisely control the position of e-beam patterning, we put down alignment marks (Ti/Au leads) before the PMMA spin coating in order to use pattern coordinates in NPGS to load our EBL design to PA to start e-beam writing.

After the development shown in step 3 in Fig. 4.1, RIE was used to remove Si as well as unprotected graphite. The etching parameters are shown in Table 2.1 and Table 2.2. For the 50 nm thick Si protective layer, 2 minutes SF_6 etching is needed. The depth of HOPG etching is determined by the duration of exposure to O_2 plasma.

4.1.3 Characterization of EBL Defined CNRs

EBL defined CNRs were first achieved with widths of several hundreds of nanometers. Characterization was performed using SEM (see Fig. 4.7). The shifting of

the HOPG mesa in Fig. 4.7a may be caused by the spin coating process. The shear stress caused by spinning can lead to the drifting of the HOPG mesa because the interlayer interaction in a thick HOPG mesa (thick HOPG mesas drifted into two thinner mesas) is very weak. 200 nm wide ribbons were produced by the first attempt at EBL and the rough edges of the ribbons are shown in Fig. 4.7b. We found two reasons which may contribute to this: 1) the recipe we used for protective Si layer etching (see recipe 1 in Table 2.2) not only etched away the 100 nm thick Si layer but also partially etched the EBL patterned PMMA ribbons on top of the Si layer; 2) PMMA was not removed before the O_2 plasma etching of HOPG (step 4 in Fig. 4.1). Like PR s1813 used in optical lithography, we removed the photoresist to obtain a HOPG mesa with a clean edge with O_2 RIE. Thus, to reduce the edge roughness, we used a new recipe of SF_6 plasma shown in Table 2.2 and kept samples in acetone liquid for 1 hour before HOPG etching.

Through the adjustment of the parameters controlling the ribbon width in EBL, we fabricated CNRs with different sizes (see Fig. 4.8). The widths of CNRs achieved were as low as ~35nm while maintaining the length of ribbons in 20–40 μm. The aspect ratio of CNRs increases as we continued to narrow the CNRs.

In Fig. 4.8, all these CNRs were directly written on thick HOPG mesas; however, they were not etched through. So the CNRs were still electrically conductive via the HOPG substrate. Thus, we then implemented EBL on thin graphite/MLG mesas (see Fig. 2.21a and Fig. 4.9) to etch through the graphite/MLG and expose the SiO_2/Si substrate. After that, all the CNRs were isolated and disconnected electrically for further device fabrication and related testing. Fig. 4.9 shows the optical images of thin HOPG mesas covered with a 50 nm thick Si protective layer as well as the EBL patterned ribbons. The

thickness of HOPG is thinned down ranging from 80–30 nm so that a short O_2 plasma etching was enough to expose the bottom SiO_2/Si substrate between CNRs (see Fig. 4.9c).

SEM characterization in Fig. 4.10 further confirms the successful etching of CNRs. Graphite particles were left in between CNRs when the O_2 Plasma etching was not long enough to remove them. A further etching of carbon was completed while Si was still covering CNRs, which exposed the SiO_2 substrate (see Fig. 4.10b).

In addition, widths and thicknesses of CNRs were also characterized by AFM, which displayed the roughness of CNRs after a complicated process shown in Fig. 4.1.

Fig. 4.11a provides the result from step 5 in Fig. 4.1, while Fig. 4.11b shows the real images of step 6 in Fig. 4.1. From these images, it is observed that the final etching step to remove Si causes the surface roughness of CNRs as well as the roughness of the SiO_2 substrate (see Fig. 4.11b, right). This indicates that the SiO_2 substrate is etched by SF6 plasma.

In summary, through the EBL patterning, we have successfully fabricated CNRs with a high aspect ratio and obtained different CNR arrays in the width range of 300 nm down to 35 nm. Some selected etched-through graphite nanoribbons by the EBL patterning are shown in Fig. 4.12. However, EBL-defined CNRs have limited ribbon edge/surface quality especially when the size of ribbons was narrowed down to less than 100 nm. This is due to the complicated processes involved in the patterning process. In addition, the ribbon width is limited by the e-beam resist (PMMA) and the SEM beam size and is difficult to be further narrowed down. Hence, we will introduce a method to simply and directly pattern CNRs with even smaller width in the next section.

4.2 MLG/EG Nanoribbon Fabrication by FIB

In this section, we present our work of using focus ion beam (FIB) to fabricate large-array, high-quality CNRs down to ~15 nm. The focused Ga^+ ion beam is used as a source for direct writing on both HOPG and EG films. Recipes and protocols for FIB nanopatterning of CNRs are developed.

4.2.1 Introduction to FIB

FIB is one of the state-of-the-art technologies used to create features with a high aspect ratio on a solid surface. Nanometer size features can be created on a sample surface, resulting from the collision between ions and surface atoms on a solid surface. A high vacuum in the $1x10^{-6}$ torr range in the FIB chamber is required to avoid interaction of ions with gas molecules and to increase the mean free path of ejected ions. Liquid metals are used as ion sources, of which Ga is selected due to its low melting temperature (29.8 ℃), low surface free energy, and high purity used in a high vacuum.

The FIB machine used in our research is a Helios NanoLab 650 DualBeam from the FEI Company. Fig. 4.13 shows the schematic drawing of the chamber in the FIB system as well as the material removal process in FIB. As Ga ions bombard a solid surface on the sample, elastic/inelastic collisions occur, and surface atoms are ejected by overcoming the surface binding energy. The structures engraved by the ion beam will appear on the sample surface with desired designs.

The FIB machine of the Helios NanoLab 650 DualBeam has both electron scanning microscopy and ion beam scanning microscopy as well. The FIB detector in Fig. 4.13 collects secondary electrons which are collected by a detector and provide an image from

the ion beam scanning. Fig. 4.14 shows a typical Ga ion bombarding a sample surface and producing sputtered materials and secondary electrons by collisions.

Typically, we use 30 kV for the acceleration voltage of Ga ions. The current of beam, which is actually the amount of ions delivered per unit time, is set to be on the order of picoAmps (pA). This provides a slow material removal rate and sharp imaging. We noticed that the preset beam current may be smaller than the actual current. This is because apertures defining the beam current can be etched by the ion beam. Ion beam dose is also a key parameter for FIB patterning, which is the number of ions impacted and absorbed into the target through a defined area. Changing the dose of the ion beam directly affects pattern qualities.

With the FIB machine on campus, we can also have e-beam or ion-beam-induced deposition of some metals. Metals can be deposited according to designed patterns defined by the e-beam or ion-beam, which can be nanometer size. Plantinum was used in our research to be deposited on our sample surface for electrodes.

4.2.2 FIB Patterning and Characterization of CNRs

Various factors influence the patterning on HOPG and EG films when FIB is used. We have tested the effects of many factors and finally achieved high quality CNRs with desirable dimensions.

The process of the FIB patterning is shown in Fig. 4.15. Ga ion spots illuminate the sample surface, filling in the dashed box and removing the material in that box (see Fig. 4.15). A CNR is then defined by two adjacent boxes so that the width of the ribbon can be smaller than the size of the ion spot. In Fig. 4.15, a pitch with dimension a and b in the FIB patterning is shown (the pitch size is defined as $a + b$). This is used for the software

design of FIB patterns and is critical to the CNR fabrication. *a* represents the size of the desired etched box while *b* shows the preset ribbons size by FIB machine software. The actual size of *a* and *b* may change after FIB patterning; we will later discuss the effect of pitch in details. If the function of ion-beam deposition is turned on, the dashed box in Fig. 4.15, which is full of ion spots with metal species, will be filled with the metal material, i.e., Pt.

Like e-beam lithography, good beam stigmation and good focus on the sample surface are required prior to FIB patterning. We first tried FIB patterning on HOPG flakes on SiO_2/Si and obtained HOPG CNRs with very good quality (see Fig. 4.16). Fig. 4.16a shows FIB patterning of HOPG film on SiO_2/Si substrate with different etching duration, and SiO_2 nanoribbons were also fabricated. Uniform and clean CNRs in the width range of 40 nm to 200 nm are shown in Fig. 4.16b–d.

AFM scanning on the FIB patterned HOPG CNRs on the SiO_2/Si substrate is shown in Fig. 4.17. The Ga ion beam is able to etch away HOPG as well as other removable materials, like SiO_2. The etch rates are different for different materials. The dashed line with the arrow in Fig. 4.17 (right panel) indicates a linear depth change was achieved with different doses in use for both SiO_2 and HOPG. The etch rate based on the depth change in Fig. 4.17 is shown in Fig. 4.18. The tested etch rate of HOPG (0.107 $nm*\mu m^2/pC$) is useful for our future FIB patterning on different thicknesses of graphite/graphene film with a proper ion beam dose.

Because of the terrains of different thicknesses in a HOPG/MLG island or mesa, the FIB patterning was sometimes either not etching through down to the substrate or overdosing the ion beam to cause rough CNRs edges. FIB patterning of CNRs usually

cannot achieve a large-area array of CNRs because it is limited by the size of the starting island or mesa. Moreover, it is difficult to achieve narrow CNRs from HOPG islands or mesas because they are usually too thick and the desired aspect ratio of CNRs requires thinner film. Therefore, we decided to switch from HOPG film to EG film. FIB patterning of uniform and thin EG on C-face 4H IOP SiC was tested. It was found that thick EG (10-layer) can yield high quality ribbons (see Fig. 4.19a) by FIB patterning due to the relatively thicker carbon film and better surface quality while the thin EG (2-layer) film can yield narrower CNRs with less good quality.

We first optimized the FIB patterning process by tuning the machine settings: beam current, dwell time, center-to-center distance, number of passes, and ion dose. Beam current of the FIB was set in the range of 17 pA to 24 pA. Higher beam current may result in the increased a parameter in Fig. 4.15. This leads to overexposure, causing the graphene ribbons to disappear as the FIB overetches the area. Dwell time (defined as the time the ion beam stays on a single site on the sample surface) was set to be 1 μs. The center-to-center distance of ion spots is one of the critical factors for fabricating nanometer size nanribbons with clean edges. This size was adjusted to the lowest limit of the machine, 1.02 nm, to achieve the most dense ion beam spot array. The resulting ribbons showed very good quality. The quantity of passes, i.e., the number of ion beam scans, is critical as well. According to our test, 3 passes usually provided the best nanoribbons (see Fig. 4.20). In addition, we investigated the influence of the ion beam. Different doses were applied in the FIB patterning on the 10-layer EG sample with 3 passes of ion beam scanning to etch through EG down to the SiC substrate.

As shown in Fig. 4.21, both insufficient and excessive doses limit the quality of graphene nanoribbons. Among the dose settings shown in Fig. 4.21, the dose of 22.20 pC/μm^2 provided the best quality graphene ribbons yielding a width of 30 nm. According to Fig. 4.15, the pitch size of FIB patterning is critical to our results. Thus, different combinations of sizes for *a* and *b* in our pattern design may lead to different nanoribbons, as shown in Fig. 4.22. To summarize, pitch sizes in the range of 110 nm to 280 nm were used here. Narrow ribbons were obtained with the design of a low value of *b* (see Fig. 4.22e, Fig. 4.22f, and Fig. 4.22i). Proper pitch design can lead to clean edges of nanoribbons independent of the width of ribbons (see Fig. 4.22d); however, the ribbons with small width may have bad edge quality (see Fig. 4.22f and Fig. 4.22i).

In order to fabricate graphene naoribbons in a high-density array, the effect of pitch size for FIB patterning was further investigated. In Fig. 4.23, pitch design of 60/30 nm provided a near 30 nm wide graphene nanoribbon array with a clean edge while the design of 40/30 nm achieved 20 nm graphene nanoribbons with a rough edge. All other results showed worse ribbon quality even though narrower ribbons were fabricated.

Using the 10-layer EG film on SiC, we successfully patterned 20 nm ribbons by FIB in a dense, long, parallel array (see Fig. 4.24a and Fig. 4.24b). An FIB-patterned CNRs array was also achieved on 2-layer EG film with the ribbon width as low as 15 nm (see Fig. 4.24c and Fig. 4.24d). Although the lowest ribbon width (15 nm) was realized on thin EG film, small CNRs with good quality were only found in a certain area of the patterned array. To our knowledge, fabrication of a graphene nanoribbon array consisting of 400 ribbons with a ribbon width of $\leq$20 nm has not been reported before.

4.3 Photoresponse from CNR-Based Photodetectors

In this section, the background of photodetectors based on GNRs is introduced. Photodetectors fabricated using CNRs made by both EBL and FIB has been characterized and tested. The results showed great photoresponsivity.

4.3.1 Introduction to GNR-Based Photodetectors

Semiconducting GNR was proposed and analyzed for an effective phototransistor,[88, 89] which is sensitive in the far infrared range like narrow-gap semiconductors. Additional theoretical work further predicted the infrared optical response of a GNR based device.[90] It has been reported that GNR-based photodetectors showed much larger photoresponse in the infrared range, compared to reduced graphene oxide.[41] The enhanced photogenerated current was also observed resulting from the increased light absorption by multilayers of GNRs.[41]

Also, photodetectors based on GNR arrays were achieved and tested.[56] The intrinsic graphene plasmon excitation was proposed to explain the one order of magnitude enhancement compared with the traditional electron-hole pair excitation. The laser induced temperature rise for phonons or electrons leads to different effects of photoresponse: The elevated phonon temperature promotes the electron-phonon scattering, thus reducing the transport current[46–49]; however, a high electron temperature leads to hot carriers, which increase the photogenerated carrier conduction.[52, 56] Unlike plasmons in metals,[54] this intrinsic plasmonic effect shows longer carrier lifetime.

We believe that the intrinsic plasmon enhancement in GNRs will also apply to the devices based on CNRs. Moreover, the multiple graphene layers would benefit the

photocurrent signal by the enhancement of light absorption. Therefore, we have made some efforts to fabricate and test CNR photodetectors, as discussed below.

4.3.2 Photoresponse of EBL-Defined CNRs

After the fabrication of CNRs by EBL, asymmetric leads were laid down at each side of the ribbon array to form a source-drain connection. The techniques used for the deposition of metal leads as discussed before (see Section 2.2.3) and were used here again for the CNRs device fabrication. Fig. 4.25a shows one such CNR device, and Fig. 4.25b shows a similar device with the improved metal leads (Ti and Pd leads covered with Au) compared with Fig. 4.25a (pure Ti and Au lead), which enhance the adhesion of the lead to the substrate as well as preventing oxidation of Ti. However, both devices shown in Fig. 4.25 were not successful to carry out photoresponse measurement. Next, two more devices were made using CNRs of different ribbon width and successfully tested for the photoresponse measurement (see Fig. 4.26).

The thicknesses of the CNRs in both devices are around 30 nm, which is slightly thinner than the HOPG film devices (e.g., the device shown in Fig. 2.16 with a graphite film thickness of ~35 nm). The average channel lengths for the 270 nm and 120 nm CNR photodetectors are 9 μm and 3 μm, respectively. Counting the pitch size (1 μm) used for the CNR fabrication by EBL, the two devices were estimated to contain ~130 ribbons. However, most (75%) of the 120-nm CNRs were broken during the EBL process. Thus, the overall active areas for each device is 350 μm^2 (270-nm CNRs) and 11.7 μm^2 (120-nm CNRs), respectively. The 120-nm CNRs device has a much smaller active area for light absorption.

The experimental setup shown in Fig. 2.14 was again used for testing and a 488 nm continuous-wave laser with a spot size of 500 μm was utilized to spot the entire active area of a device. The performance of two devices in response to the laser illumination is shown in Fig. 4.27. When the power of the laser was set to be 1.3 mW, the photogenerated currents for the two devices were 80 nA (270-nm CNRs) and 25 nA (120-nm CNRs), respectively (see Fig. 4.27a and Fig. 4.27b). Considering the spot size of the laser beam as well as the active area of ribbons, the photoresponsivities of the two devices are 0.65 mA/W (270 nm) and 2.4 A/W (120 nm), respectively, both higher than our HOPG flake-based photodetector shown in Fig. 2.17.

Despite the larger area of the 270-nm CNRs device, the response of this photodetector is much smaller than the 120-nm CNRs device. The reason is not clear. We did notice the 120-nm ribbons have better edge quality than 270-nm ribbons (see Fig. 4.26a and Fig. 4.26b) so that there are less edge states in the 120-nm CNR device than in the 270-nm CNR device. Edge states, usually introduced by etching, will lead to the shorter life time of carriers in devices. Also, the 120-nm CNR device has a shorter channel length. This shorter length may help carrier extraction. The saturation trend was observed for both devices in Fig. 4.27c, which is similar to the graphite/MLG mesa devices in Chapter 2. However, our CNR-based photodetector did not show the greatly enhanced photoresponse as seen in some GNR devices reported in literature.[56] The reason are not clear.

4.3.3 Photoresponse Based on FIB-Induced CNRs

FIB patterning on graphite/MLG was realized to achieve very good ribbon quality with controlled ribbon width. A multilayer graphene mesa (15 nm thick) was firstly

fabricated on a SiO_2/Si substrate with the area of 14 x 24 μm. Then FIB patterning with proper parameters was applied to split the entire mesa into 2 zones: a MLG mesa (top) and a 40-nm ribbon array (bottom) (see Fig. 4.28a and Fig. 4.28b). With an asymmetric metal scheme, we built photodetectors on this FIB modified MLG sample (see Fig. 4.28). 2 pairs of metal (Ti and Pd) schemes were built in 2 parallel zones with the same separation space (1.1 μm) and electrode width (3 μm), in an attempt to limit the effect of channel length and contact area among these two detectors. Both of the 2 connections were separately applied into the photocurrent measurement circuit system for the comparison of performance in photoresponse.

Fig. 4.28a and Fig. 4.28b show the burned device after the laser experiment, which is due to the high temperature confined on top of SiO_2/Si substrate under the laser beam. For the 40-nm ribbons zone, 9 ribbons were buried under metal electrodes. Thus, the active area between the two leads for this zone is 5.04 μm^2 (9 x 40 nm x 14 μm for the 40-nm ribbon array), while the MLG mesa-based device (Top, Fig. 4.28a and Fig. 4.28b) has an active area of 46.2 μm^2 (3 μm x 14 μm). A 450-nm continous-wave laser was used here with tunable power output. The photoresponse of the 2 devices is shown in Fig. 4.29.

Under the near-uniform laser beam of 3.9 mW, the calculated photoresponsivities of the two devices shown in Fig. 4.28 are 32.9 mA/W (CNRs device) and 7.8 mA/W (MLG mesa device), respectively. This high photoresponse was obtained because a very low laser power limits the thermal influence on our devices. When the laser power is as high as 178 mW, the photoresponsivities of the CNRs and MLG mesa devices are reduced to 0.90 mA/W and 0.36 mA/W, respectively. We could expect that increasing ribbon

density in the array will further improve the photoresponse, which is indeed confirmed in the device based on the FIB-patterned EG ribbon devices.

For the photodetector based on the FIB-patterned EG CNR array, the Pt lead, with a higher work function than Pd (ϕ = 5.4 eV), was deposited on one side of the array by employing electron beam induced deposition, which is a simple function of the FIB machine. A relatively slow deposition rate was achieved using e-beam conditions of 2 kV and 0.8 nA. This yielded a 30-nm thick Pt film. We then built the asymmetric metal scheme by depositing the Ti on the other side of ribbon array via EBL and a lift-off process. This formed a device based on the smallest nanoribbons we were able to fabricate (see Fig. 4.30).

The active area of the device between the two leads was ~7.2 μm^2 (300 x 20nm x 1.2μm), much larger than the area produced by FIB patterning on the MLG mesa (see Fig. 4.28). The photoresponse of this device is shown in Fig. 4.31. Photocurrent signal as high as ~2 μA was achieved. This is because the laser spot is very large, and it is possible for the photocurrent to be generated from both the Pt/EG and Au/EG interfaces, in addition to the Ti-CNRs-Pt junctions. With a 500 μm laser spot irradiating the center of the device, the photocurrent vs. power curve shows a linear relationship, which is similar to the EG device performance in Chapter 3. This further verified that the good thermal conductivity of the SiC substrate, compared with SiO_2, leads to the minimized thermal effect so that the resistivity of the graphene at high T is not affected so much. By the measurement of light reflection (see Fig. 4.32), we observed that light refection on the Ti and Au leads is much higher than the Pt lead. Most of contributions to the photocurrent signal were from the active part of the ribbon array and the adjacent Pt/EG interface.

To summarize this chapter, we first realized the fabrication of CNRs on graphite and MLG by using EBL technology. Ribbon size as low as 35 nm was achieved on bulk graphite film with a high aspect ratio, and isolated, >100-nm CNRs were made by etching through multilayer graphene on SiO2/Si substrate. In addition, the FIB was used to directly remove carbon materials and then to fabricate CNRs. We successfully patterned CNRs on both MLG mesas and EG on SiC, and CNRs down to ~15nm were fabricated. It is notable that a large-area array of ~400 nanoribbons on 10-layer EG was achieved for the first time, whose ribbon width is only ~20 nm.

By building CNR-based devices, we tested the photoresponse in multi-CNR-based detectors. The results showed greater photoresponse, compared to graphene/graphite film-based devices. Photodetectors based on a CNR array by FIB patterning showed greater photoresponse than those by EBL patterning because the direct FIB patterning yields a clean ribbon surface as well as good edges.

Table 4.1 Parameters used for EBL based on PMMA processing

E-beam Lithography	
Parameter	**Setpoint**
950K PMMA from Micro Chem Inc.	in anisole (2%)
Spin coating	1000rpm @ 45sec
Bake	180°C on Hotplate @ 90sec
E-beam exposure	Dose 50 - 500 μC/cm2 (vary with different machines and conditions)
Developer	1:3 MIBK:IPA @ 30sec
Rinse	DI water
Post-baking	100°C on Hotplate @ 90sec

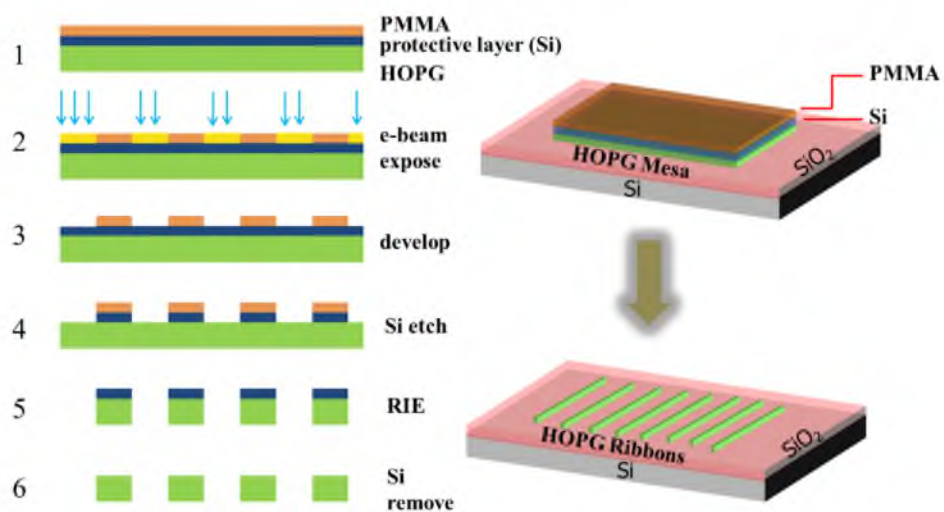

Figure 4.1 EBL patterning on HOPG mesa. Left: schematic process flow of EBL patterning on HOPG mesa (cross-sectional). Here, PMMA is used as a positive resist. Right: schematic 3D view of a HOPG mesa on SiO_2/Si converted to an array of CNRs array by EBL.

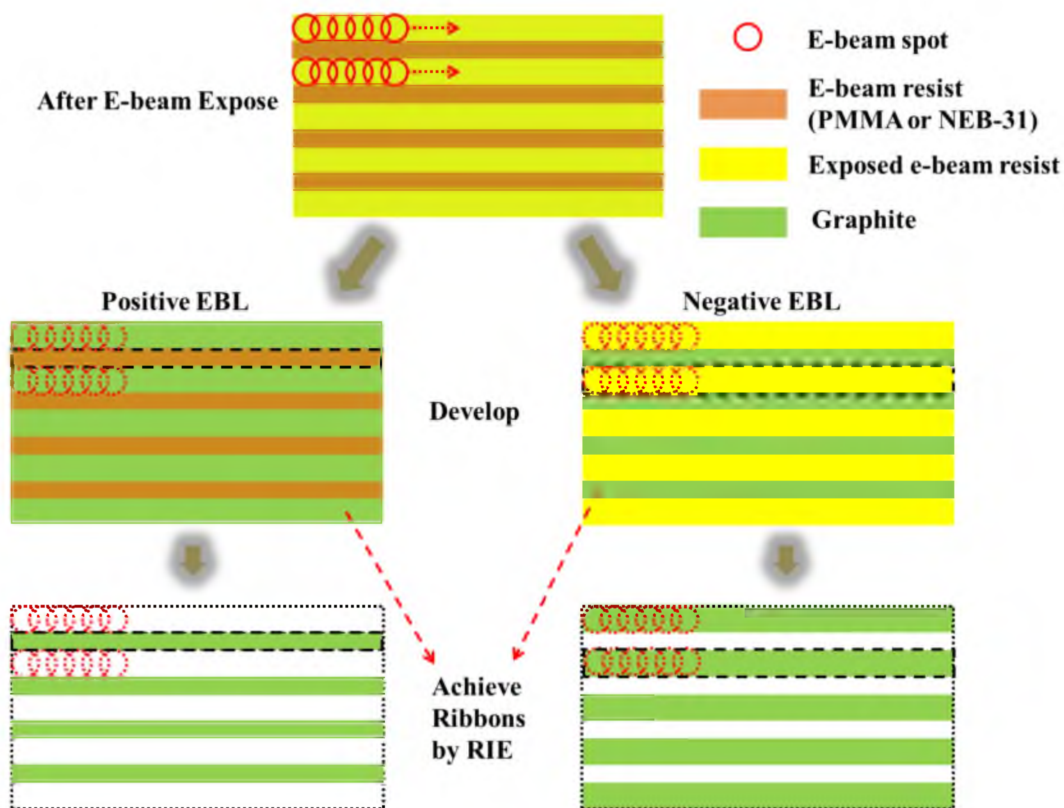

Figure 4.2 Schematic process flow of EBL patterning on a HOPG mesa (Top-view). The silicon protective layer and the SiO_2/Si substrate are not included here for simplicity. The dashed red arrow indicates the etching of exposed graphite in the final RIE process, and the dashed red box shows the CNRs formed by RIE, and the dashed red circle indicates the position of e-beam scans.

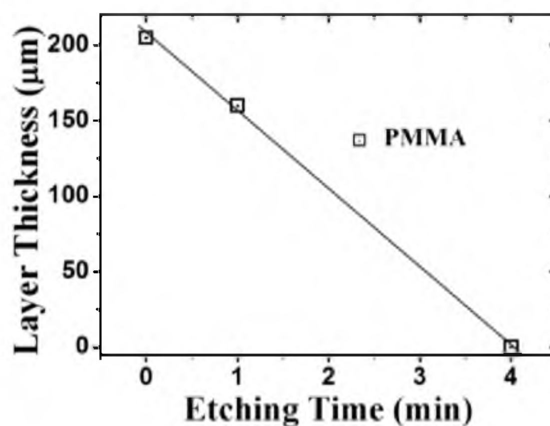

Figure 4.3 Etching test of 950K PMMA under O_2 RIE at 75W, and the fitted slope shows that the etch rate is ~52 nm/min.

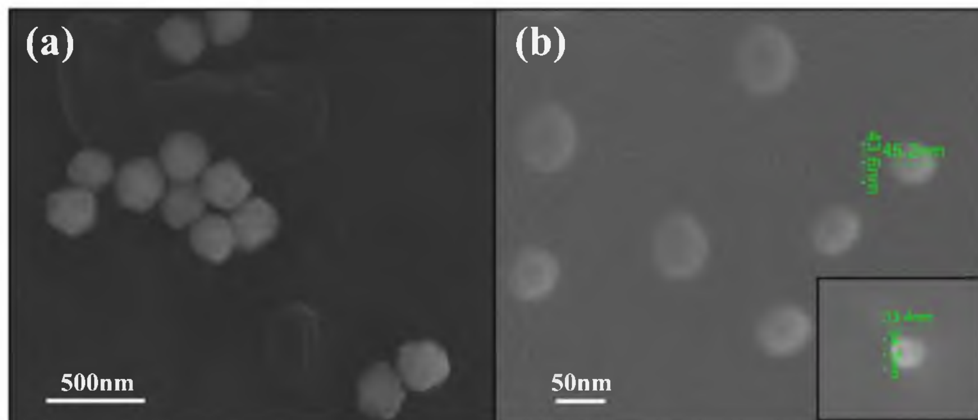

Figure 4.4 Stigmation modulation by the procedure to get the best Au balls and e-beam spot. (a) Successful stigmation tuning to get a clear Au ball SEM image. (b) Testing of the e-beam spot on the PMMA layer, which covers the Ti/Au lead in TA. Different spots were produced by 10-second e-beam illumination. Inset shows an optimized beam of ~35nm in spot size.

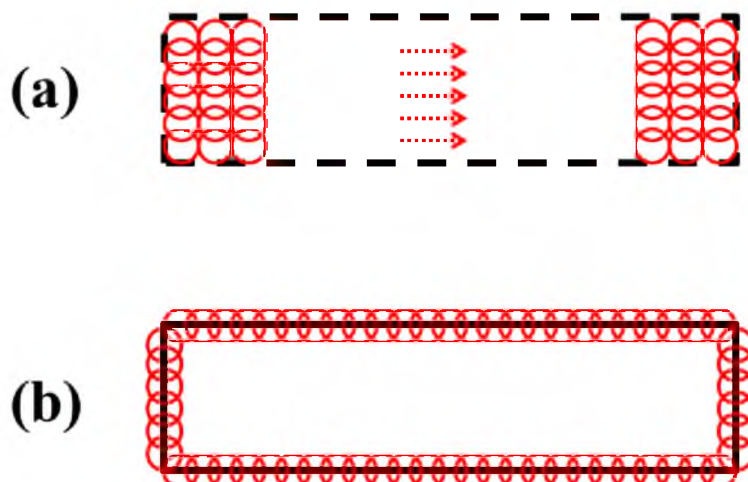

Figure 4.5 Schematic drawing of EBL patterns designed by DesignExpress software. The Red circle represents the e-beam spot. (a) Closed dashed box: e-beam spots will fill in the box during EBL writing. (b) Closed solid box: e-beam will write along the solid line.

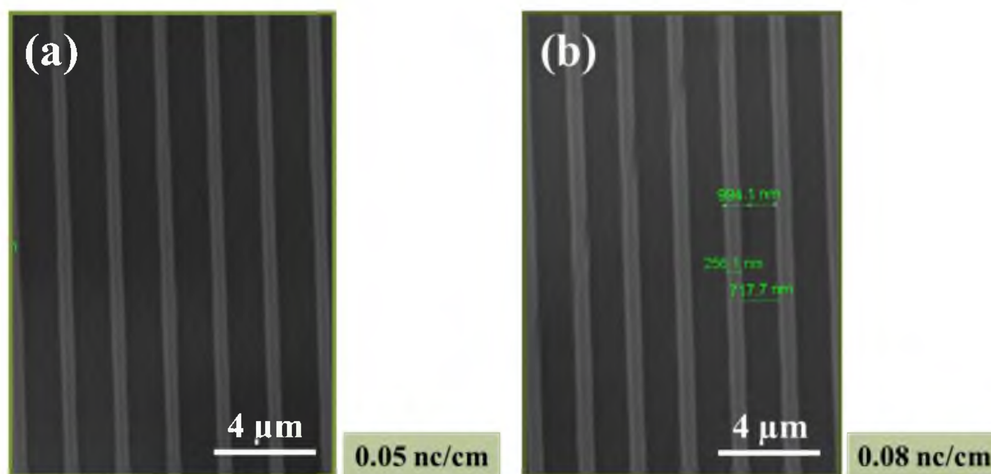

Figure 4.6 SEM images of EBL-patterned CNRs (~250nm wide) with two different e-beam line doses: (a) 0.05 nC/cm and (b) 0.08 nC/cm.

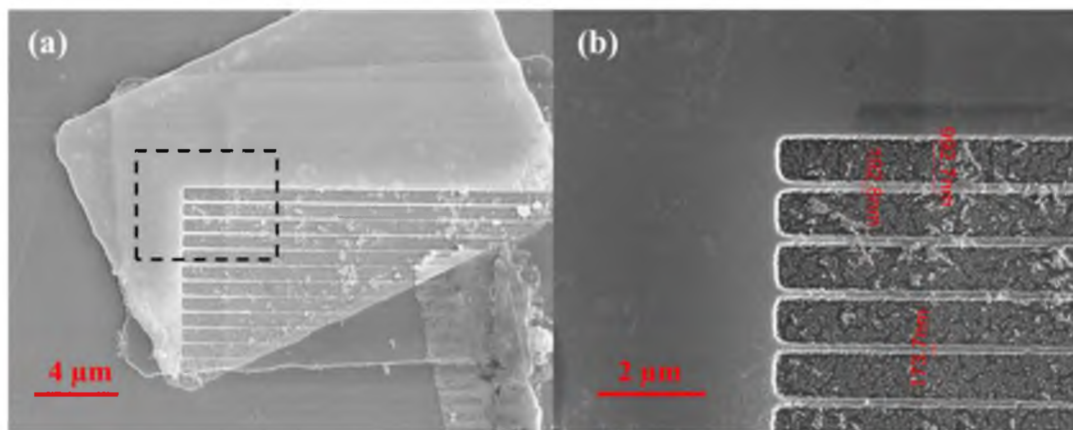

Figure 4.7 SEM characterization of EBL defined CNRs. (a) EBL patterning on drifted HOPG mesa. (b) Enlarged SEM image of the area confined in the dashed rectangle in (a).

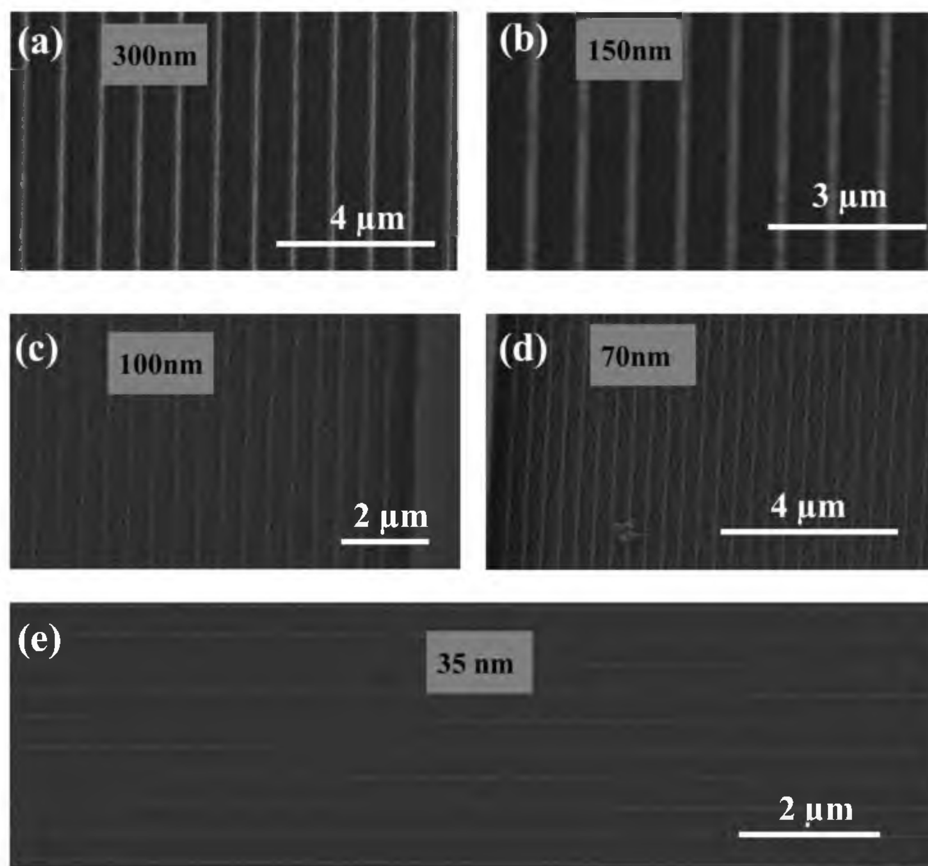

Figure 4.8 SEM images of EBL patterned CNRs on HOPG mesas. Different widths of ribbons were produced: (a) 300 nm, (b) 150 nm, (c) 100 nm, (d) 70 nm, and (e) 35 nm.

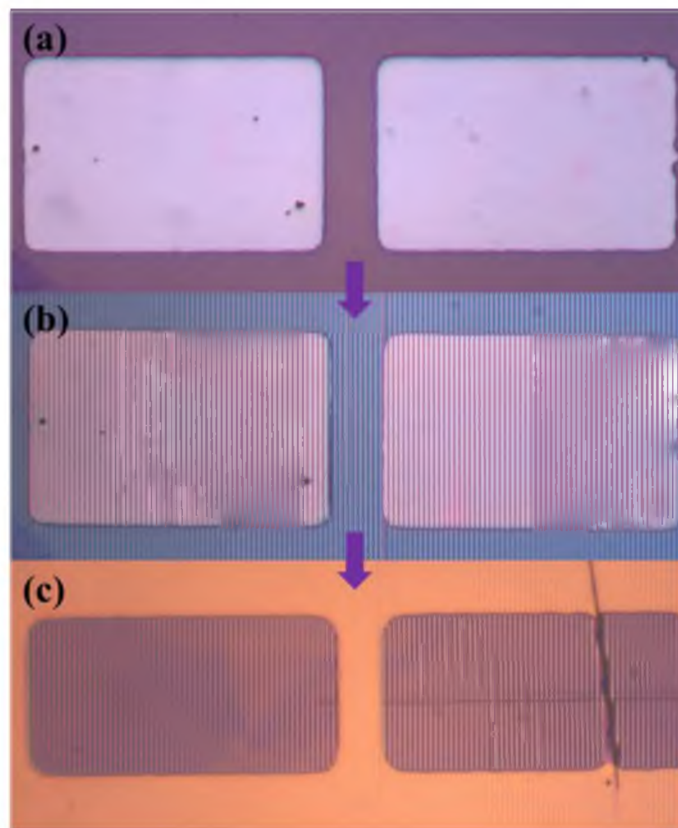

Figure 4.9 Optical images showing the CNRs fabrication flow. (a) Two 40 x 60 µm HOPG mesas with a thickness of ~80 nm, protected by a 50-nm thick Si layer, (b) EBL-patterned PMMA ribbons on top of HOPG mesas in (a), and (c) 10 min O_2 plasma etching to reveal the SiO_2 substrate in between ribbons. The size of mesa used here is 30 x 60 µm, and finally 270-nm CNRs were achieved.

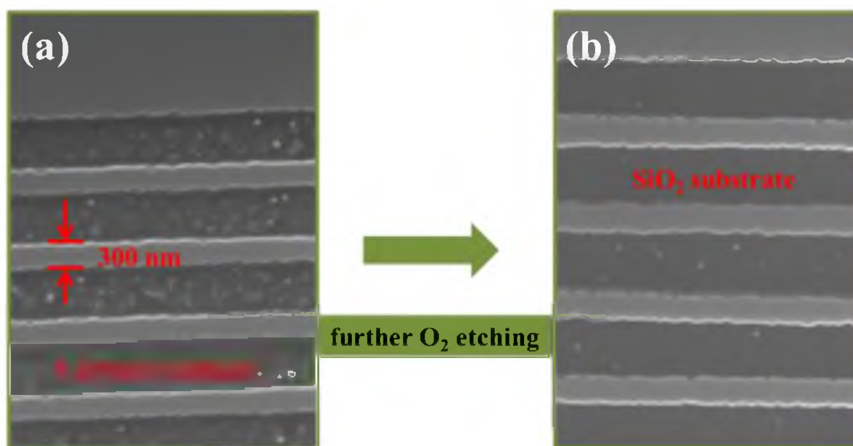

Figure 4.10 Etching-through of CNRs as seen by SEM imaging. (a) 300-nm wide CNRs with carbon residuals in between. (b) Clean with exposed substrate achieved by supplementary O_2 RIE.

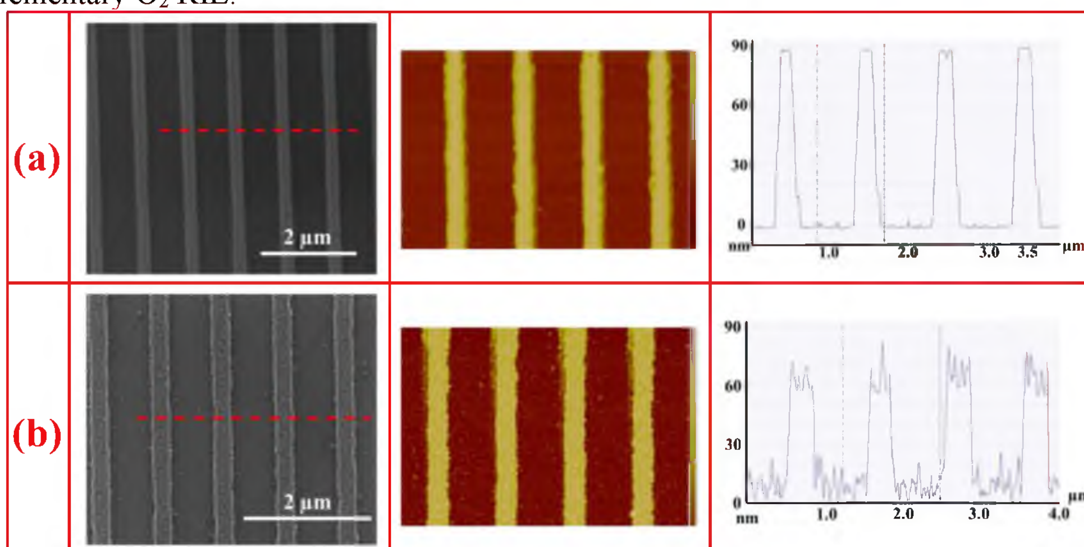

Figure 4.11 Surface analyses of CNRs by SEM and AFM, with the completion of two processes: (a) O_2 plasma etching of HOPG to form ribbons. (Left: SEM image, Middle: AFM scan of the same sample, Right: Depth profile along the dashed line in left SEM image), (b) SF_6 plasma etching to remove protective Si (Left: SEM image, Middle: AFM scan of the same sample, Right: Depth profile along the dashed line in left SEM image). Z-scale in the middle AFM images is 120 nm. CNRs are 250–300 nm wide and ~35nm thick, covered by 50-nm thick Si.

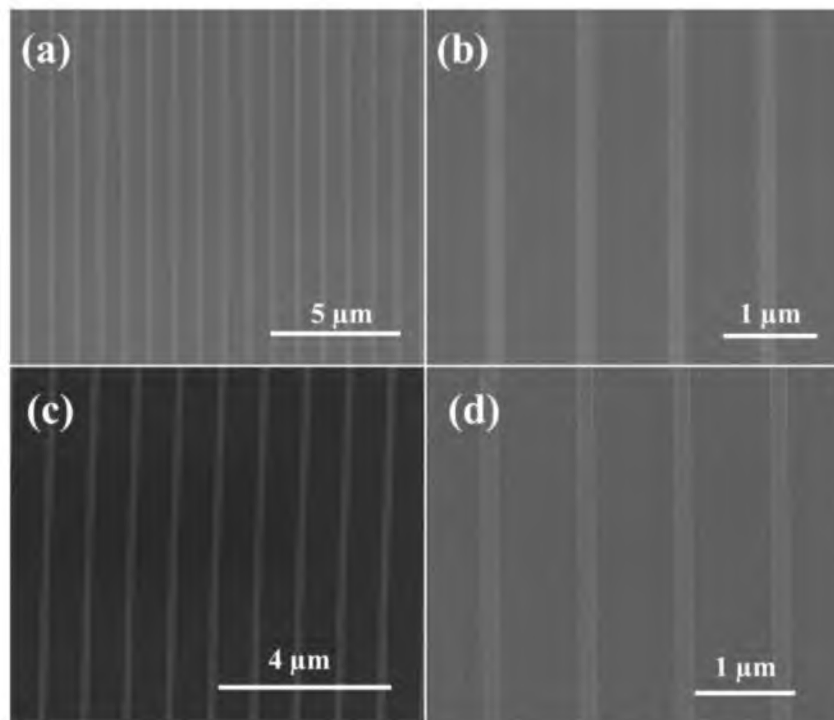

Figure 4.12 SEM imaging of isolated CNRs on SiO_2/Si substrate. Ribbons are 150–200 nm wide. (a), (b), and (c) CNRs covered with Si protective layer. (d) Pure CNRs through the removal of the covered Si.

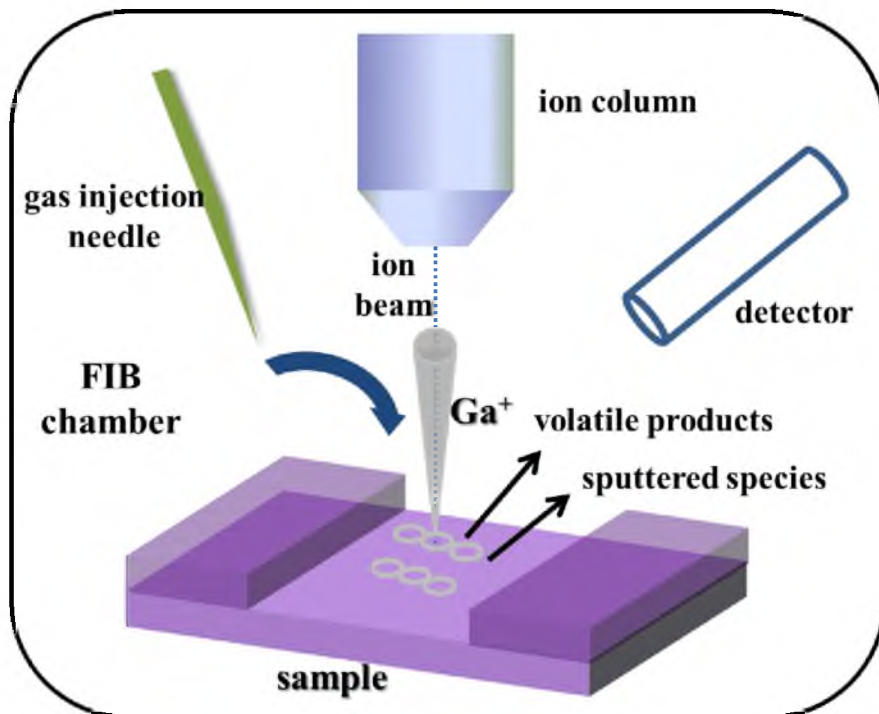

Figure 4.13 Schematic drawing of the structure of the FIB chamber and the controlled material removal process.

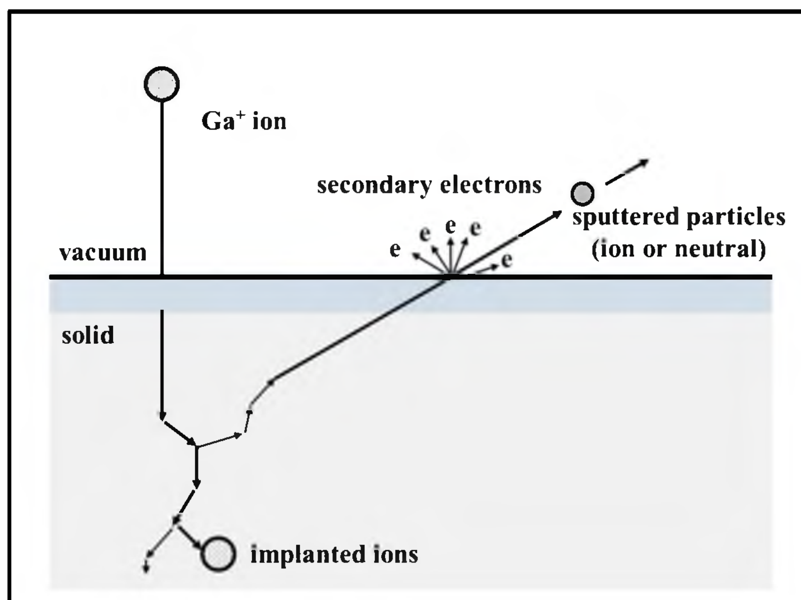

Figure 4.14 Schematic diagram of the sputtering process and ion-solid interactions.

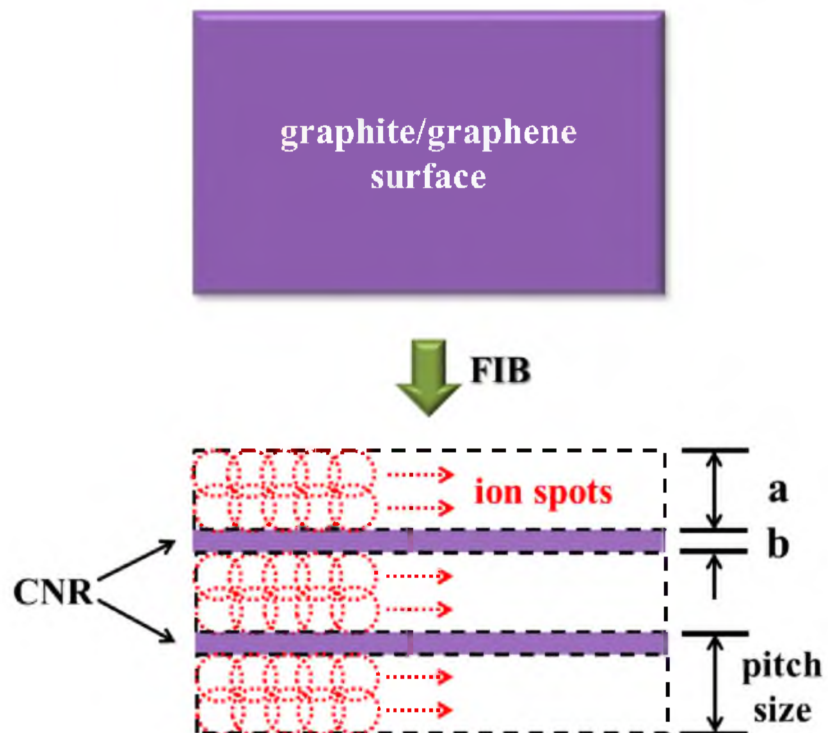

Figure 4.15 Schematic diagram of CNRs patterning process by FIB. The dashed red circle represents the Ga ion beam spot arrays, which fill the dashed boxes. A pitch size composed of the etching box (area) width *a* and ribbon width in pattern *b* is defined here.

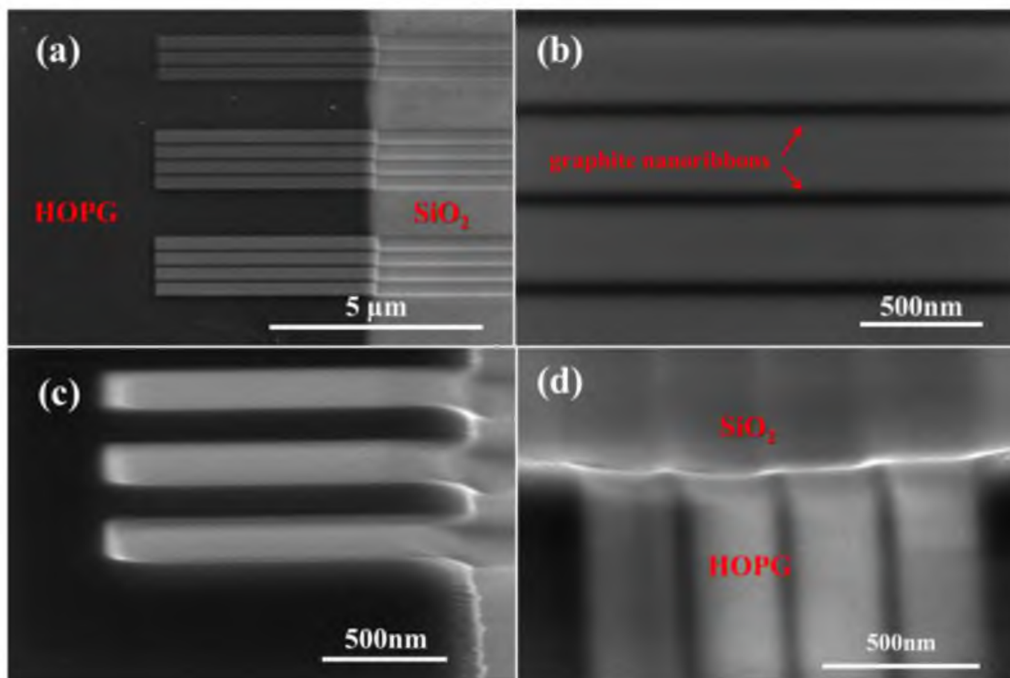

Figure 4.16 SEM characterization of FIB-patterned HOPG CNRs. (a) Ribbons with different widths by FIB patterning. (b) 45–50 nm ribbons. (c) 200-nm ribbons. (d) 40-nm ribbons.

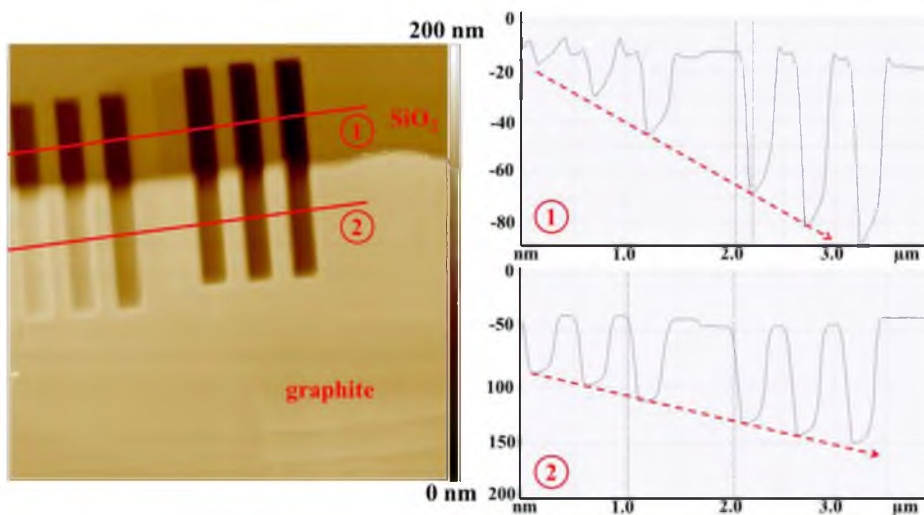

Figure 4.17 AFM characterization of FIB patterned HOPG ribbons with different beam doses (left). AFM image of HOPG ribbons on SiO_2/Si substrate. SiO_2 is etched by the Ga ion beam as well. (Right) Depth measurement along the red line shown in the left image, for both SiO_2 ribbons (up) and HOPG ribbons (down).

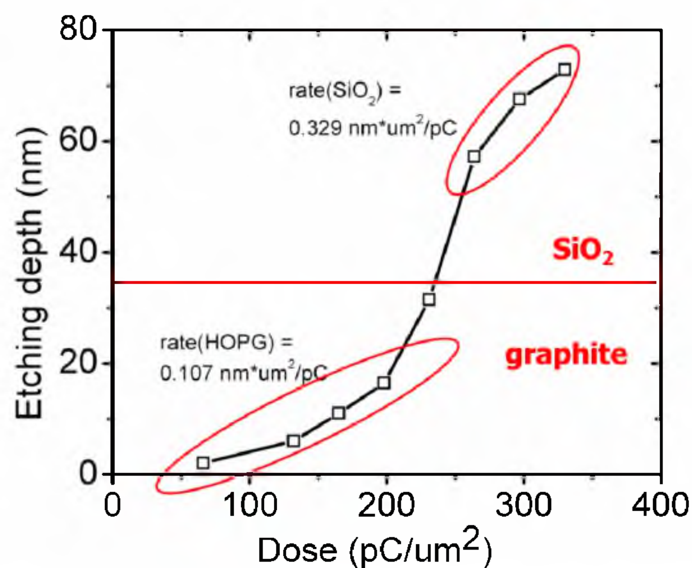

Figure 4.18 FIB etching depth of HOPG on SiO_2 (300 nm) as a function of ion beam dose. The etch rates of SiO_2 and HOPG by FIB are 0.329 nm-μm^2/pC and 0.107 nm-μm^2/pC, respectively.

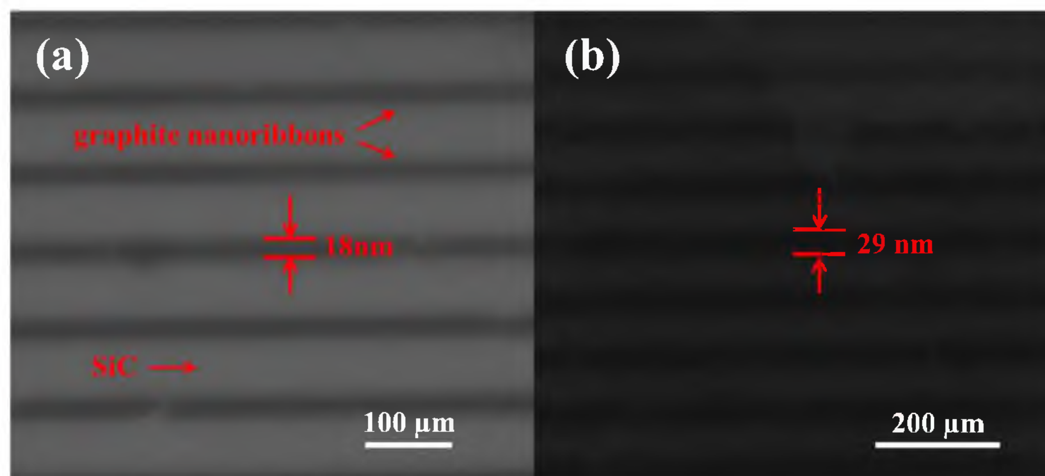

Figure 4.19 SEM pictures of FIB-patterning on thick (10-layer) and thin (2-layer) EG. (a) 18-nm thick CNR array. (b) 29-nm thin CNR array.

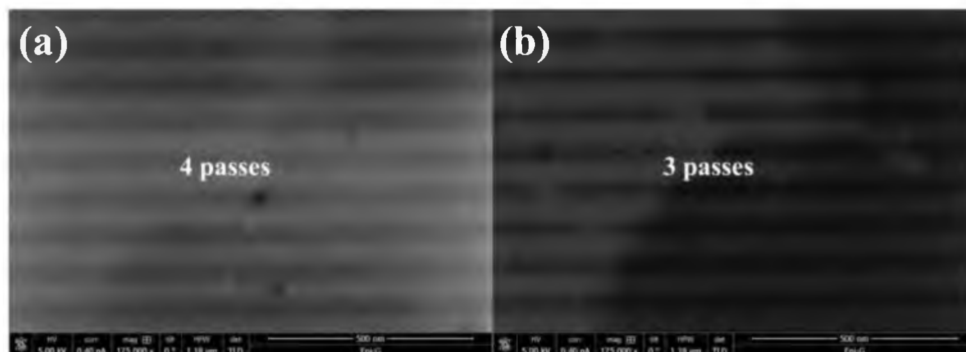

Figure 4.20 SEM imaging to compare two different passes of ion beam scanning at the same dose: ~30 pC/μm^2. (a) 4 passes. No ribbons were obtained due to the over exposed etching area. (b) 3 passes. 24-nm wide ribbons were achieved.

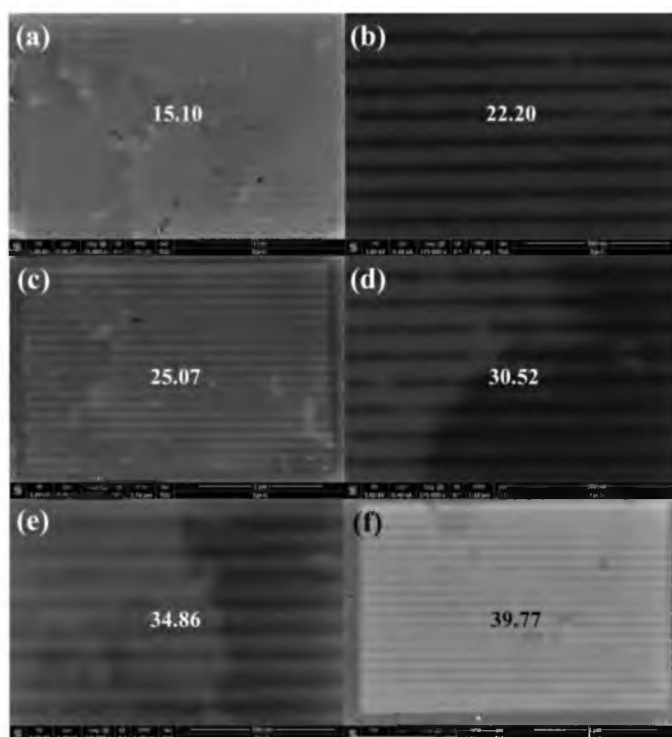

Figure 4.21 SEM characterization of graphene nanribbons on 10-layer EG sample by FIB-patterning with 3 passes of scanning. Different doses were tested: (a) 15.10 pC/μm^2, (b) 22.20 pC/μm^2, (c) 25.07 pC/μm^2, (d) 30.52 pC/μm^2, (e) 34.86 pC/μm^2, and (f) 39.77 pC/μm^2.

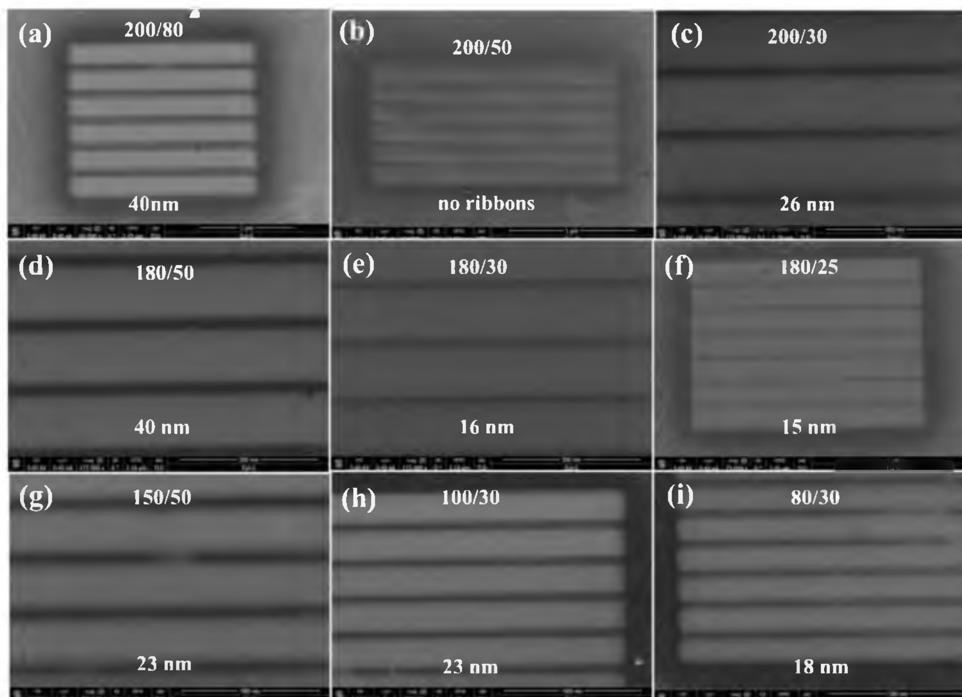

Figure 4.22 SEM images of FIB-patterned nanoribbons on a 10-layer EG sample with different pitch sizes: (a) a/b = 200/80 nm, 40-nm ribbons were achieved; (b) a/b = 200/50 nm, no EG ribbons were fabricated; (c) 200/30 nm, 26-nm ribbons; (d) 180/50 nm, 40-nm ribbons; (e) 180/30 nm, 16-nm ribbons; (f) 180/25 nm, 15-nm ribbons; (g) 150/50 nm, 23-nm ribbons; (h) 100/30 nm, 23-nm ribbons; and (i) 80/30 nm, 18-nm ribbons.

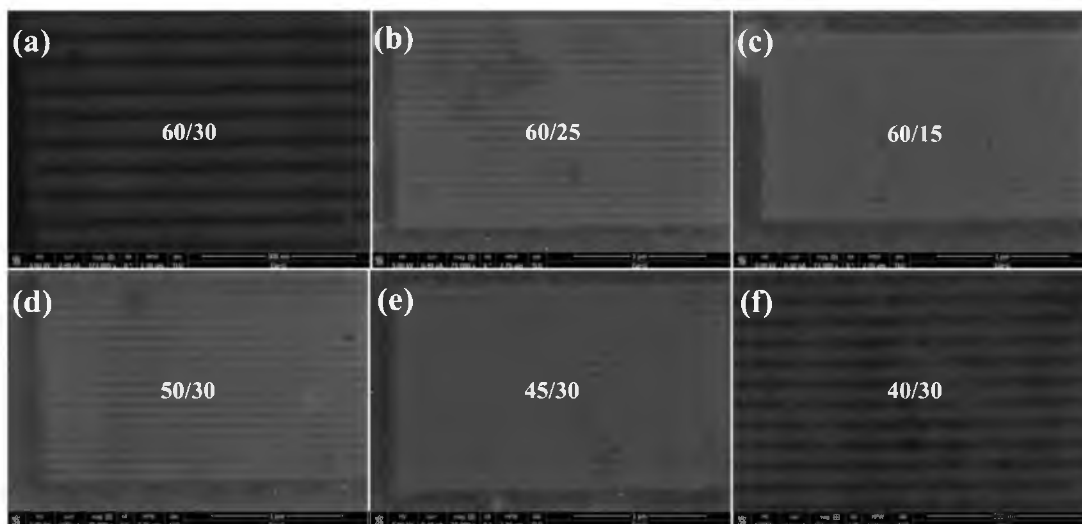

Figure 4.23 SEM images of FIB-patterned nanoribbons on a 10-layer EG sample with different pitch combinations: (a) a/b = 60/30 nm, (b) 60/25 nm, (c) 60/15nm, (d) 50/30 nm, (e) 45/30 nm, and (f) 40/30 nm.

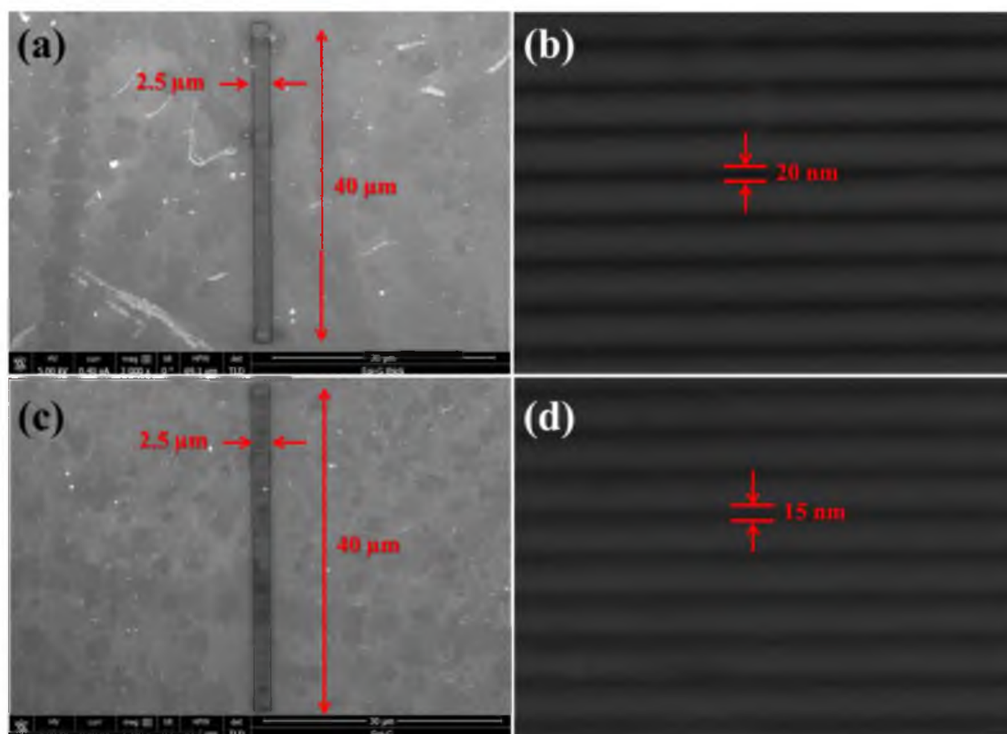

Figure 4.24 Surface characterization of FIB-patterned graphene nanoribbon arrays on EG film by SEM. (a) a 2.5 x 40 µm array containing ~400 ribbons on thick EG film; (b) zoom-in image for the 20-nm ribbons with good quality; (c) a 2.5 x 40 µm array containing ~400 ribbons on thin EG film; (d) zoom-in image for the 15-nm ribbons in a certain area with good EG film quality.

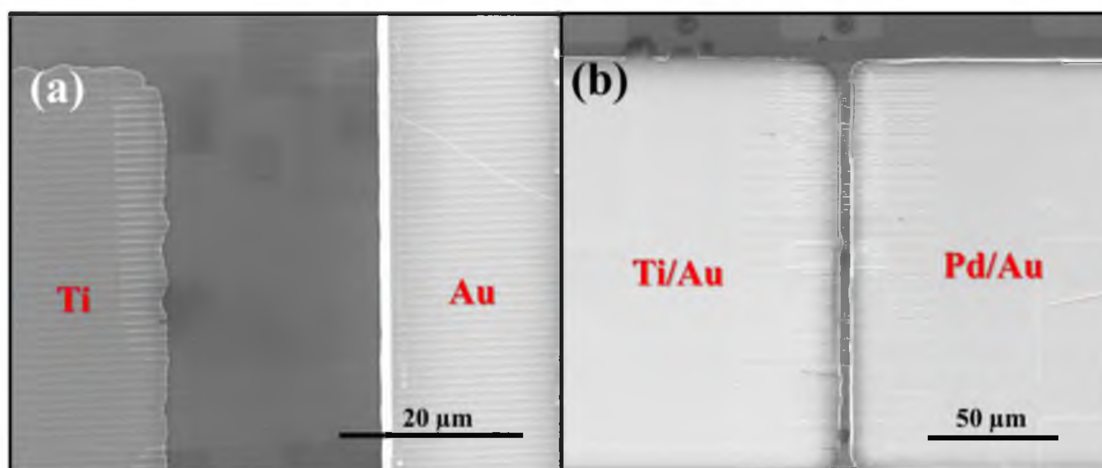

Figure 4.25 SEM imaging of devices with asymmetric metal leads on graphite nanoribbons. (a) Ti-CNRs-Au device and (b) Ti-CNRs-Pd device.

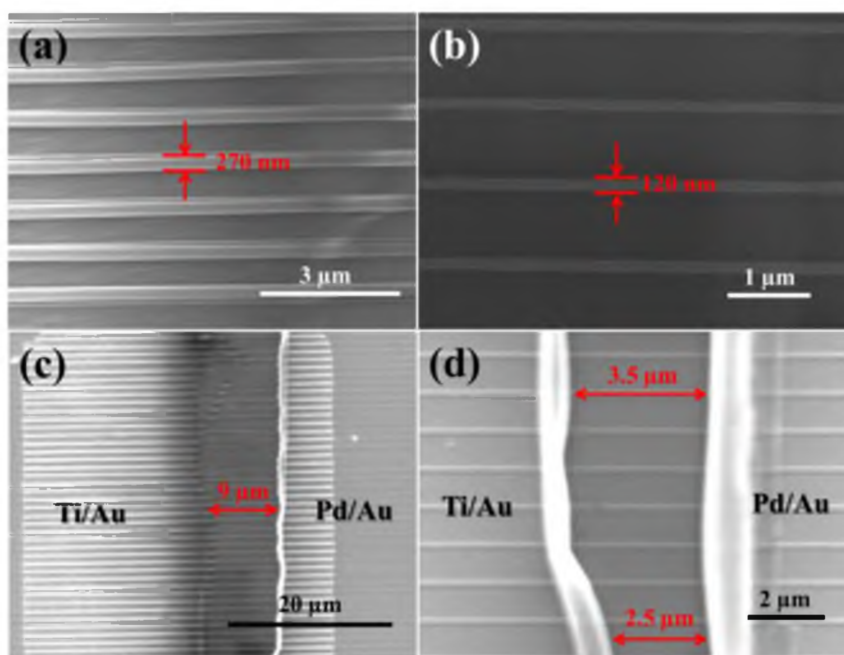

Figure 4.26 SEM imaging of graphite nanoribbons with different widths: (a) 270nm; (b) 120 nm, which were used for the devices based on Ti and Pd electrodes (c) device using 270nm graphite ribbons shown in (a); (d) device using 120-nm graphite ribbons shown in (b).

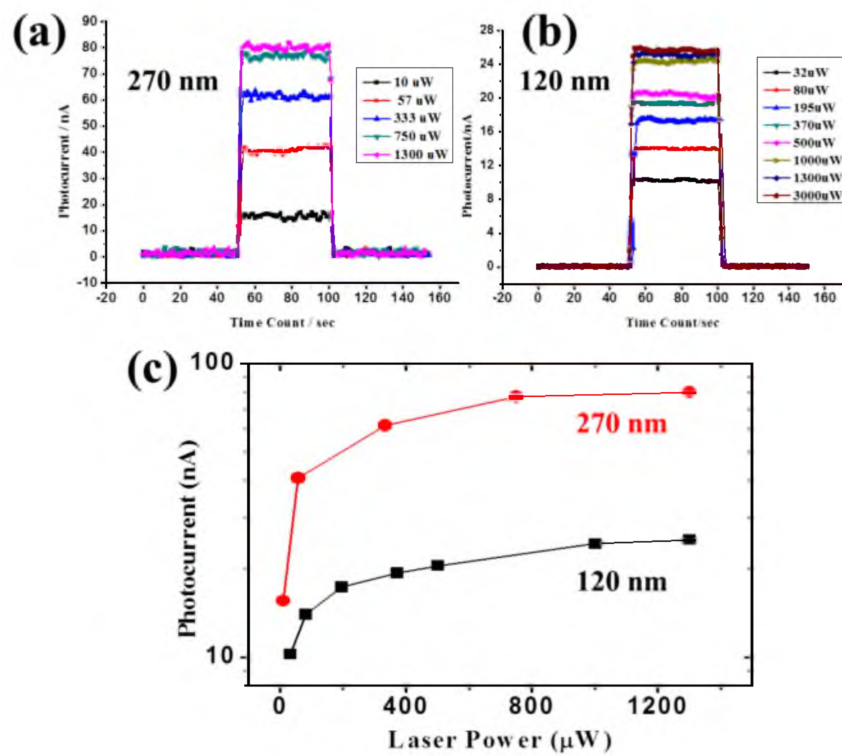

Figure 4.27 Photoresponse testing of the 270-nm CNRs and 120-nm CNRs devices. Photocurrents measured with the increasing testing duration are shown in (a) and (b) for the two devices. (c) Photocurrent as a function of laser power for both devices.

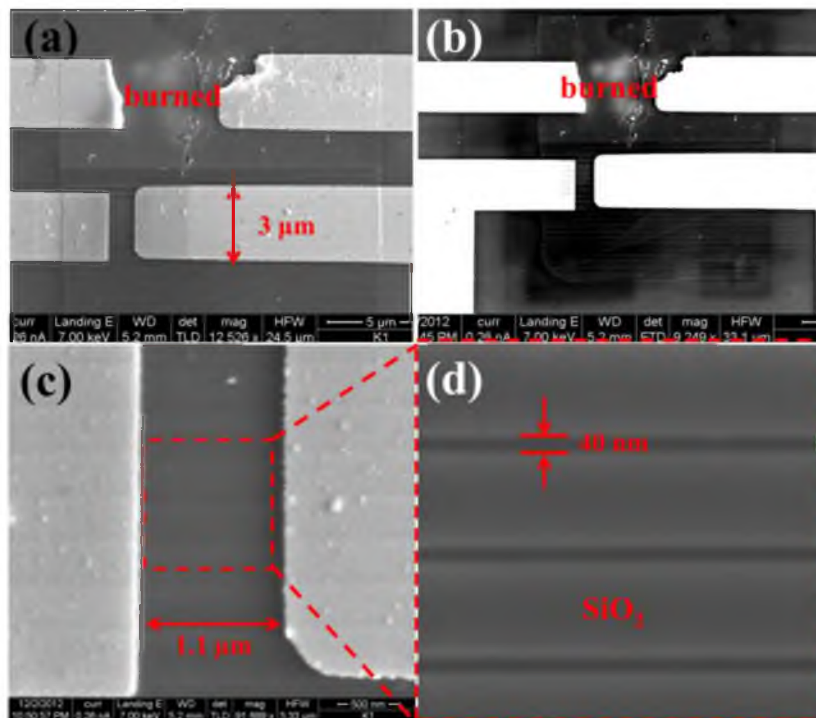

Figure 4.28 SEM characterization of photodetectors based on a FIB-patterned MLG mesa (14 x 24 µm). (a) and (b) photodetectors built on 2 zones: a MLG mesa (top) and a 40-nm wide CNRs array (bottom); (c) photodetector on 40-nm ribbons array; (d) enlarged image to show the MLG ribbons in (c).

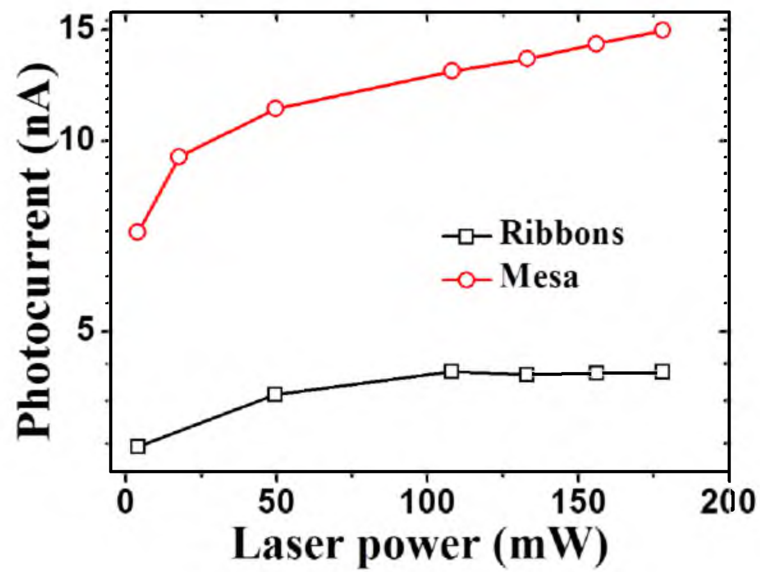

Figure 4.29 Photocurrent vs. laser power, for the 3 connections built on the 3 different zones.

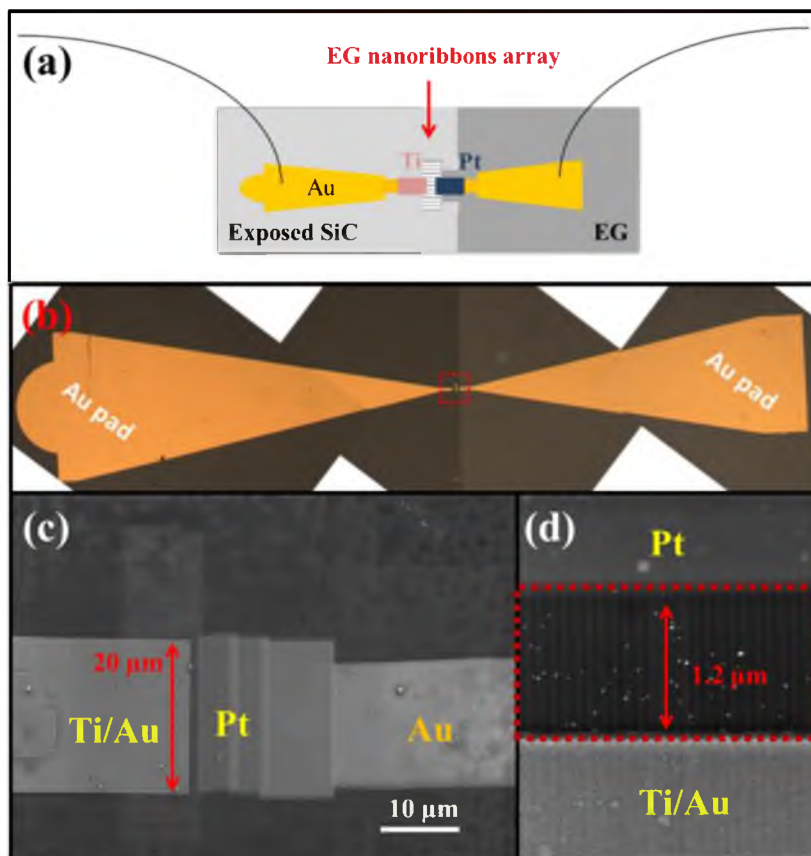

Figure 4.30 Schematic drawing and surface characterization of the Ti-CNRs-Pt device based on a large-area EG nanoribbon array. (a) Schematic diagram of the device after fabrication. (b) Optical image showing the entire device. (c) SEM imaging of the main detection area in the dotted box shown in (b). (d) Ti-CNRs-Pt configuration with 1.2-µm uniform separation between the 2 gaps.

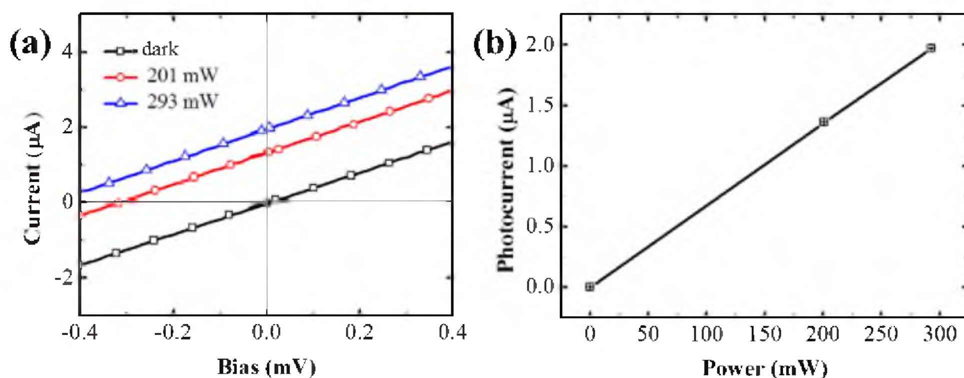

Figure 4.31 Photoresponse of the Ti-CNRs-Pt device under 450-nm laser illumination. (a) current-bias curves under different laser output. (b) Photocurrent as a function of laser power.

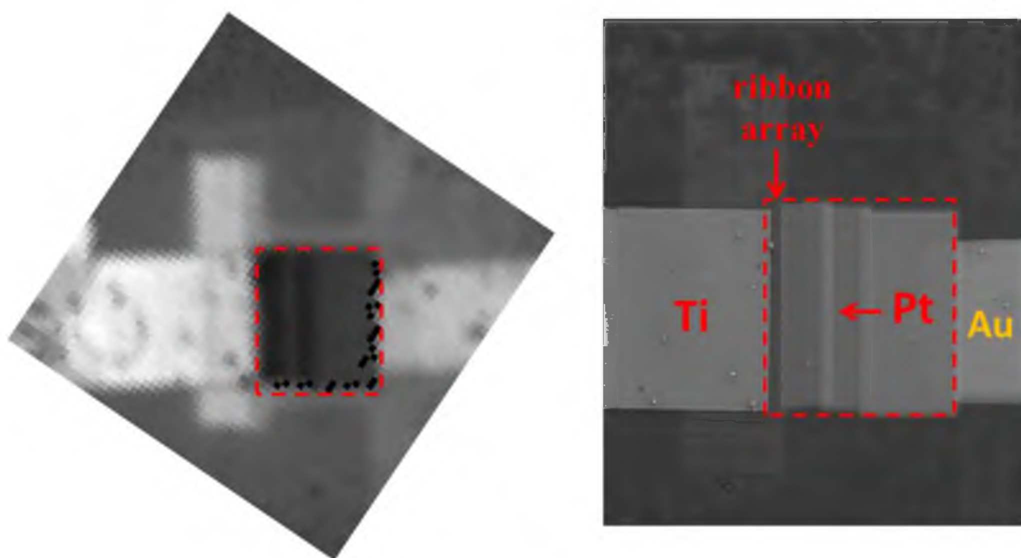

Figure 4.32 Characterization of CNR-based photodetector. Characterization of light reflection (left). SEM image (right) shows the same zone with dashed box as the one marked in left figure.

CHAPTER 5

CONCLUSION

In this research, we first developed experimental methods and processes to cleave, thin, and bond graphitic films to dielectric substrates. We next developed optical lithography to fabricate graphite mesas on the micron scale. During this process, Si was tested and chosen to deposit on top of graphite films for protection, and anisotropic O_2 RIE with a steady etching rate was applied for the removal of carbon materials. The resistance of PMMA and PR s1813 to plasma etching (O_2 and SF_6) was researched as well.

To build a MLG/graphite-based photodetector, we used islands with random shapes and graphite mesas defined by optical lithography. Symmetric and asymmetric metal configurations were deposited using optical lithography followed by lift-off process. EBL and related lift-off processes were also studied to successfully create metal leads on a substrate with very precisely controlled dimension and clean edges.

An attempt to use Ti and Au to form a metal scheme was unsuccessful. Ti and Pd covered with Au protective layers were then used and found sucessful, and Pt was used to replace Pd in some of our devices.

The graphitic films-based photodetectors showed great photoresponse under laser illuminations. The photoresponsivities varied with the film thickness (related to the light

absorption rate), metal lead coverage, channel length, and the quality of the devices. We then demonstrated photoresponse in large-area EG/SiC devices with asymmetric metal contacts for both 2-layer and 10-layer EG samples. Photocurrent was generated from the internal electric field at the metal/EG junctions due to the work function difference. High photoresponsivity was achieved under both a single wavelength blue laser illumination (1.11 mA/W at 0V bias) and an AM 1.5 visible light source (4.08 mA/W at 0V bias). The biased EG-based photodetector showed a photoresponse as high as 4.5 mA/W at 0.7V. The device performance is shown to be highly tunable by varying metal lead, EG layer thickness, channel length, and/or illumination area. The extraction of photon-induced electron carriers in the EG device was demonstrated to be faster than that of the SiC device.

We also fabricated CNRs by using EBL technology and the direct FIB patterning. EBL was used to pattern CNRs on the graphitic mesas defined by optical lithography. The developed procedure involved transfer of the EBL-patterned PMMA ribbon structure to the Si layer by RIE and then to the MLG/graphite mesas to generate CNRs. A minimum width of ~35 nm was achieved with a very high aspect ratio. However, CNRs generated by EBL involved a multistep process, solution-based and etching-introduced, so that the final ribbons may have high surface and edge roughness. Defects and edge states may have been introduced.

We finally developed protocols for FIB-patterning of CNRs directly on a graphitic substrate. Based on the large spot size of the Ga ion beam, we achieved CNR arrays with the nanoribbon width as low as 13 nm. The etch rate of carbon materials as a function of dose was studied in order to adequately etch both MLG and EG films and to expose

substrates (SiO_2 or SiC) in between ribbons. Many factors, which may affect the ribbons size and qualities, were thoroughly researched. Finally, a large CNR array with an average ribbon width of ~20 nm was fabricated and built into a device.

CNR-based photonic devices were fabricated. Under laser illumination, the CNR devices exhibited better photoresponse than graphite flake devices; this is mainly because of the improved metal/carbon contact (area/length). In addition to the graphene/lead interfaces formed on the top carbon layer of graphite, more internal electric fields were created between side-covered metal leads and the edges of multiple graphene layers inside a graphitic film.

REFERENCES

[1] K. S. Novoselov, A. K. Geim, S. V. Morozov, D. Jiang, Y. Zhang, S. V. Dubonos, I. V. Grigorieva, and A. A. Firsov, Science **306**, 666 (2004).

[2] K. Novoselov, V. Fal'ko, L. Colombo, P. Gellert, M. Schwab, and K. Kim, Nature **490**, 192 (2012).

[3] A. Balandin, S. Ghosh, W. Bao, I. Calizo, D. Teweldebrhan, F. Miao, and C. Lau, Nano Lett. **8**, 902 (2008).

[4] J. Hu, X. Ruan, and Y. Chen, Nano Lett. **9**, 2730 (2009).

[5] X. Du, P. Guo, H. Song, and X. Chen, Electrochim. Acta **55**, 4812 (2010).

[6] I. Frank, D. M. Tanenbaum, A. Van der Zande, and P. L. McEuen, J. Vac. Sci. Technol., B: Microelectron. Nanometer Struct. **25**, 2558 (2007).

[7] A. Geim and K. Novoselov, Nat. Mater. **6**, 183 (2007).

[8] M. Allen, V. Tung, and R. Kaner, Chem. Rev. **110**, 132 (2010).

[9] J. Charlier, P. Eklund, J. Zhu, and A. Ferrari, Top. Appl. Phys. **111**, 673–709 (2008).

[10] P. Avouris, Z. Chen, and V. Perebeinos, Nat. Nanotechnol. **2**, 605 (2007).

[11] K. Novoselov, D. Jiang, F. Schedin, T. Booth, V. Khotkevich, S. Morozov, and A. Geim, Proc. Natl. Acad. Sci. U.S.A. **102**, 10451 (2005).

[12] M. I. Katsnelson, Mater. Today **10**, 20 (2007).

[13] S. V. Morozov, K. S. Novoselov, M. I. Katsnelson, F. Schedin, D. C. Elias, J. A. Jaszczak, and A. K. Geim, Phys. Rev. Lett. **100**, 016602 (2008).

[14] A. Mayorov, et al., Nano Lett. **11**, 2396 (2011).

[15] E. B. Ramayya, D. Vasileska, S. M. Goodnick, and I. Knezevic, Nanotechnology, IEEE Transactions on **6**, 113 (2007).

[16] S. Y. Zhou, et al., Nat. Phys. **2** (2006).

[17] T. Stauber, N. M. R. Peres, and A. K. Geim, Phys. Rev. B **78**, 085432 (2008).

[18] M. Sprinkle, et al., Phys. Rev. Lett. **103**, 226803 (2009).

[19] A. Reina, X. Jia, J. Ho, D. Nezich, H. Son, V. Bulovic, M. Dresselhaus, and J. Kong, Nano Lett. **9**, 30 (2009).

[20] S. Sasha, A. D. Dmitriy, D. P. Richard, A. K. Kevin, K. Alfred, J. Yuanyuan, W. Yue, T. N. SonBinh, and S. R. Rodney, Carbon **45** (2007).

[21] W. A. de Heer, et al., Solid State Commun. **143**, 92 (2007).

[22] C. Berger, et al., Science **312**, 1191 (2006).

[23] X. Du, I. Skachko, A. Barker, and E. Andrei, Nat. Nanotechnol. **3**, 491 (2008).

[24] S. Bae, et al., Nat. Nanotechnol. **5**, 574 (2010).

[25] T. Ohta, A. Bostwick, T. Seyller, K. Horn, and E. Rotenberg, Science **313**, 951 (2006).

[26] Y. M. Lin, C. Dimitrakopoulos, K. Jenkins, D. Farmer, H. Y. Chiu, A. Grill, and P. Avouris, Science **327**, 662 (2010).

[27] J. Krupka and W. Strupinski, Appl. Phys. Lett. **96**, 082101 (2010).

[28] R. S. Singh, V. Nalla, W. Chen, A. T. S. Wee, and W. Ji, ACS Nano **5**, 5969 (2011).

[29] F. Varchon, et al., Phys. Rev. Lett. **99**, 126805 (2007).

[30] R. S. Singh, V. Nalla, W. Chen, W. Ji, and A. T. S. Wee, Appl. Phys. Lett. **100**, 093116 (2012).

[31] Y. Kopelevich and P. Esquinazi, Adv. Mater. **19** (2007).

[32] Y. Zhang, Y.-W. Tan, H. Stormer, and P. Kim, Nature **438**, 201 (2005).

[33] R. Nair, P. Blake, A. Grigorenko, K. Novoselov, T. Booth, T. Stauber, N. Peres, and A. Geim, Science **320**, 1308 (2008).

[34] F. Wang, Y. Zhang, C. Tian, C. Girit, A. Zettl, M. Crommie, and Y. Shen, Science **320**, 206 (2008).

[35] T. Mueller, F. Xia, and P. Avouris, Nat. Photon. **4**, 297 (2010).

[36] Y. Liu, R. Cheng, L. Liao, H. Zhou, J. Bai, G. Liu, L. Liu, Y. Huang, and X. Duan, Nat. Commun. **2**, 579 (2011).

[37] P. Blake, E. W. Hill, A. H. C. Neto, K. S. Novoselov, D. Jiang, R. Yang, T. J. Booth, and A. K. Geim, Appl. Phys. Lett. **91**, 063124 (2007).

[38] F. Xia, T. Mueller, Y.-m. Lin, A. Valdes-Garcia, and P. Avouris, Nat. Nano. **4**, 839 (2009).

[39] L. Prechtel, L. Song, D. Schuh, P. Ajayan, W. Wegscheider, and A. W. Holleitner, Nat. Commun. **3**, 646 (2012).

[40] F. Bonaccorso, Z. Sun, T. Hasan, and A. C. Ferrari, Nat. Photon. **4**, 611 (2010).

[41] B. Chitara, L. S. Panchakarla, S. B. Krupanidhi, and C. N. R. Rao, Adv. Mater. **23**, 5419 (2011).

[42] J. H. LeeEduardo, K. Balasubramanian, R. T. Weitz, M. Burghard, and K. Kern, Nat. Nano. **3**, 486 (2008).

[43] F. Xia, T. Mueller, R. Golizadeh-Mojarad, M. Freitag, Y.-m. Lin, J. Tsang, V. Perebeinos, and P. Avouris, Nano Lett. **9**, 1039 (2009).

[44] X. Xu, N. Gabor, J. Alden, A. van der Zande, and P. McEuen, Nano Lett. **10**, 562 (2010).

[45] M. Lemme, F. Koppens, A. Falk, M. Rudner, H. Park, L. Levitov, and C. Marcus, Nano Lett. **11**, 4134 (2011).

[46] K. Mak, M. Sfeir, Y. Wu, C. Lui, J. Misewich, and T. Heinz, Phys. Rev. Lett. **101**, 196405 (2008).

[47] K. Bolotin, K. Sikes, J. Hone, H. Stormer, and P. Kim, Phys. Rev. Lett. **101**, 96802 (2008).

[48] A. Akturk and N. Goldsman, in IEEE conference: Simulation of Semiconductor Processes and Devices, 2008 p. 173.

[49] W. Xu, F. Peeters, and T. Lu, Phys. Rev. B **79**, 73403 (2009).

[50] J. Yan, M. H. Kim, J. Elle, A. Sushkov, G. Jenkins, H. Milchberg, M. Fuhrer, and H. Drew, Nat. Nanotechnol. 7, 472 (2012).

[51] F. Marcus, L. Tony, X. Fengnian, and A. Phaedon, Nat. Photon. 7, 53–59 (2013).

[52] N. M. Gabor, J. C. W. Song, Q. Ma, N. L. Nair, T. Taychatanapat, K. Watanabe, T. Taniguchi, L. S. Levitov, and P. Jarillo-Herrero, Science **334**, 648 (2011).

[53] J. Viljas and T. Heikkilä, Phys. Rev. B **81**, 245404 (2010).

[54] Q. Bao and K. Loh, ACS Nano **6**, 3677 (2012).

[55] P. Wang, W. Zhang, O. Liang, M. Pantoja, J. Katzer, T. Schroeder, and Y.-H. Xie, ACS Nano **6**, 6244 (2012).

[56] M. Freitag, T. Low, W. Zhu, H. Yan, F. Xia, and P. Avouris, Nat. Commun. **4**, 1951 (2013).

[57] T. Mueller, F. Xia, M. Freitag, J. Tsang, and P. Avouris, Phys. Rev. B **79**, 245430 (2009).

[58] A. Urich, K. Unterrainer, and T. Mueller, Nano Lett. **11**, 2804 (2011).

[59] D. R. Lide, *CRC Handbook of Chemistry and Physics* (CRC Press, Boca Raton, Florida, 2005).

[60] U.S. Department of the Interior, Mineral Commodity Summaries (2011).

[61] M. Y. Han, B. Özyilmaz, Y. Zhang, and P. Kim, Phys. Rev. Lett. **98**, 206805 (2007).

[62] X. Li, X. Wang, L. Zhang, S. Lee, and H. Dai, Science **319**, 1229 (2008).

[63] D. E. Eastman, Phys. Rev. B **2**, 1 (1970).

[64] Q. Yan, B. Huang, J. Yu, F. Zheng, J. Zang, J. Wu, B.-L. Gu, F. Liu, and W. Duan, Nano Lett. 7, 1469 (2007).

[65] Z. F. W. and F. Liu, unpublished.

[66] X. Lu, H. Huang, N. Nemchuk, and R. S. Ruoff, Appl. Phys. Lett. **75**, 193 (1999).

[67] R. Legtenberg, H. Jansen, M. de Boer, and M. Elwenspoek, J. Electrochem. Soc. **142**, 2020 (1995).

[68] G. Giovannetti, P. Khomyakov, G. Brocks, V. Karpan, J. van den Brink, and P. Kelly, Phys. Rev. Lett. **101**, 26803 (2008).

[69] K. Chalapat, N. Chekurov, H. Jiang, J. Li, B. Parviz, and G. S. Paraoanu, Adv. Mater. **25**, 91 (2013).

[70] J. Zang, M. Huang, and F. Liu, Phys. Rev. Lett. **98**, 146102 (2007).

[71] J.-H. Cho, T. James, and D. H. Gracias, Adv. Mater. **22**, 2320 (2010).

[72] J.-H. Cho, D. Datta, S.-Y. Park, V. Shenoy, and D. Gracias, Nano Lett. (2010).

[73] L. Jijun and M. Dorel, Scripta Mater. **63**, 1120–1123 (2010).

[74] L. Zhou, Y. Wang, and G. Cao, Carbon **57**, 357 (2013).

[75] S. Shivaraman, et al., Nano Lett. **9**, 3100 (2009).

[76] M. Huang, et al., Adv. Mater. **17** (2005).

[77] A. J. Birnbaum and A. Pique, Appl. Phys. Lett. **98**, 134101 (2011).

[78] H. Skulason, P. Gaskell, and T. Szkopek, Nanotechnology **21**, 295709 (2010).

[79] D. S. L. Abergel, A. Russell, and V. I. Fal'ko, Appl. Phys. Lett. **91**, 063125 (2007).

[80] J. Park, Y. H. Ahn, and C. Ruiz-Vargas, Nano Lett. **9**, 1742 (2009).

[81] R. Sun, Y. Zhang, K. Li, C. Hui, K. He, X. Ma, and F. Liu, Appl. Phys. Lett. **103**, 013106 (2013).

[82] H. Song, S. Li, H. Miyazaki, S. Sato, K. Hayashi, A. Yamada, N. Yokoyama, and K. Tsukagoshi, Sci. Rep. **2**, 337 (2012).

[83] V. Barone, O. Hod, and G. Scuseria, Nano Lett. **6**, 2748 (2006).

[84] D. Kosynkin, A. Higginbotham, A. Sinitskii, J. Lomeda, A. Dimiev, B. Price, and J. Tour, Nature **458**, 872 (2009).

[85] L. Tapasztó, G. Dobrik, P. Lambin, and L. Biró, Nature Nanotechnol. **3**, 397 (2008).

[86] X. Liang, Y.-S. Jung, S. Wu, A. Ismach, D. Olynick, S. Cabrini, and J. Bokor, Nano Lett. **10**, 2454 (2010).

[87] M. Sprinkle, M. Ruan, Y. Hu, J. Hankinson, M. Rubio-Roy, B. Zhang, X. Wu, C. Berger, and W. de Heer, Nature Nanotechnol. **5**, 727 (2010).

[88] V. Ryzhii, V. Mitin, M. Ryzhii, N. Ryabova, and T. Otsuji, arXiv preprint arXiv:0804.1833 (2008).

[89] V. Ryzhii, M. Ryzhii, N. Ryabova, V. Mitin, and T. Otsuji, Jpn. J. Appl. Phys., Part 1 **48** (2009).

[90] Z. Duan, W. Liao, and G. Zhou, Advances in Condens. Matter Phys. **2010** (2010).